Stochastic Gravitational Wave Background from Eccentric Supermassive Black Hole Binaries in Dense Stellar Environments

Masterarbeit

zur Erlangung des akademischen Grades
Master of Science in Physik
am Institut für Theoretische Physik
der Goethe-Universität in Frankfurt am Main

vorgelegt von
Matthias Daniel

eingereicht am 06. März 2025

Erstgutachterin: Prof. Dr. Laura Sagunski
Zweitgutachter: Prof. Dr. Jürgen Schaffner-Bielich

Selbstständigkeitserklärung

Hiermit erkläre ich, dass ich die Arbeit selbstständig und ohne Benutzung anderer als der angegebenen Quellen und Hilfsmittel verfasst habe. Alle Stellen der Arbeit, die wörtlich oder sinngemäß aus Veröffentlichungen oder aus anderen fremden Texten entnommen wurden, sind von mir als solche kenntlich gemacht worden. Ferner erkläre ich, dass die Arbeit nicht - auch nicht auszugsweise - für eine andere Prüfung verwendet wurde.

Erlenbach am Main, den 06. März 2025

_____

Matthias Daniel

Abstract

In the summer of 2023, Pulsar Timing Array collaborations around the world, including NANOGrav, PPTA, EPTA, and CPTA, reported evidence for a correlated, stochastic signal in their data sets. This signal indicates the presence of a stochastic gravitational wave background (SGWB) in the nanohertz frequency range. The most likely source for this SGWB is a cosmic population of supermassive black holes in binary systems. These systems could reside in the centers of large galaxies and gradually lose orbital energy through the emission of gravitational waves until the black holes finally merge.

However, a noticeable turnover in the SGWB spectrum at the lowest observed frequencies suggests that these binary systems are not moving on circular orbits in a matter-free environment. Instead, they are influenced by interactions with their galactic surroundings and could also exhibit certain orbital eccentricities. The most effective mechanism driving their evolution is expected to be the gravitational interaction with surrounding stars via 3-body scatterings, through which stars are ejected from the inner regions of their host galaxies over time.

This thesis investigates in detail the impact of the initial orbital parameters of the binary systems and their stellar environment on the shape of the SGWB. Based on this, it is examined which combinations of the corresponding fit parameters best align the underlying theoretical model for the SGWB with the recent 15-year data from NANOGrav and 18-year data from PPTA. For this purpose, a Markov Chain Monte Carlo (MCMC) algorithm is employed.

For the first time, this study identifies a data-preferred value for the ratio of the stellar density to the velocity dispersion across most of the explored parameter space. In galactic centers hosting a supermassive black hole binary (SMBHB), this value is found to be around $10^2\,\mathrm{M}_\odot/\mathrm{pc}^3\,(\mathrm{km/s})^{-1}$ on a scale of approximately one parsec. Additionally, the MCMC results reveal a strict upper limit for this ratio, as the theoretical model would be inconsistent with the experimental data for values exceeding this threshold.

These findings provide valuable insights into the composition of matter in galactic cores and contribute to a better understanding of the dynamics of SMBHBs.

Zusammenfassung

Im Sommer 2023 berichteten Pulsar-Timing-Array-Kollaborationen auf der ganzen Welt, darunter NANOGrav, PPTA, EPTA und CPTA, über die Evidenz für ein korreliertes, stochastisches Signal in ihren Datensätzen. Dieses Signal weist auf die Existenz eines stochastischen Gravitationswellenhintergrunds (SGWB) im Nanohertz-Frequenzbereich hin. Die naheliegendste Quelle dafür ist eine kosmische Population supermassereicher Schwarzer Löcher in binären Systemen. Diese Systeme könnten sich in Zentren großer Galaxien befinden und verlieren allmählich durch die Abstrahlung von Gravitationswellen ihre Bahnenergie, solange bis die Schwarzen Löcher schließlich miteinander verschmelzen.
Eine auffällige Trendwende im SGWB-Spektrum bei den niedrigsten beobachteten Frequenzen deutet jedoch darauf hin, dass diese binären Systeme sich nicht auf kreisförmigen Bahnen im materiefreien Raum bewegen. Stattdessen werden sie durch Interaktionen mit ihrer galaktischen Umgebung beeinflusst und könnten außerdem gewisse Bahnexzentrizitäten aufweisen. Dabei ist der effektivste Mechanismus, der ihre Evolution vorantreibt, vermutlich die gravitative Wechselwirkung mit umliegenden Sternen über Drei-Körper-Streuungen, durch die Sterne aus den inneren Bereichen ihrer Wirtsgalaxien mit der Zeit herausgeschleudert werden.
Diese Arbeit untersucht detailliert den Einfluss derjenigen Bahnparameter, die die binären Systeme zum Zeitpunkt ihrer Entstehung inne haben, sowie ihrer stellaren Umgebung auf die Form des SGWB. Darauf basierend wird geprüft, welche Kombinationen der entsprechenden Fit-Parameter das zugrunde liegende theoretische Modell zum SGWB am besten mit den aktuellen 15-Jahres-Daten von NANOGrav und 18-Jahres-Daten von PPTA in Einklang bringen. Zu diesem Zweck kommt ein Markov Chain Monte Carlo (MCMC)-Algorithmus zum Einsatz. Dieser Studie gelingt es erstmals, einen von den Daten bevorzugten Wert für das Verhältnis der stellaren Dichte zur Geschwindigkeitsdispersion über weite Teile des erkundeten Parameterraums zu identifizieren. Dieser Wert beträgt in galaktischen Zentren mit einem supermassereichen binären System auf einer Skala von etwa einem Parsec ungefähr $10^2\,\mathrm{M}_\odot/\mathrm{pc}^3\,(\mathrm{km/s})^{-1}$. Darüber hinaus offenbaren die MCMC-Ergebnisse eine strikte Obergrenze für dieses Verhältnis, da das theoretische Modell für Werte darüber inkonsistent mit den experimentellen Daten wäre. Diese Erkenntnisse liefern wertvolle Einblicke in die Zusammensetzung der Materie in galaktischen Kernen und tragen zu einem besseren Verständnis der Dynamik supermassereicher Schwarzer Löcher in binären Systemen bei.

Publications Relevant to this Thesis

This thesis is based on the procedure and findings of the first study [1] listed below. In the second publication [2], the research from my Bachelor thesis [3] is extended to the Laser Interferometer Space Antenna (LISA). For both papers, the main contents and key results are provided, along with a description of their relevance to this Master thesis.

[1] Y. Chen, M. Daniel, L. Sagunski, X. Xue, and *The NANOGrav Collaboration*, "Galaxy Tomography with the Gravitational Wave Background from Supermassive Black Hole Binaries," Nov. 2024. arXiv: 2411.05906, *submission to Nature Astronomy pending.*

By analyzing the 15-year data from NANOGrav, we investigate how the SGWB from a cosmic population of SMBHBs is influenced by the initial inner galactic density profile prior to its disruption by the ejection of stars (or cold dark matter clumps) via the gravitational slingshot mechanism, considering a wide range of initial binary eccentricities. Our findings reveal a parsec-scale galactic center matter density of approximately $10^6\,M_\odot/pc^3$ across most of the examined parameter space. This sheds light on the environmental impact on the evolution of SMBHBs and the combined (baryonic and dark) matter density in galactic nuclei.
This work was published in collaboration with NANOGrav. The authors' contributions can be found in detail at the end of the paper.

This Master thesis also serves as a cross-check for the results of this publication, since slightly different but consistent approaches within the theoretical model for calculating the SGWB are employed as well as different codes[1] for the data analysis through a MCMC algorithm. Specifically, both different fit parameters describing the galactic density profile and an alternative population model (supplied by NANOGrav) are utilized (for detailed discussions, see Subsecs. 2.2 and 2.6). Furthermore, it is important to mention that this thesis uses not only the NANOGrav data but also the current data from PPTA. Despite these variations, both studies come to the same overall results.

[1] While the `SMBHBpy` code is applied in this work (see Subsec. 3.1), our publication uses `holodeck` from NANOGrav and `PTArcade` [4].

[2] M. Daniel, K. Pardo, and L. Sagunski, "Forecasted Detection Limits on the (Dark) Matter Density in Supermassive Black Hole Binaries for LISA," Jan. 2025. arXiv: 2501.13601, *submitted to Physical Review D.*

We first study the evolution of individual SMBHBs driven by Chandrasekhar's dynamical friction with dark matter (DM) spikes surrounding their components. We confirm that both eccentric orbits and the presence of (dark) matter in such systems significantly accelerate their orbital evolution compared to the case where the supermassive black holes (SMBHs) move on circular orbits through vacuum. Next, we develop a model-independent approach to forecast upper limits on the (dark) matter density for given future SMBHB observations with LISA. For this purpose, we limit our analysis to circular, equal-mass[2] SMBHBs, but take into account different redshifts and black hole masses. We then compare these thresholds with the theoretical density profiles expected for spikes consisting of self-interacting DM particles. We conclude that LISA will be able to detect GW signals of SMBHBs with densities over several orders of magnitude, including those of self-interacting DM spikes.

The paper was written by me. K. Pardo and L. Sagunski contributed significantly to the continuous improvement of the draft by providing extensive feedback. The figures were generated using a version[3] of the `SMBHBpy` code, which was developed by me but differs from the one used in this work.

In this thesis, it is assumed that SMBHBs do not interact gravitationally with their stellar or DM environment through the dynamical friction mechanism but rather through 3-body scatterings (see Subsecs. 2.1 and 2.2). By comparing the two studies, one finds that both effects could have similar impacts on the evolution of binary systems.

[2]The term "equal-mass" means that the two SMBHs of a binary system have the same mass.

[3]This version is an extension of the `IMRIpy` code [5], written by Niklas Becker, and publicly available on GitHub (https://github.com/DMGW-Goethe/SMBHBpy).

List of Abbreviations

3B – (gravitational slingshot ejections via) 3-body (interactions)

AT – arrival time (of the periodic pulsar signal)

CL – confidence level

CPTA – Chinese Pulsar Timing Array

DM – dark matter

EFE – Einstein field equations

EPTA – European Pulsar Timing Array

ET – Einstein Telescope

GR – General Relativity

GW – gravitational wave

HD – Hellings-Downs (correlation)

ISCO – innermost stable circular orbit (around a black hole)

KAGRA – Kamioka Gravitational Wave Detector

LIGO – Laser Interferometer Gravitational-Wave Observatory

LISA – Laser Interferometer Space Antenna

MCMC – Markov Chain Monte Carlo (sampling)

NANOGrav – North American Nanohertz Observatory for Gravitational Waves

PPTA – Parkes Pulsar Timing Array

PTA – Pulsar Timing Array

SGWB – stochastic gravitational wave background

SMBH – supermassive black hole

SMBHB – supermassive black hole binary

Contents

1 Introduction

1.1 Stochastic Gravitational Wave Background

Gravitational waves (GWs) have become a crucial source of information for today's astrophysicists, offering a direct window into the universe and enabling the exploration of its many mysteries. Their detection through current Earth-based interferometric detectors, such as Advanced LIGO[4], Advanced Virgo[5], and KAGRA[6], has opened up new avenues of research. As detectors operating in the GW frequency range of approximately 10 Hz to 10^4 Hz [10], they are primarily sensitive to mergers of neutron stars and stellar-mass[7] black holes in compact binary systems. However, this frequency range also allows for the investigation of other *astrophysical* phenomena, such as asymmetrically rotating neutron stars or powerful bursts like core-collapse supernovae. Future detectors with enhanced sensitivity, such as the Einstein Telescope[8], could have the potential to detect these specific GW sources. All of these objects produce individually *resolvable* GW signals, generally characterized by *deterministic* properties [12].

In contrast, a *random* superposition of a large number of independent and individually *unresolved* signals from all the aforementioned astrophysical sources leads to a continuous "background noise" in the universe. This so-called stochastic gravitational wave background (SGWB) remains hidden beneath the intrinsic noise level of current single GW detectors. While certain data from LIGO and Virgo implies that a stochastic background generated by merging binary systems may exist in the frequency range to which both detectors are sensitive [13], the Pulsar Timing Array (PTA) collaboration NANOGrav (see Subsec. 1.2) recently found compelling evidence for the existence of a SGWB in the nanohertz frequency regime in their data [14]. The dominant sources of the SGWB in this low-frequency range are expected to be unresolved supermassive black hole binaries (SMBHBs) (see Subsec. 2.1) due to their powerful GW signals [15], [16].

[4]The Advanced Laser Interferometer Gravitational-Wave Observatory (Advanced LIGO) is a system of two second-generation GW detectors located in the USA [6]. On September 14, 2015, the two detectors made the first-ever detection of GWs from the merger of two stellar-mass black holes (GW150914) [7].

[5]Advanced Virgo is another GW detector located in Italy, and it is also part of the network of significantly more sensitive second-generation detectors [8].

[6]The Kamioka Gravitational Wave Detector (KAGRA) is also one of the new-generation GW observatories, located in Japan. What makes KAGRA unique is that it is the first underground GW detector [9].

[7]The term "stellar-mass" refers to black hole masses up to $\sim 100\,\mathrm{M}_\odot$.

[8]The Einstein Telescope (ET) is a proposed third-generation, ground-based GW observatory. One of the many promising features of ET is its ability to detect mergers of black hole binaries up to a redshift of $z \sim 20$ [11].

In addition, GWs from *cosmological* processes in the early universe are also predicted to contribute to the stochastic background over a wide frequency range [17]. Examples of such sources include primordial quantum fluctuations amplified by the inflation [18], cosmic strings [19], cosmological first-order phase transitions [20] and scalar-induced GWs [21]. All these models are capable of explaining the recent data provided by different PTA collaborations. This illustrates that, at present, none of the mentioned theories for generating a SGWB can be definitively ruled out. Nevertheless, future data sets will improve the ability to differentiate cosmological origins from astrophysical sources like SMBHBs. Observing *anisotropies* in the SGWB, which are expected on smaller scales, could resolve this problem, since those generated by SMBHBs are significantly larger than those produced by most cosmological sources [22].

However, in general, it is assumed that the stochastic background is *isotropic*, meaning it has the same fundamental statistical properties regardless of the region of the sky where it is observed [23]. Similar to the cosmic microwave background [24], [25], studying anisotropies in the SGWB could enhance our understanding of their cosmological [26] and astrophysical [27] origins, and thereby, of the universe itself. For example, if one assumes that the SGWB is produced by inspiraling SMBHBs, exploring the deviations from isotropy can provide information about the discrete distribution of these binary systems in the local universe and the statistical characteristics of their population [28]–[31].

It should also be mentioned that for a deeper understanding of the evolution of SMBHBs and the influence of their matter environment, detecting isolated signals from individual binary systems is crucial. Extracting imprints of individual SMBHBs from the top of the nanohertz SGWB is a challenge, but it is not impossible, as demonstrated by Ref. [32]. On the other hand, detecting GW signals emitted by binary systems with masses between approximately $10^3\,\mathrm{M}_\odot$ and $10^7\,\mathrm{M}_\odot$ during the last years to hours before coalescence, is expected to be more straightforward with the space-based interferometric GW detector LISA[9] in future [33]. This is because the number of such massive binary systems merging around the same time should be relatively low within the frequency range accessible to LISA, making a significant overlap of the corresponding signals, as observed in the low-frequency range, less likely.

This work focuses on the astrophysical SGWB in the nanohertz frequency regime generated by

[9]The Laser Interferometer Space Antenna (LISA) is a planned space-based GW observatory adopted by the European Space Agency. LISA will operate in the frequency range from $10^{-5}\,\mathrm{Hz}$ to $10^{0}\,\mathrm{Hz}$, thus bridging the gap between the Pulsar Timing Arrays in the nanohertz regime and current ground-based detectors in the range of $10\,\mathrm{Hz}$ to $10^{4}\,\mathrm{Hz}$ [33].

a cosmic population of SMBHBs. As several previous studies have shown, the precise shape of the characteristic strain of this stochastic background strongly depends on the eccentricity of the orbits of the supermassive black holes (SMBHs) [34] and how they interact with their matter environment [16], [35]–[37], while the amplitude of the SGWB is deeply connected with the galaxy merger rate or SMBHB formation rate. In this context, both dynamical friction [38], [39] with dark matter (DM) spikes[10] [41], [42] and slingshot ejections of stars via 3-body interactions (see Subsec. 2.2) [43]–[47] have been considered as potential effects that lead to the loss of orbital energy and orbital angular momentum of the SMBHBs (see Subsec. 2.1). Additionally, the signatures in the SGWB resulting from accretion disks of gaseous matter have also been explored [48], [49].

The further investigation of the specific impacts on the SGWB caused by eccentric orbits and ejections of stars from galactic centers through gravitational slingshots around SMBHBs is the aim of this thesis and will be discussed in more detail in Subsec. 4.1.

1.2 Pulsar Timing Arrays and Hellings-Downs Correlation

Pulsar Timing Arrays are sets consisting of millisecond pulsars[11] – rapidly rotating and highly magnetized neutron stars – distributed across our galaxy. These pulsars serve as stable and accurate cosmic clocks, emitting periodic electromagnetic signals[12] that can be detected and analyzed from Earth. The continuous monitoring of these objects enables the measurement of their astrometric parameters as well as deviations in the arrival times (ATs) of their pulses.

Various effects lead to *correlated* signatures among the pulsars in the ATs, which can be distinguished based on their *multipole* contributions to the timing residuals. For instance, uniform influences that are direction-independent and affect all pulsar signals simultaneously can be formulated as a *monopole* term. Conversely, for example, errors in the transformation between different reference frames, which depend on the position of the pulsars in the sky, manifest as a *dipole* contribution [52].

The primary application of PTAs is to use them as galactic-scale detectors for GWs in the

[10] A dark matter spike is an overdense region around a SMBH, which forms as the black hole undergoes adiabatic growth within a dark matter halo [40].

[11] Millisecond pulsars are used because their rotational stability is generally 3-4 orders of magnitude better than that of normal pulsars [50], and their timing stability over several years is comparable to the most precise atomic clocks on Earth [51]. These are just two factors that significantly reduce the probability for pulsar-induced deviations in the ATs of their signals.

[12] Such a periodic signal arises due to a misalignment between the pulsar's rotation and magnetic axes.

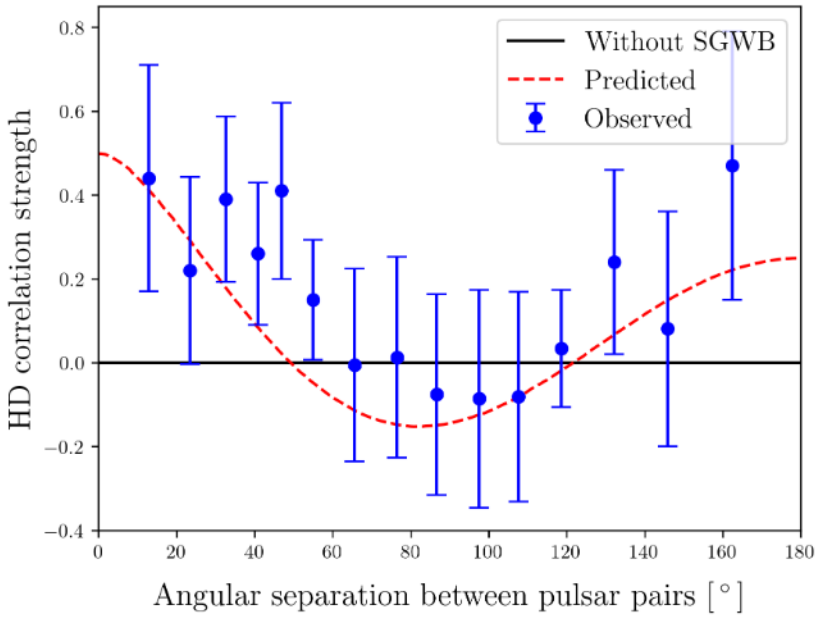

Fig. 1.1: Angular-separation-binned interpulsar correlations measured from all 2,211 possible pairings between the 67 pulsars of the NANOGrav 15-year PTA (blue data points). The red dashed line shows the predicted HD correlation for an isotropic SGWB. Additionally, the black line represents the case in which no stochastic background exists that would disturb the ATs of the pulsar signals, thus resulting in no HD-correlated signatures between them. This figure is reproduced from Fig. 1 (c) of Ref. [14].

nanohertz frequency range. As it was first described by Refs. [53] and [54], for this purpose, a pulsar and the Earth (or more precisely the solar system barycenter) can be treated as free masses acting together as a GW antenna. Long-wavelength GWs passing between the Earth and a distant pulsar induce slight perturbations in the ATs and would leave characteristic correlations of *quadrupole order or higher* in the data.

PTA collaborations worldwide, such as the North American Nanohertz Observatory for Gravitational Waves (NANOGrav) [14], the Parkes Pulsar Timing Array (PPTA) [55], the European Pulsar Timing Array (EPTA) [56], and the Chinese Pulsar Timing Array (CPTA) [57], are searching for a specific quadrupole (and higher order) correlation in the timing residuals of pulsar signals that only depends on their angular separation on the sky as seen from Earth. This so-called *Hellings-Downs correlation* [58] is a prediction of General Relativity (GR) for an *isotropic* SGWB in the universe and cannot be mimicked by other sources[13] [60].

In the summer of 2023, NANOGrav announced the identification of a correlation following the Hellings-Downs (HD) pattern in their 15-year pulsar timing data set, which includes 67 pulsars

[13] A detailed theoretical derivation of the Hellings-Downs correlation can be found, for example, in Ref. [59].

[14]. The corresponding results are shown in Fig. 1.1. The other PTA collaborations mentioned above found similar manifestations of this signature in their data [55]–[57]. This provides the first strong evidence for the existence of a SGWB in the nanohertz regime.

1.3 Motivation

By studying the SGWB of SMBHBs it is possible to gain significant insights into the environmental composition and astrodynamical properties of these binary systems. The latest data from the major PTA collaborations not only provide strong evidence for an isotropic SGWB in the nanohertz frequency regime, as mentioned in the previous subsections, but also indicate that SMBHBs are not simply moving on circular orbits through vacuum. Instead, it is inferred that they evolve within dense matter environments and could exhibit a certain eccentricity distribution. These conclusions are based on an observed turnover[14] in the arrangement of the data points for the SGWB at the lowest accessible frequencies, particularly around 3 to 4 nHz, as can be seen from Fig. 1.2.

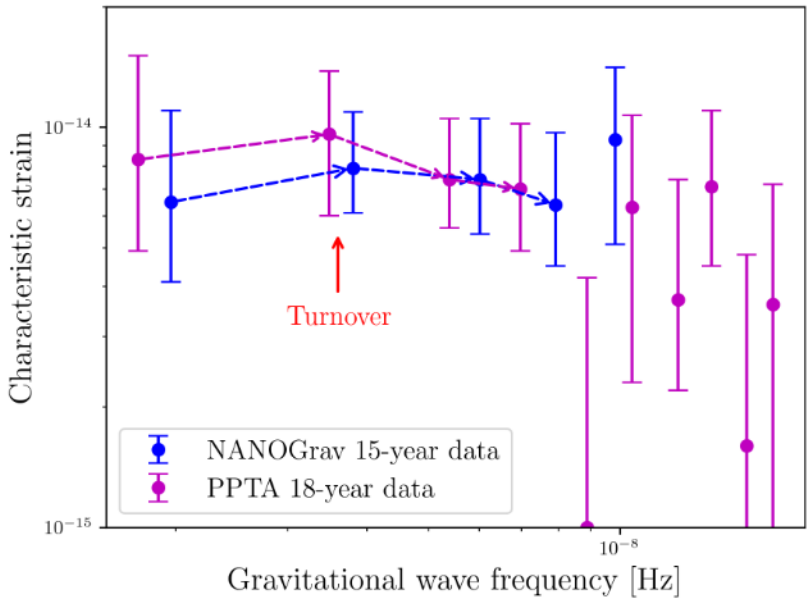

Fig. 1.2: Frequency-binned SGWB derived from the NANOGrav 15-year data set (lowest five bins, blue) and the PPTA 18-year data set (lowest ten bins, violet), respectively. The data, including uncertainties, were extracted from Fig. 5 of Ref. [41] after being verified for accuracy. Additionally, the approximate position of the turnover is marked by a red arrow. The dashed arrows visualize the change in the slope.

[14] It is explicitly not possible to explain this turnover by assuming circular SMBHBs surrounded by vacuum. A detailed discussion on this will be provided in Chap. 4.

Using various theoretical models describing the interaction of binary systems with their matter environment and the resulting eccentricity evolution, several previous studies have already attempted to explain different PTA data.

For example, Ref. [35] considered the SGWB generated by *eccentric* SMBHBs, while Refs. [36] and [16] examined the stochastic background produced by *circular* SMBHBs. All three publications used the 15-year data set from NANOGrav and employed a *phenomenological* approach to account for the interaction between the SMBHBs and general forms of matter, such as stars, gas, or dark matter. In contrast, Refs. [41] and [42] focused on *circular* supermassive binary systems that lose energy through the effect of *dynamical friction with dark matter spikes*. Both used the latest data sets from NANOGrav and PPTA, while Ref. [41] additionally utilized current data from EPTA.

The studies most closely related to the aims of this thesis are Refs. [44], [61], [47] and [56]. All of them examined *gravitational slingshot ejections of stars* from galactic nuclei in their analyses and were able to constrain the associated parameter space with respect to the *eccentricity* at different stages of the evolution of SMBHBs and quantities related to the matter density in these systems, albeit to a limited extent. For this purpose, they use data that precisely emulates the sensitivity of the 9-year NANOGrav data set, simulated PTA data in conjunction with certain constraints on the SGWB's amplitude from PPTA, the 15-year NANOGrav data set and the recent EPTA data set, respectively[15].

Their results and the findings of some of the other previously mentioned papers show that it is extremely challenging to distinguish the effects on the SGWB caused by eccentricity and the dark or baryonic matter environment by using PTA data. This is because highly eccentric SMBHBs evolving in environments with lower density generate a SGWB with a similar shape to that produced by a lower eccentricity binary population in a denser environment. Nevertheless, setting a stringent upper limit on the matter densities in SMBHBs would be a first step toward breaking this degeneracy and could help to improve our understanding of the properties of the matter in galactic centers as well as to constrain the contribution of dark matter in these regions. The former is among the objectives of this thesis.

Building on this previous research, this work employs a Markov Chain Monte Carlo (MCMC) sampling algorithm to further investigate the aforementioned degeneracy between the eccen-

[15]It should be noted that these works had access to different PTA data due to the varying years of their publication. However, all studies utilized results such as stringent upper limits on the SGWB's amplitude that reflected the most up-to-date research from various PTA collaborations at the time.

tricity of SMBHBs and the gravitational slingshot mechanism as environmental effect. This degeneracy will be partially disentangled by constraining the parameter space consisting of the initial eccentricity e_0, as the eccentricity at SMBHB formation, the ratio of the stellar density ρ to the velocity dispersion σ, and the quantity A_0 which is related to the level of the stochastic background. For this purpose, the recent 15-year data from NANOGrav and 18-year data from PPTA are used.

After the motivation and aims of this study have been outlined, the following subsections provide the theoretical background on the formation and evolution of SMBHBs (see Subsec. 2.1), with a focus on the gravitational slingshot effect (see Subsec. 2.2) and the emission of GWs (see Subsec. 2.3). Additionally, the connection between the GW signals from individual SMBHBs (see Subsec. 2.5) and the astrophysical SGWB produced by a cosmic population of such binary systems (see Subsec. 2.6) is established. Next, the numerical setup is introduced, explaining how the theory on calculating the stochastic background is translated into the `SMBHBpy` code (see Subsec. 3.1), along with a detailed overview of the MCMC algorithm used (see Subsec. 3.2). The results of this work are presented and discussed in Chap. 4, while Chap. 5 finally draws conclusions based on these findings.

2 Theoretical Background

2.1 Formation and Evolution of SMBHBs in Galactic Centers

When two galaxies, each harboring a SMBH with a mass ranging from $10^5\,\mathrm{M}_\odot$ to $10^{10}\,\mathrm{M}_\odot$ at their galactic center, collide, they could merge into a larger galaxy [62]. In this newly formed galaxy, the two SMBHs initially do not really feel each other's gravitational potential and thus evolve independently of each other. However, for a gravitationally bound system to form, the distance between the two SMBHs must first be reduced. This task is handled by dynamical friction [38] with stars or gas surrounding the SMBHs [63]. This mechanism is assumed to be important for reducing the initial separation between the SMBHs of $\mathcal{O}(10\,\mathrm{kpc})$ down to a few (tens of) parsecs.

At the separation where the mass of the matter enclosed between them is twice as large as the mass of the SMBH-pair, the gravitational attraction is sufficient to form a binary system[16] and dynamical friction ceases to be efficient. This separation corresponds by definition to the radius r_infl of the sphere of influence of the SMBHB [67]. This suggests equating the initial semi-major axis a_0 of a SMBHB with its corresponding r_infl as long as matter is present in the binary system. In the case of a vacuum, however, a_0 cannot be interpreted as the influence radius. Typically, it is assumed that the components of these binary systems can be described as point-like masses m_1 and m_2, moving around their common center of mass on Keplerian orbits[17] with a semi-major axis a and eccentricity e. The description of a SMBHB within this Newtonian approximation is valid as long as the separation between both constituents is greater than the sum of their innermost stable circular orbits (ISCOs), i.e., for $a > r_\mathrm{ISCOs} = r_\mathrm{ISCO,1} + r_\mathrm{ISCO,2}$ with

$$r_\mathrm{ISCOs} = 6\,\frac{Gm_1}{c^2} + 6\,\frac{Gm_2}{c^2} = 6\,\frac{Gm_1(1+q)}{c^2}\,, \tag{2.1}$$

where $q = m_2/m_1 \leq 1$ is the mass ratio of the two Schwarzschild-SMBHs, c the speed of light in vacuum and G Newton's gravitational constant. Furthermore, a binary system is referred to

[16] To date, there are no unequivocally confirmed observations of gravitationally bound SMBHs. Nevertheless, there are several systems, such as the blazar OJ 287 [64] and the two elliptical radio galaxies 0402+379 [65] and 3C 66B [66], which host a highly promising candidate for a SMBHB.

[17] This implies that a SMBHB is modeled as a classical two-body system. Effects of GR are neglected in describing the orbits, which is justified by the large separations between the SMBHs compared to their ISCOs in the PTA frequency band.

as "hard" once the semi-major axis reaches the value[18] $a_h = \frac{q}{4(1+q)^2}\, r_{\mathrm{infl}}$ [68].

This work assumes that the gravitational slingshot ejection of stars through 3-body interactions [69] is the dominant effect responsible for the energy and angular momentum loss of a SMBHB from its formation at a_0 up to a certain value for the semi-major axis, beyond which GW emission dominates the final, sub-parsec phase until coalescence (see Subsec. 2.4).

However, if the supply of stars diminishes and, consequently, the gravitational slingshot effect becomes too inefficient to further drive the hardening[19] of the binary system, the evolution of SMBHBs would stagnate at $\mathcal{O}(1\,\mathrm{pc})$, since the loss of energy through the emission of GWs would not be sufficient to bring their components to merge within the Hubble time $t_H = 13.79\,\mathrm{Gyr}$ [70]. Nevertheless, observations [71], [72] suggest that mergers of SMBHs have indeed occurred throughout the history of the universe. This contradiction is known as the final parsec problem [73]. However, N-body simulations [74], [75] have shown that a certain triaxiality[20] in the geometry of the host galaxy of the SMBHB can cause a repopulation of the loss cone[21] [77], [78]. The stars interacting with the binary system are therefore not depleted and the gravitational slingshot effect remains efficient.

Fig. 2.1 provides an overview of the mechanisms discussed in this subsection that dominate the evolution of a SMBHB at different stages, using the example of a specific circular SMBHB typically expected to contribute to the SGWB in the nanohertz frequency range (for a detailed discussion, see Subsec. 2.6). It can be observed that the influence of the stellar environment on the evolution and the GW signal of this SMBHB may still play an important role at the low-frequency end of the PTA band (area delimited by red arrows). This further supports the idea of using current PTA data to investigate the matter composition of supermassive binary systems. However, it is important to mention that the transition region between GW emission (green area) and the gravitational slingshot mechanism (orange area) is shifted to larger binary separations for eccentric orbits as well as for lower matter densities, gradually moving out of the PTA band (see Subsec. 2.4). Therefore, the interplay between eccentricity and the stellar environment will play a crucial role in understanding the recent NANOGrav and PPTA data

[18] It should be noted that there is no uniform definition for a "hard" binary system in the literature. In this study, the definition introduced here is used.

[19] The term "hardening" means the reduction of the separation between the two components of a SMBHB.

[20] The newly formed galaxy has substantial deviations from sphericity induced by the merger of the initial galaxies.

[21] The loss cone refers to a specific phase space region. Stars within this region are highly likely to be ejected from the galactic center due to the gravitational slingshot effect. The term originally comes from plasma physics [76].

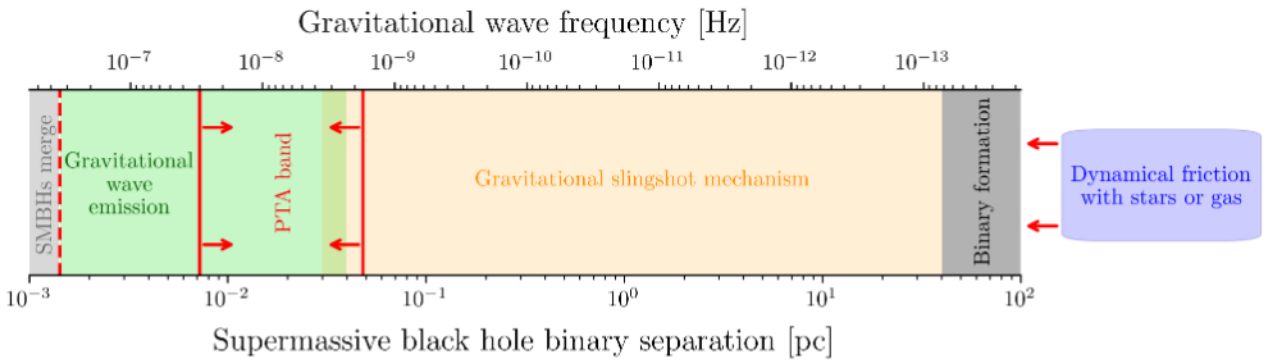

Fig. 2.1: Mechanisms (gravitational slingshot effect: orange area, and GW emission: green area) driving the evolution of a circular SMBHB with $m_1 = 3 \times 10^9\,\mathrm{M}_\odot, q = 0.65$ and $z = 0.3$ in a dense stellar environment after the binary has formed (dark gray region) through dynamical friction with stars or gas (blue box). The corresponding separation between the two SMBHs as well as the observed frequency of the GW signal emitted during the different phases are shown on the two horizontal axes. Furthermore, within the entire frequency range from formation to merger (light gray region), the approximate bandwidth of current PTAs is marked by red arrows. This plot was created by me.
Note: The exact value for the binary separation below which the evolution of the SMBHB is dominated by GW emission depends on parameters such as ρ and σ, which characterize the stellar environment and thus the strength of the gravitational slingshot effect (for more details, see Subsec. 2.4).

using the theoretical model for calculating the SGWB introduced in the next subsections.

In addition, this work assumes that the effect of dynamical friction is not relevant for the sub-parsec evolution of SMBHBs and thus has no notable influence on their corresponding GW signal. This form of interaction can, for example, arise from accretion disks consisting of gaseous or stellar matter [79], [80] or from dark matter spikes surrounding the SMBHs. However, as shown in Refs. [81] and [41], the energy deposited in such spikes through dynamical friction can exceed their potential binding energy, causing the spikes to become saturated and eventually dissipate over time[22]. Moreover, these structures can be destroyed during the collision of the galaxies initially hosting the individual SMBHs [83], [84].

[22]It should also be noted that self-interacting dark matter particles [82] might be capable of rethermalizing and replenishing the spikes sufficiently fast, allowing these structures to survive for a longer period. Nevertheless, this process significantly weakens their impact on the evolution of SMBHBs via the dynamical friction mechanism [41].

2.2 Slingshot Ejections via 3-Body Interactions

The gravitational interaction of a SMBHB with unbound stars of an isotropic, fixed background within its host galaxy can be described as the sum of individual 3-body scatterings[23]. Through this type of interaction, stars with masses $m_\star \ll m_1, m_2$ are ejected from the galactic center at increased velocities, similar to a slingshot, which extracts energy and angular momentum from the binary system, leading to a gradual approach of its components over time. This mechanism will be referred to as "3B" throughout this work. The influence of this gravitational slingshot effect on the evolution of binary systems and the distribution of stellar matter in their host galaxies is determined by three dimensionless parameters [69]: the hardening rate

$$H = \frac{\sigma}{G\rho} \frac{d}{dt_r} \left(\frac{1}{a} \right) \Bigg|_{\text{3B}} , \tag{2.2}$$

where ρ is the density of the stellar background, σ the one-dimensional velocity dispersion and t_r the time in the rest frame of the SMBHB, the eccentricity growth rate

$$K = \frac{de}{d\ln(1/a)} \Bigg|_{\text{3B}} , \tag{2.3}$$

and the mass ejection rate

$$J = \frac{1}{M} \frac{dM_{\text{ej}}}{d\ln(1/a)} \Bigg|_{\text{3B}} , \tag{2.4}$$

with M_{ej} as the stellar mass ejected from the galactic core and $M = m_1 + m_2 = m_1(1+q)$ as the total mass of the binary system.

In general, H, K, and J, as partially evident from their definitions, depend on different SMBHB parameters, such as the mass ratio q, the eccentricity e, and the degree of hardness[24] [69], [86]. Moreover, the cross section of individual 3-body scatterings also plays an important role in determining these three quantities. The cross section, in turn, depends on the incoming/outgoing direction and the initial/final velocity of a background star before/after the scattering [85], [87]. Despite these complex correlations, the hardening rate H can be well constrained to between

[23] This mechanism applies for both stars and, for example, clumps of cold, collisionless dark matter. The latter is not always explicitly mentioned in this work.

[24] The degree of hardness can be specified, for example, by comparing the current relative velocity between the SMBHs with the velocity dispersion of the background stars [69], or by comparing the current semi-major axis with the value at which a binary system is considered as "hard" [85].

approximately 15 and 20 for hard binary systems through numerical scattering experiments [69], [85]. For the SMBHBs considered later in this work, $H = 18$ is an appropriate value.
The situation is different for the eccentricity growth rate K. A parameterization for K comparable with the results obtained in Refs. [69] and [85] was introduced by Ref. [88]. It reads

$$K \approx 0.3\, e\, (1 - e^2)^{0.6} \left(1 + \frac{a}{\tilde{a}_0}\right)^{-1} \geq 0\,, \tag{2.5}$$

where $\tilde{a}_0$ is defined as $\tilde{a}_0 = 0.2\, a_h$ with $a_h = \frac{q}{4(1+q)^2}\, r_{\text{infl}}$. This specific parameterization is also adopted in this work. Examining the above equation for K more closely, it becomes evident that the gravitational slingshot mechanism always leads to an eccentrification of the SMBHs' orbits[25] (see also Fig. 4.1). At the same time, $K(e \to 1) \to 0$ ensures that the eccentricity does not exceed the physically allowed range of $0 \leq e < 1$. Additionally, K increases with increasing mass ratio q for a given r_{infl}.
Fig. 2.2 shows the values that K takes across a wide range of a and e using the example of a specific SMBHB. From the same figure and Eq. 2.5, it is evident that K approaches 0 for small eccentricities e (and those close to 1) as well as for large semi-major axes a. In contrast, the eccentricity growth rate reaches its maximum of $K_{\text{max}} \approx 0.141$ at e ≈ 0.674 for $a \to 0$.
Since K, as given in Eq. 2.5, also depends on the influence radius r_{infl}, it should be recalled at this point that r_{infl} is defined as the separation between the SMBHs where the mass M_{matter} of the matter enclosed between them is twice the binary mass M, i.e.,

$$2M = M_{\text{matter}}(r < r_{\text{infl}}) = 4\pi \int_0^{r_{\text{infl}}} \rho(r)\, r^2\, dr\,. \tag{2.6}$$

In this work, it is assumed that the exact form of the stellar density profile $\rho(r)$, and thus the expression for calculating r_{infl} and $\rho(r = r_{\text{infl}})$, are unknown, as it is typically the case. Instead, r_{infl} is identified with the initial semi-major axis a_0 and treated as a free binary parameter[26].
In general, in Eq. 2.2, not only ρ but also σ depends on the binary separation[27] r. However,

[25] As will be demonstrated in Subsec. 2.3, the emission of GWs has the opposite effect.

[26] In paper [1], we consider a power-law ansatz for $\rho(r)$. Instead of fixing the value of r_{infl}, we treat the slope and normalization constant of this density profile as free/model parameters and use them to calculate $r_{\text{infl}} = a_0$. However, these two approaches are equivalent.

[27] The velocity dispersion σ in the central region of a galaxy (usually within the galactic bulge) can be determined experimentally directly through observations [89], from which empirical correlations between the mass of the central SMBH and σ can be derived [90]. Typical values are between approximately 80 km/s and 440 km/s for masses between $5 \times 10^6\, \text{M}_\odot$ and $5 \times 10^9\, \text{M}_\odot$.

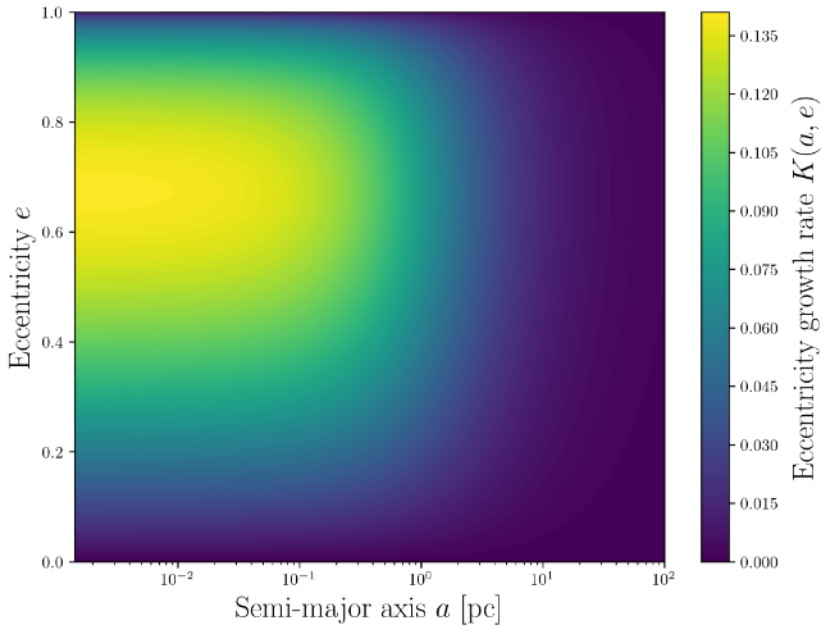

Fig. 2.2: Dimensionless eccentricity growth rate K for different semi-major axes a in parsecs and eccentricities e. To obtain these results, $q = 0.65$ and $r_{\text{infl}} = 100\,\text{pc}$ are used. The smallest value of a considered corresponds to r_{ISCOs} (see Eq. 2.1) for which $m_1 = 3 \times 10^9\,\text{M}_\odot$ is chosen.

by comparing the predictions for the hardening rate and for the eccentricity evolution of a SMBHB from N-body simulations with the results from 3-body scatterings, Ref. [91] found that the outcomes of both numerical techniques are in reasonable agreement if ρ and σ in Eq. 2.2 are the stellar matter density and the velocity dispersion at the influence radius r_{infl} of the SMBHB. This finding is equivalent to saying that an efficient loss cone refilling occurs at r_{infl} [92]. For this reason, from this point onward, ρ and σ will always refer specifically to the stellar density and velocity dispersion at r_{infl}, rather than their full spatial distributions.

Since the supply of stars in the region of the loss cone, which is crucial for the hardening of a SMBHB, does not diminish (see Subsec. 2.1), a detailed study of the matter ejection rate J is not necessarily relevant for describing the orbital evolution of a SMBHB. However, it should be kept in mind that the total stellar mass that can be expelled from the region within the sphere of influence should be limited to a few multiples of the mass of the binary system, according to the definition of r_{infl} in Eq. 2.6. This has also been verified by Refs. [69], [93] and [94]. Therefore, the impact of the mechanism discussed in this subsection on the temporal evolution of the orbital parameters a and e of a SMBHB can be fully described by H and K.

Based on this, in the following, an expression for the energy and angular momentum loss of a

binary system due to the gravitational slingshot effect will be derived.
Within the Newtonian approximation the SMBHs move on eccentric Keplerian orbits, and thus, at any given time, the binary system has a certain orbital or binding energy E_{orb}, given by

$$E_{\mathrm{orb}} = -\frac{GM\mu}{2a} \,, \tag{2.7}$$

and an angular momentum $\vec{L}_{\mathrm{orb}}$ with magnitude

$$L_{\mathrm{orb}} = \mu\sqrt{GMa(1-e^2)} = \mu GM\sqrt{\frac{\mu(e^2-1)}{2E_{\mathrm{orb}}}} \,. \tag{2.8}$$

Here, the reduced mass $\mu = m_1 m_2/M$ of the binary system was introduced with $M = m_1 + m_2 = m_1(1+q)$ as its total mass. As mentioned before, the mass ratio q of the SMBHs is defined as $q = m_2/m_1 \leq 1$. First, Eq. 2.2 can be rewritten as

$$\left.\frac{da}{dt_r}\right|_{\mathrm{3B}} = -HG\,\frac{\rho}{\sigma}\,a^2 \,. \tag{2.9}$$

Thus, the energy loss of a SMBHB due to the ejection of stars from the galactic center is given by

$$\frac{dE_{\mathrm{3B}}}{dt_r} = \left.\frac{dE_{\mathrm{orb}}}{dt_r}\right|_{\mathrm{3B}} = \left.\frac{\partial E_{\mathrm{orb}}}{\partial a}\,\frac{da}{dt_r}\right|_{\mathrm{3B}} = -\frac{HG^2M\mu}{2}\,\frac{\rho}{\sigma} \,. \tag{2.10}$$

As previously discussed, H, ρ, and σ can be considered as fixed quantities. Therefore, according to Eq. 2.10, the temporal energy loss through the gravitational slingshot mechanism remains constant throughout the evolution of a SMBHB.
Since the temporal change of the orbital frequency f_{orb} of a binary system is required for calculating the GW signal of individual SMBHBs in Subsec. 2.5, the corresponding expression should also be provided in this context. By using the well-known relation between a and f_{orb} for Keplerian orbits, $f_{\mathrm{orb}} = \frac{1}{2\pi}\sqrt{\frac{GM}{a^3}}$, it follows

$$\begin{aligned}\left.\frac{df_{\mathrm{orb}}}{dt_r}\right|_{\mathrm{3B}} &= \left.\frac{\partial f_{\mathrm{orb}}}{\partial a}\,\frac{da}{dt_r}\right|_{\mathrm{3B}} = \frac{3}{4\pi}\,HG^{3/2}M^{1/2}\,\frac{\rho}{\sigma}\,a^{-1/2} \\ &= \frac{3}{2(2\pi)^{2/3}}\,HG^{4/3}(m_1(1+q))^{1/3}\,\frac{\rho}{\sigma}\,f_{\mathrm{orb}}^{1/3} \,.\end{aligned} \tag{2.11}$$

To obtain the temporal change of the eccentricity e, Eq. 2.3 is first rearranged to

$$K = \left(\frac{de}{dt_r} \left(\frac{d\ln(1/a)}{dt_r} \right)^{-1} \right) \Bigg|_{\text{3B}} = \frac{de}{dt_r}\Bigg|_{\text{3B}} \left(\frac{\partial \ln(1/a)}{\partial a} \frac{da}{dt_r}\Bigg|_{\text{3B}} \right)^{-1} . \tag{2.12}$$

Substituting the expression for $\frac{da}{dt_r}\Big|_{\text{3B}}$ from Eq. 2.9 and solving the resulting equation for $\frac{de}{dt_r}\Big|_{\text{3B}}$ gives

$$\frac{de}{dt_r}\Bigg|_{\text{3B}} = HKG \frac{\rho}{\sigma} a . \tag{2.13}$$

In addition, rearranging Eq. 2.8 to solve for e and differentiating the result with respect to t_r leads to

$$\begin{aligned} \frac{de}{dt_r}\Bigg|_{\text{3B}} &= \frac{d}{dt_r} \left(1 + \frac{2E_{\text{orb}}}{\mu} \left(\frac{L_{\text{orb}}}{\mu G M} \right)^2 \right)^{1/2} \Bigg|_{\text{3B}} \\ &= \frac{1}{2e} \left[\frac{2}{\mu} \frac{dE_{\text{orb}}}{dt_r}\Bigg|_{\text{3B}} \left(\frac{L_{\text{orb}}}{\mu G M} \right)^2 + \frac{2E_{\text{orb}}}{\mu} \frac{2L_{\text{orb}}}{(\mu G M)^2} \frac{dL_{\text{orb}}}{dt_r}\Bigg|_{\text{3B}} \right] \\ &= \frac{e^2 - 1}{2e} \left(\frac{dE_{\text{3B}}}{dt_r} \frac{1}{E_{\text{orb}}} + 2 \frac{dL_{\text{3B}}}{dt_r} \frac{1}{L_{\text{orb}}} \right) , \end{aligned} \tag{2.14}$$

for the case where energy and angular momentum of the SMBHB are lost solely due to the gravitational slingshot effect. Inserting the known expression for E_{orb} from Eq. 2.7 and $\frac{dE_{\text{3B}}}{dt_r}$ from Eq. 2.10 gives

$$\begin{aligned} \frac{de}{dt_r}\Bigg|_{\text{3B}} &= \frac{e^2 - 1}{2e} \left(\frac{HG^2 M \mu \rho}{2\sigma} \frac{2a}{GM\mu} + 2 \frac{dL_{\text{3B}}}{dt_r} \frac{1}{L_{\text{orb}}} \right) \\ &= HG \frac{\rho}{\sigma} a \underbrace{\left[\frac{e^2 - 1}{e} \left(\frac{1}{2} + \frac{\sigma}{HG\rho a} \frac{dL_{\text{3B}}}{dt_r} \frac{1}{L_{\text{orb}}} \right) \right]}_{= K} . \end{aligned} \tag{2.15}$$

By comparing Eq. 2.15 with Eq. 2.13, K can be identified as[28]

$$K = \frac{e^2 - 1}{e} \left(\frac{1}{2} + \frac{\sigma}{HG\rho a} \frac{dL_{\text{3B}}}{dt_r} \frac{1}{L_{\text{orb}}} \right) = \frac{e^2 - 1}{e} \left[\frac{1}{2} + \left(\frac{dE_{\text{3B}}}{dt_r} \right)^{-1} E_{\text{orb}} \frac{dL_{\text{3B}}}{dt_r} \frac{1}{L_{\text{orb}}} \right] . \tag{2.16}$$

[28] While this expression describes the "full" change in eccentricity over time, Eq. 12 in Ref. [69] only refers to the change caused by a single scattering event.

Finally, this equation can be solved for the sought expression for the angular momentum loss due to the considered hardening mechanism. The result is

$$\begin{aligned}\frac{dL_{3B}}{dt_r} &= -HG\,\frac{\rho}{\sigma}\,a\,L_{\mathrm{orb}}\left(\frac{e}{1-e^2}\,K+\frac{1}{2}\right)\\ &= -H\,\frac{\rho}{\sigma}\,\mu\sqrt{G^3Ma^3(1-e^2)}\left(\frac{e}{1-e^2}\,K+\frac{1}{2}\right)\,,\end{aligned} \tag{2.17}$$

where Eq. 2.8 is used in the last step.

Through above equations, the influence of the gravitational slingshot mechanism on the evolution of a SMBHB in a background of field stars is fully described. In the following subsection, the emission of GWs will be considered as another effect that removes energy and angular momentum from a binary system.

2.3 Radiation of Gravitational Waves

At the beginning of this subsection, important fundamental properties of GWs are discussed. Detailed derivations are omitted. These can be found, for example, in Ref. [95].

GWs are tiny distortions of spacetime that propagate at the speed of light c in vacuum. They are generated by accelerated masses or, more precisely, distributions of matter/energy in the universe that exhibit a time-dependent change in their quadrupole moment. This necessary quadrupolar character is exhibited, for example, by binary systems of astrophysical objects such as black holes of different masses or neutron stars. This work focuses on SMBHBs.

Mathematically, GWs are solutions to the Einstein field equations (EFE) of GR expanded to linear order in a small perturbation $h_{\mu\nu}$ (with $|h_{\mu\nu}| \ll 1$) of the flat spacetime metric $\eta_{\mu\nu}$, also known as Minkowski metric (commonly referred to as the linearized EFE):

$$\Box h_{\mu\nu} = -\frac{16\pi G}{c^4}\,T_{\mu\nu} \quad \text{(inside a source)}\,, \qquad \Box h_{\mu\nu} = 0 \quad \text{(in vacuum)}\,. \tag{2.18}$$

Here, $T_{\mu\nu}$ represents the energy-momentum tensor of the GW source and $\Box = \partial^\mu\partial_\mu$ denotes the flat-space d'Alembert operator. By choosing appropriate gauges, the number of independent entries of the symmetric tensor $h_{\mu\nu}$ can be reduced from ten to two in the vacuum case. These two degrees of freedom correspond to the polarization modes of a GW and are typically referred to as *plus* (+) and *cross* (×). Additionally, the quantity that is usually used to specify the GW

signal of an inspiraling SMBHB is the dimensionless characteristic strain[29] h_c which depends on the GW frequency f in the reference frame of a detector[30]. Due to the Hubble expansion of the universe [96], a GW experiences a redshift, denoted as z, on its journey from its source to the detector. Consequently, the frequency f_r at which a GW is emitted in the rest frame of the SMBHB does not correspond to the frequency f that the GW has when it reaches the detector. However, these two frequencies are related by $f_r = (1+z)f$.

Since the two components of SMBHBs can generally move on eccentric orbits, the frequency f_r of the GWs emitted by these binary systems is not limited to twice their orbital frequency f_{orb}, i.e., $f_r = 2f_{\mathrm{orb}}$, as it would be the case for circular orbits. Rather, the GW signal is a superposition of emissions at different multiples $n \in \mathbb{N}$ of f_{orb}, referred to as *harmonics* [97]. These *discrete* GW frequencies are therefore $f_r = nf_{\mathrm{orb}}$. The consideration of higher orders becomes increasingly important as the eccentricity e of the orbits increases. Nevertheless, since the emission of GWs is always associated with a loss of energy and angular momentum, causing a permanent increase of f_{orb} over time, the resulting gravitational wave spectrum of an individual SMBHB is not discrete but rather *continuous*.

It is expected that the radiation of GWs dominates the final phase of the SMBHB's evolution until coalescence. This last phase is initiated once the energy loss due to the gravitational slingshot effect and GW emission are in equilibrium (see Subsec. 2.4). According to Refs. [98], [95] and [99], the corresponding expressions for the energy and angular momentum loss averaged over one orbital period are given by

$$\begin{aligned}\frac{dE_{\mathrm{GW}}}{dt_r} &= \sum_{n=1}^{\infty} \frac{dE_{\mathrm{GW},n}}{dt_r} = \sum_{n=1}^{\infty} \frac{dE_{\mathrm{GW,circ}}}{dt_r}\, g(n,e) \\ &= -\frac{32}{5}\,\frac{G^4\mu^2M^3}{c^5a^5} \sum_{n=1}^{\infty} g(n,e) = -\frac{32}{5}\,\frac{G^4\mu^2M^3}{c^5a^5}\, F(e)\ ,\end{aligned} \tag{2.19}$$

$$\frac{dL_{\mathrm{GW}}}{dt_r} = -\frac{32}{5}\,\frac{G^{7/2}\mu^2M^{5/2}}{c^5a^{7/2}}\,\frac{1}{(1-e^2)^2}\left(1+\frac{7}{8}e^2\right)\ , \tag{2.20}$$

[29] The characteristic strain is not a directly measurable quantity but rather a theoretical concept that provides a practical way to describe the strength of a GW signal. It is particularly useful for comparing theoretical predictions of GW signals with the sensitivity of detectors.

[30] As evident from Subsec. 1.2, PTAs are not detectors localized in one place, as the pulsars used are distributed across the Milky Way. The reference frame typically employed in this framework is the barycenter of the solar system.

with

$$F(e) = \sum_{n=1}^{\infty} g(n,e) = \frac{1}{(1-e^2)^{7/2}} \left(1 + \frac{73}{24}e^2 + \frac{37}{96}e^4\right) . \tag{2.21}$$

Here, $n \in \mathbb{N}$ corresponds to the order of the harmonic, $\frac{dE_{\mathrm{GW},n}}{dt_r}$ is the energy emission rate in the n-th harmonic and $\frac{dE_{\mathrm{GW},circ}}{dt_r}$ is the corresponding emission rate for circular orbits. In addition, $g(n,e)$ is the GW frequency distribution function, defined by

$$\begin{aligned} g(n,e) = \frac{n^4}{32} \Bigg[&\Big(J_{n-2}(ne) - 2eJ_{n-1}(ne) + \frac{2}{n}J_n(ne) + 2eJ_{n+1}(ne) - J_{n+2}(ne) \Big)^2 \\ &+ (1-e^2)\left(J_{n-2}(ne) - 2J_n(ne) + J_{n+2}(ne)\right)^2 + \frac{4}{3n^2}\left(J_n(ne)\right)^2 \Bigg] , \end{aligned} \tag{2.22}$$

where $J_n(x)$ are the n-th order Bessel functions of the first kind. Since $J_n(0) = \delta_{n0}$, in the case of circular orbits ($e = 0$) follows $g(n,0) = \delta_{n2}$. Using above equations, the corresponding time evolution of the orbital parameters a, f_{orb} and e are derived below.
For the temporal change of a, the result is as follows:

$$\left.\frac{da}{dt_r}\right|_{\mathrm{GW}} = \left.\frac{dE_{\mathrm{orb}}}{dt_r}\right|_{\mathrm{GW}} \left(\frac{\partial E_{\mathrm{orb}}}{\partial a}\right)^{-1} = \frac{dE_{\mathrm{GW}}}{dt_r} \left(\frac{\partial E_{\mathrm{orb}}}{\partial a}\right)^{-1} = -\frac{64}{5}\frac{G^3\mu M^2}{c^5 a^3} F(e) . \tag{2.23}$$

Analogous to the previous subsection, for the orbital frequency applies

$$\begin{aligned} \left.\frac{df_{\mathrm{orb}}}{dt_r}\right|_{\mathrm{GW}} &= \frac{\partial f_{\mathrm{orb}}}{\partial a}\left.\frac{da}{dt_r}\right|_{\mathrm{GW}} = \frac{48}{5\pi}\frac{G^{7/2}\mu M^{5/2}}{c^5} F(e)\, a^{-11/2} \\ &= \frac{96}{5}\frac{(2\pi)^{8/3} G^{5/3}}{c^5}\frac{m_1^{5/3} q}{(1+q)^{1/3}} F(e)\, f_{\mathrm{orb}}^{11/3} . \end{aligned} \tag{2.24}$$

Finally, the expression for $\left.\frac{de}{dt_r}\right|_{\mathrm{GW}}$ can be obtained by using Eq. 2.14 in relation to GW emission

$$\begin{aligned} \left.\frac{de}{dt_r}\right|_{\mathrm{GW}} &= \frac{e^2-1}{2e}\left(\frac{dE_{\mathrm{GW}}}{dt_r}\frac{1}{E_{\mathrm{orb}}} + 2\frac{dL_{\mathrm{GW}}}{dt_r}\frac{1}{L_{\mathrm{orb}}}\right) \\ &= \frac{e^2-1}{2e}\left[\frac{32}{5}\frac{G^4\mu^2 M^3}{c^5 a^5}\frac{2a\,F(e)}{G\mu M} - \frac{64}{5}\frac{G^{7/2}\mu^2 M^{5/2}}{c^5 a^{7/2}\left(1-e^2\right)^2}\frac{1+\frac{7}{8}e^2}{\mu\sqrt{GMa(1-e^2)}}\right] \\ &= -\frac{32}{5}\frac{G^3\mu M^2}{c^5 a^4\left(1-e^2\right)^{5/2}}\left[\frac{1}{e}\left(1 + \frac{73}{24}e^2 + \frac{37}{96}e^4\right) - \frac{1-e^2}{e}\left(1 + \frac{7}{8}e^2\right)\right] \end{aligned}$$

$$= -\frac{32}{5}\frac{G^3\mu M^2}{c^5 a^4}\frac{e\left(\frac{19}{6}+\frac{121}{96}e^2\right)}{\left(1-e^2\right)^{5/2}} = -\frac{304}{15}\frac{G^3\mu M^2}{c^5 a^4}\frac{e\left(1+\frac{121}{304}e^2\right)}{\left(1-e^2\right)^{5/2}}\,, \tag{2.25}$$

where Eqs. 2.7 and 2.8 are used in the first step. The global minus sign in Eq. 2.25 indicates that the emission of GWs leads to the circularization of the SMBHs' orbits. Therefore, the effect discussed in this subsection has the opposite impact on the eccentricity evolution compared to the gravitational slingshot mechanism.

2.4 Energy and Angular Momentum Balance

As shown in the previous subsections, ejections of unbound stars from galactic centers through 3-body interactions and the radiation of GWs result in the loss of energy and angular momentum of a SMBHB. Consequently, its two components gradually approach each other until they finally merge into an even more massive SMBH[31]. By combining these two effects, the energy and angular momentum balance for an *individual* SMBHB can be formulated as

$$\frac{dE_{\rm orb}}{dt_r} = \frac{dE_{\rm 3B}}{dt_r} + \frac{dE_{\rm GW}}{dt_r}\,, \tag{2.26}$$

$$\frac{dL_{\rm orb}}{dt_r} = \frac{dL_{\rm 3B}}{dt_r} + \frac{dL_{\rm GW}}{dt_r}\,. \tag{2.27}$$

Additionally, the impact of both mechanisms on the eccentricity e and the semi-major axis a can be specified as follows:

$$\frac{da}{dt_r} = \left.\frac{da}{dt_r}\right|_{\rm 3B} + \left.\frac{da}{dt_r}\right|_{\rm GW}\,, \tag{2.28}$$

$$\frac{de}{dt_r} = \left.\frac{de}{dt_r}\right|_{\rm 3B} + \left.\frac{de}{dt_r}\right|_{\rm GW}\,. \tag{2.29}$$

To calculate the SGWB from inspiraling SMBHBs, the values of $a(t_r)$ and $e(t_r)$ are required. For this, the two coupled differential equations can be solved numerically using the `SMBHBpy` code (see Subsec. 3.1) for given initial conditions $a(0) = a_0 = r_{\rm infl}$ and $e(0) = e_0$.

To conclude this subsection, a brief derivation of the semi-major axis $a_{\rm 3B,GW}$, at which a SMBHB loses an equal amount of energy through the gravitational slingshot effect as through GW

[31] It should be noted that the process of the merger cannot be described within the Newtonian approximation. For this, full-GR simulations are required.

emission, is provided. The dependencies of this quantity on ρ/σ and the eccentricity e will play a role in the analysis and explanation of certain results in Chap. 4.
By setting the expressions from Eq. 2.10 and Eq. 2.19 equal to each other and rearranging the resulting equation for a, one obtains

$$a_{\mathrm{3B,GW}} = \left(\frac{64}{5} \frac{G^2 \mu M^2}{H c^5} \frac{\sigma}{\rho} F(e = e_{\mathrm{3B,GW}}) \right)^{1/5} . \tag{2.30}$$

As can be seen from this equation, $a_{\mathrm{3B,GW}}$ also depends on the corresponding value of the eccentricity $e_{\mathrm{3B,GW}}$ at the equilibrium. The larger $e_{\mathrm{3B,GW}}$, the greater $a_{\mathrm{3B,GW}}$ becomes. However, this dependence is relatively weak, since $(F(e))^{1/5} \in [1, 20.8]$ for $e \in [0, 0.99]$ (see Eq. 2.21). Moreover, $a_{\mathrm{3B,GW}}$ decreases and thus the fraction of the total evolution dominated by the ejection of stars through 3-body interactions naturally increases with increasing ρ/σ. Based on the results from the last two subsections, $a_{\mathrm{3B,GW}}$ also corresponds to the point beyond which the orbits of the SMBHs become circularized rather than more eccentric.
In the next two subsections, the theoretical foundation for calculating the GW signal of individual SMBHBs will be provided, before connecting this to the SGWB of a SMBHB population.

2.5 Characteristic Strain of Individual Eccentric SMBHBs

As mentioned before, the GW signal from an eccentric SMBHB that reaches a detector is the interference of (infinitely) many partial signals, referred to as harmonics. To the resulting GW signal, a characteristic strain $h_c(f)$ can be assigned, which corresponds to the quadratic sum of the characteristic amplitudes $h_{c,n}(f)$ of all harmonics:

$$h_c(f) = \left(\sum_{n=1}^{\infty} h_{c,n}^2(f) \right)^{1/2} . \tag{2.31}$$

Here, $f = f_r/(1+z) = n f_{\mathrm{orb}}/(1+z)$ is the observed GW frequency, i.e., the frequency in the rest frame of the detector. Additionally, $h_{c,n}(f)$ can be expressed as [100]

$$h_{c,n}^2(f) = \frac{2(1+z) f^2}{\dot{f}} h_n^2(f) , \quad \text{with} \quad \dot{f} = \frac{df}{dt_r} = \frac{n}{1+z} \frac{df_{\mathrm{orb}}}{dt_r} . \tag{2.32}$$

Since this work assumes that a SMBHB loses energy trough both GW emission and the gravitational slingshot mechanism, the total temporal change of its orbital frequency f_{orb} is given

by

$$\frac{df_{\rm orb}}{dt_r} = \left.\frac{df_{\rm orb}}{dt_r}\right|_{\rm 3B} + \left.\frac{df_{\rm orb}}{dt_r}\right|_{\rm GW} . \tag{2.33}$$

In Eq. 2.32, $h_n(f)$ represents the dimensionless root-mean-square amplitude of the n-th harmonic defined by [45], [99]–[101]

$$\begin{aligned} h_n(f) &= \sqrt{\left\langle h_{n,+}^2(f,\vec{n}) + h_{n,\times}^2(f,\vec{n})\right\rangle} = \frac{G^{1/2}}{c^{3/2}}\frac{1}{\pi f D_L(z)}\sqrt{-\frac{dE_{{\rm GW},n}}{dt_r}} \\ &= \frac{G^{1/2}}{c^{3/2}}\frac{1}{\pi f D_L(z)}\left(\frac{32}{5}\frac{G^4\mu^2M^3}{c^5}g(n,e)\right)^{1/2}\left[\frac{(2\pi f_{\rm orb})^2}{GM}\right]^{5/6} \\ &= \sqrt{\frac{32}{5}}\frac{G^{5/3}}{c^4}\frac{\mu M^{2/3}}{\pi f D_L(z)}(2\pi f_{\rm orb})^{5/3}\sqrt{g(n,e)} \\ &= \sqrt{\frac{32}{5}}\frac{G^{5/3}}{c^4}\frac{\mathcal{M}_c^{5/3}}{\pi f D_L(z)}\left(2\pi\frac{(1+z)f}{n}\right)^{5/3}\sqrt{g(n,e)}\,. \end{aligned} \tag{2.34}$$

Here, $h_{n,+}(f,\vec{n})$ and $h_{n,\times}(f,\vec{n})$ are the amplitudes of two polarizations of the GW emitted in the direction $\vec{n}$. Furthermore, $\langle ... \rangle$ denotes the average over a wave period and over $\vec{n}$, which can also be regarded as the GW source orientations relative to the detector. To obtain the result in the second line of Eq. 2.34, the expression for $\frac{dE_{{\rm GW},n}}{dt_r}$ from Eq. 2.19 is used. Additionally, the chirp mass,

$$\mathcal{M}_c = \mu^{3/5}M^{2/5} = \left(\frac{q^3}{1+q}\right)^{1/5} m_1\,, \tag{2.35}$$

is introduced in the last step. Finally, $D_L(z)$ stands for the luminosity distance [102] of the GW source depending on the redshift z. For a flat ($\Omega_k = 0$) universe with Friedmann-Lemaître-Robertson-Walker metric the relation between $D_L(z)$ and z is given by [103]

$$D_L(z) = \frac{(1+z)c}{H_0}\int_0^z \frac{dz'}{E(z')}\,, \quad \text{with} \quad E(z') = \sqrt{\Omega_R(1+z')^4 + \Omega_M(1+z')^3 + \Omega_\Lambda}\,, \tag{2.36}$$

where $H_0 = 67.66\,{\rm Mpc}^{-1}\,{\rm km/s}$ is the Hubble constant, $\Omega_R \approx 10^{-4}$ is today's radiation density, which is usually neglected, $\Omega_M = 0.31$ today's matter (dark and baryonic) density and $\Omega_\Lambda = 0.69$ today's dark energy density [70].

2.6 Astrophysical SGWB from SMBHB Populations

As mentioned at the beginning of this work, there are many different astrophysical as well as cosmological sources and processes that are expected to generate a SGWB. The observation of the Hellings-Downs correlation in the recent PTA data from NANOGrav strongly suggests the existence of an isotropic SGWB in the nanohertz frequency range of the GW spectrum. In this work, it is considered that this stochastic background is produced by a *stationary* population of eccentric SMBHBs. Furthermore, it is assumed that these SMBHBs lose energy and angular momentum not only through the radiation of GWs but also through slingshot ejections of stars from the center of their host galaxies. Both effects have been described in detail in the preceding subsections.

Based on this, the expression for the characteristic strain $h_{c,\mathrm{SGWB}}(f)$ of the SGWB, which is implemented into the `SMBHBpy` code, will be derived in the following.

In the literature, the starting point for computing the SGWB is typically Phinney's theorem [104]. This theorem connects $h_{c,\mathrm{SGWB}}(f)$ with the comoving number density[32] $\frac{d^3n}{dzdm_1dq}\,dzdm_1dq$ of SMBHBs in the universe and the total GW energy spectrum $\frac{dE_{\mathrm{GW}}}{df_r}$ in the frequency domain of *individual* binary systems. It reads

$$h^2_{c,\mathrm{SGWB}}(f) = \frac{4G}{\pi f c^2} \int dz \int dm_1 \int dq \, \frac{d^3n}{dzdm_1dq} \left| \frac{dE_{\mathrm{GW}}}{df_r} \right| , \tag{2.37}$$

with

$$\begin{aligned} \left| \frac{dE_{\mathrm{GW}}}{df_r} \right| &= -\frac{dE_{\mathrm{GW}}}{df_r} = -\sum_{n=1}^{\infty} \frac{dE_{\mathrm{GW},n}}{df_r} = -\sum_{n=1}^{\infty} \frac{dE_{\mathrm{GW},n}}{dt_r} \frac{dt_r}{df_r} \\ &= -\sum_{n=1}^{\infty} \frac{dE_{\mathrm{GW,circ}}}{dt_r} \frac{dt_r}{df_r} \, g(n,e) = -\sum_{n=1}^{\infty} \frac{dE_{\mathrm{GW,circ}}}{dt_r} \frac{\tau(f)}{f(1+z)} \, g(n,e) , \end{aligned} \tag{2.38}$$

where the timescale $\tau(f)$ of GW emission and stellar hardening is introduced, defined by

$$\tau(f) = f \, \frac{1}{\dot{f}} . \tag{2.39}$$

[32] The comoving number density refers to the number of SMBHBs per unit volume that factors out the expansion of the universe and thus remains constant over time.

In order to better illustrate mathematically that the SGWB is indeed the superposition of the GW signals from individual SMBHBs, the comoving number density can first be written as

$$\frac{d^3n}{dzdm_1dq} = \frac{d^4\mathcal{N}}{dzdm_1dqd\ln(f_r)}\,\frac{dz}{dV_c}\,\frac{dt_r}{dz}\,\frac{d\ln(f_r)}{dt_r}\,, \quad \text{with} \quad n = \frac{d\mathcal{N}}{dV_c}\,. \tag{2.40}$$

Here, $\frac{d^4\mathcal{N}}{dzdm_1dqd\ln(f_r)}$ represents the comoving number of SMBHBs emitting GWs in a given logarithmic frequency interval with parameters z, m_1, and q in the range $[z, z+dz]$, $[m_1, m_1+dm_1]$, and $[q, q+dq]$, respectively [105]. Furthermore, dV_c denotes the comoving volume shell between z and $z+dz$, and $\frac{dt_r}{dz}$ is the relation between the time t_r in the rest frame of the GW source and redshift z, described by [104]

$$\frac{dt_r}{dz} = \frac{1}{H_0(1+z)E(z)}\,. \tag{2.41}$$

Additionally, $\frac{dV_c}{dz}$ is given by

$$\frac{dV_c}{dz} = \frac{4\pi c}{H_0E(z)}\,\frac{D_L^2(z)}{(1+z)^2}\,, \tag{2.42}$$

with $E(z)$ from Eq. 2.36 [102]. By substituting Eq. 2.40 in Eq. 2.37 and using the above cosmological correlations, one obtains

$$\begin{aligned} h^2_{c,\mathrm{SGWB}}(f) &= \frac{4G}{\pi f c^2}\int dz \int dm_1 \int dq \sum_{n=1}^{\infty}\left(\frac{d^4\mathcal{N}}{dzdm_1dqd\ln(f_r)}\,\frac{dz}{dV_c}\,\frac{dt_r}{dz}\,\frac{d\ln(f_r)}{dt_r}\,\left|\frac{dE_{\mathrm{GW},n}}{df_r}\right|\right)\Bigg|_{f_r=(1+z)f} \\ &= \int dz \int dm_1 \int dq \sum_{n=1}^{\infty}\left(\frac{d^4\mathcal{N}}{dzdm_1dqd\ln(f_r)}\,\frac{G(1+z)\dot{f}}{\pi^2c^3D_L^2(z)f^2}\,\left|\frac{dE_{\mathrm{GW},n}}{df_r}\right|\right)\Bigg|_{f_r=(1+z)f} \\ &= \int dz \int dm_1 \int dq \sum_{n=1}^{\infty}\left.\frac{d^4\mathcal{N}}{dzdm_1dqd\ln(f_r)}\right|_{f_r=(1+z)f} h_n^2(f)\,, \end{aligned} \tag{2.43}$$

where the relation between $\left|\frac{dE_{\mathrm{GW},n}}{df_r}\right|$ and the strain $h_n(f)$ of the n-th harmonic from Eq. 2.34, i.e.,

$$\left|\frac{dE_{\mathrm{GW},n}}{df_r}\right| = -\frac{dE_{\mathrm{GW},n}}{df_r} = \frac{\pi^2c^3D_L^2(z)f^2}{G(1+z)\dot{f}}\,h_n^2(f) = \frac{\pi^2c^3}{2G}\,\frac{D_L^2(z)}{(1+z)^2}\,\underbrace{\frac{2(1+z)f^2}{\dot{f}}\,h_n^2(f)}_{=h^2_{c,n}(f)}\,, \tag{2.44}$$

is used in the last step. As can be seen from Eq. 2.43, the squared characteristic strain $h^2_{c,\mathrm{SGWB}}(f)$ of the observed SGWB is the integral over all GW sources, with the contribution of each SMBHB corresponding to the sum of the strain squares $h^2_n(f)$ for each harmonic n. Despite this simple interpretation, Eq. 2.37 is generally preferred over Eq. 2.43, as the comoving number density (and not the comoving number of binary systems) is the essential component for modeling SMBHB populations. This quantity will be discussed in more detail below.

As mentioned at the beginning of this work, it is expected that SMBHBs form through the merger of two massive galaxies. As shown in Refs. [106] and [61], the galaxy merger rate and consequently $\frac{d^3n}{dzdm_1dq}$ can be derived from the galaxy stellar mass function, the galaxy pair fraction, the typical merger timescale for a galaxy pair, and different relations connecting SMBHBs and their host galaxies. The most widely used and general approach for the SMBHB distribution function, which considers all the aforementioned cosmological quantities, was first developed by Ref. [107]. Adapted to this study, it is given by

$$\frac{d^3n}{dzdm_1dq} = \dot{n}_0 \left(\frac{m_1}{10^7 M_\odot}\right)^{-\alpha} e^{-m_1/M_*}\, e^{-z/z_*}\, (1+z)^{\beta_z}\, q^{\gamma_*}\, \frac{dt_r}{dz}\,, \tag{2.45}$$

where $\{\dot{n}_0, \alpha, M_*, z_*, \beta_z, \gamma_*\}$ are the free parameters of the population model [42], [61]. The parameter $\dot{n}_0$ is usually expressed in the unit $\mathrm{Mpc}^{-3}\,\mathrm{Gyr}^{-1}$ and M_* in solar masses $\mathrm{M}_\odot$. The other parameters are dimensionless[33].

As evident from Eq. 2.45, the above distribution of SMBHBs does not depend on quantities, such as the initial eccentricity e_0, or on parameters like H, ρ, or σ, which characterize the gravitational slingshot effect[34]. When calculating the SGWB of a SMBHB population, it is therefore explicitly assumed that these parameters, or at least related ones[35], are identical for all binary systems within the same population. However, since these quantities generally depend on the SMBH masses as well as the evolutionary history of a SMBHB and its host galaxy, this assumption only makes sense if (at least) the other binary parameters covered by $\frac{d^3n}{dzdm_1dq}$, namely z, m_1, and q, are also very similar or identical across the population.

[33] Constraints on the ranges of these parameters can be found, for example, in Ref. [107] or Ref. [61].

[34] Due to the lack of observational data as well as theoretical knowledge about the dynamics of SMBHBs and their environments, it is not possible to specify any realistic eccentricity or density distribution across the population.

[35] As mentioned before, ρ as the stellar density at the influence radius, can be calculated for the case that the expression for the matter density distribution in a SMBHB is known. For instance, if the density is not constant, it may depend on parameters like the slope s and the normalization constant ρ_{norm} of the profile. In such a case, it is not ρ, but rather s and ρ_{norm} that are the mentioned related parameters, which are assumed to be the same for all SMBHBs in the population.

For this reason, this study assumes that the population can be replaced by N *identical* SMBHBs that are distributed in the local universe and whose GW signals dominate the SGWB in the nanohertz frequency range[36]. These binary systems would thus serve as a good representation of the whole population. Furthermore, such a *discrete* distribution of SMBHBs better reflects the physical reality in the universe than a continuous one, as considered in Eq. 2.45. In this case, the corresponding distribution function can be written as

$$\begin{aligned} \left.\frac{d^3n}{dz dm_1 dq}\right|_{\mathrm{id}} &= \underbrace{\tilde{n}_0\, N}_{=A_0}\, \delta(z-z_0)\, \delta(m_1-m_{1,0})\, \delta(q-q_0) \\ &= A_0\, \delta(z-z_0)\, \delta(m_1-m_{1,0})\, \delta(q-q_0)\ , \end{aligned} \tag{2.46}$$

where $\delta(x)$ is the Dirac delta distribution and $\tilde{n}_0$ as well as N are the free parameters of this SMBHB distribution function, which can be combined into A_0. Thus, the number of free model parameters has been reduced from six to one compared to Eq. 2.45. In this work, A_0 is referred to as the number density normalization and has therefore the unit Mpc^{-3}. This quantity is directly related to the level of the SGWB. In addition, the abbreviation "id" signifies that identical SMBHBs are considered.

As shown in Refs. [16] and [37], the SMBHBs whose GW signals contribute most to the SGWB in the nanohertz frequency regime and thus dominate this stochastic background have a redshift of $z \approx 0.3$, which corresponds to a luminosity distance of $D_L \approx 1.6\,\mathrm{Gpc}$ (see Eq. 2.36), a mass ratio of $q \approx 0.65$, and total masses M of a few $10^9\,\mathrm{M}_\odot$ (to be more precise, $M \approx 10^9\,\mathrm{M}_\odot - 8\times10^9\,\mathrm{M}_\odot$). Therefore, in this work, $z_0 = 0.3$, $q_0 = 0.65$, and $M_0 = m_{1,0}(1+q_0) = 4.95\times10^9\,\mathrm{M}_\odot$, i.e., $m_{1,0} = 3\times10^9\,\mathrm{M}_\odot$, are chosen.

Before the formula used in the `SMBHBpy` code to calculate $h_{c,\mathrm{SGWB}}(f)$ can be provided, another restriction needs to be made. In Eq. 2.37, the contributions of an infinite number of harmonics are summed up for eccentric SMBHBs. Since this cannot be practically realized with a computer, an upper bound for n has to be selected. However, it is important to ensure that still a sufficient number of harmonics is considered so that the deviation from the exact value for $h_{c,\mathrm{SGWB}}(f)$ is negligible. In this study, the order n_{max} of the last non-neglected harmonic is

[36] One great advantage of this approach is that the total computing time of the Markov Chain Monte Carlo sampling algorithm (see Subsec. 3.2) is reduced by several hours to a few days depending on N, as the differential equations for the temporal evolution of the orbital parameters a and e need to be solved only once per parameter combination.

defined as $n_{\max}(e, \xi_{\text{peak}}) = \xi_{\text{peak}} \times \min\{m \in \mathbb{N} : m \geq n_{\text{peak}}(e)\}$, with

$$n_{\text{peak}}(e) = 2 \left(1 + \sum_{k=1}^{4} c_k e^k\right) (1 - e^2)^{-3/2} , \tag{2.47}$$

where $c_1 = -1.01678$, $c_2 = 5.57372$, $c_3 = -4.9271$, $c_4 = 1.68506$, and $\xi_{\text{peak}} \in \mathbb{N}$ [108]. Here, n_{peak} is a numerical approximation for the harmonic in which the maximum GW power is emitted[37]. The factor ξ_{peak} is set to $\xi_{\text{peak}} = 3$. A detailed discussion of this choice can be found in Appendix A. Furthermore, for simplicity, the number $n_{\max}$ of the considered harmonics is not varied as a function of e throughout the evolution of a SMBHB. Instead, $n_{\max}$ is determined based on the maximum eccentricity $e_{\max}$ reached by a SMBHB during its evolution, i.e., $n_{\max} = n_{\max}(e_{\max})$. This ensures that enough harmonics are taken into account at any given time. Additionally, the steep growth of $n_{\max}(e_{\max})$ is illustrated in Fig. 2.3.

Finally, by combining Eqs. 2.37, 2.38, and 2.46, one obtains [34]

$$h^2_{c,\text{SGWB}}(f) \simeq \frac{4G}{\pi f^2 c^2} \frac{A_0}{1 + z_0} \sum_{n=1}^{n_{\max}(e_{\max})} P_{\text{GW,circ}}(\Xi_0, f, n)\, \tau(\Xi_0, f, n)\, g(n, e) , \tag{2.48}$$

where $\Xi_0 = \{z_0, m_{1,0}, q_0\}$ and $P_{\text{GW,circ}} = -\frac{dE_{\text{GW,circ}}}{dt_r}$ are defined. It should be noted, that in the case of circular orbits ($e = 0$), only the contribution of the second harmonic remains, since $g(n, 0) = \delta_{n2}$. This formula will be used in this work to calculate the SGWB generated by an eccentric SMBHB population.

Moreover, for circular orbits, Eq. 2.48 can be differentiated with respect to f to determine the frequency at which $h_{c,\text{SGWB}}(f)$ reaches its maximum. This frequency, later referred to as the *turnover frequency* f_t, is given by[38]

$$f_t\Big|_{e=0} = \frac{1}{(1+z)\pi} \left(\frac{15}{128} \frac{c^5}{G^{1/3}} \frac{H\rho}{\sigma} \frac{(1+q)^{2/3}}{m_1^{4/3} q}\right)^{3/10} . \tag{2.49}$$

Unfortunately, the turnover frequency for eccentric orbits cannot be calculated analytically but numerically. However, this implies that explicit dependencies on parameters, such as a_0, e_0,

[37] From the definition of n_{peak} it is evident that $n_{\text{peak}}(e \to 1) \to \infty$. This implies that the number of harmonics that has to be considered increases significantly for high e, particularly for $e \gtrsim 0.95$ (see Fig. 2.3).

[38] Note: $f_t\big|_{e=0}$ corresponds exactly to $\left(\frac{3}{2}\right)^{3/10}$ times the GW frequency at which the transition between the 3B-dominated phase and the GW-dominated stage occurs in the SGWB spectrum of identical SMBHBs. This can be easily shown using Eq. 2.30 and the known relation between a and f for the case of circular orbits.

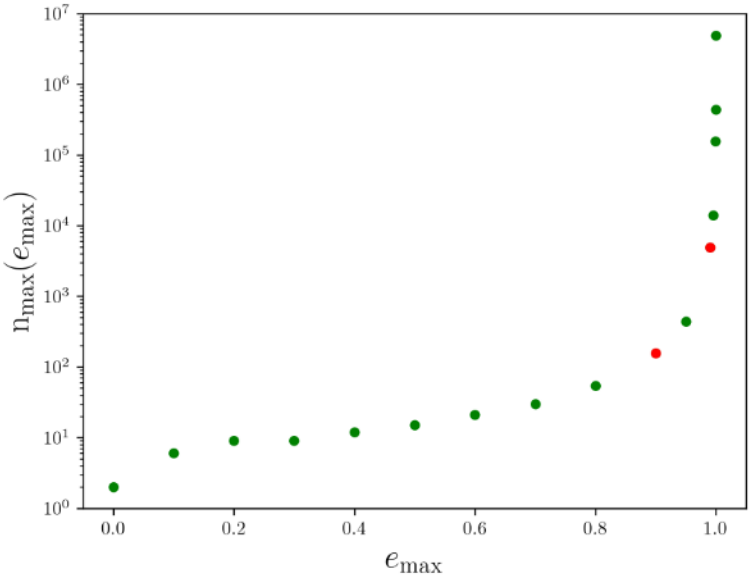

Fig. 2.3: Order of the last non-neglected harmonic $n_{\max}$ for different $e_{\max}$ using $\xi_{\text{peak}} = 3$. Additionally, the pairs (0.9, 156) and (0.99, 4,905) are marked in red, as they will later play a role for the MCMC algorithm (see Subsec. 3.2 and Tab. 4.3).

or ρ/σ get lost. As a consequence, it is not possible to make any statements about how these quantities influence f_t from a purely mathematical perspective. Nevertheless, much can be learned about these relationships by comparing the SGWB for different configuration of these parameters, as will be demonstrated in Subsec. 4.1.

To conclude the theoretical part of this thesis, it is explained in detail why $e_0, \rho/\sigma$, and A_0 are chosen as parameters for modeling the SGWB.

The exact eccentricity that the orbits of the SMBHs exhibit when they become gravitationally bound is extremely difficult to predict. Nevertheless, some studies suggest a strong correlation between the initial eccentricity e_0 at the time of SMBHB formation and the eccentricity of the galactic orbits of the SMBHs right after the merger of their initial host galaxies [109], [110]. However, since the latter is obviously subject to stochastic effects, e_0 can in principle take any allowed value. Therefore, it makes sense to consider the initial eccentricity e_0 as a model parameter in the MCMC sampling algorithm.

Furthermore, according to Eq. 2.2, the stellar density ρ and the velocity dispersion σ at r_{infl} are the key parameters that govern the hardening of a SMBHB through the ejection of stars from the center of its host galaxy. For this reason, the ratio[39] ρ/σ or, to be more precise, $\log_{10}(\rho/\sigma)$

[39]It should be noted that it is not sufficient to consider only ρ instead of ρ/σ as a model parameter. This is because ρ as the density at r_{infl} would already be fully determined by r_{infl} (and the mass M of the binary system) in the case of a constant density distribution in the SMBHB, according to Eq. 2.6. Therefore, at least one additional degree of freedom is necessary. This role is taken by σ.

is considered as another fit parameter. The influence radius r_{infl}, which corresponds to the initial semi-major axis a_0, is treated as a free binary parameter.

Both e_0 and ρ/σ, in conjunction with a_0, strongly influence the shape of the characteristic strain of the SGWB. On the other hand, the number density normalization A_0 of a population of identical SMBHBs from Eq. 2.46 is linked to the overall level of the stochastic background and is therefore also included as a model parameter.

The next chapter focuses on the implementation of the previously derived theory into the `SMBHBpy` code as well as the statistical algorithm used to determine the parameter combinations for which the theoretical model (best) fits the recent experimental data from NANOGrav and PPTA.

3 Numerical Setup

3.1 Implementation of the SGWB Calculation into the SMBHBpy Code

This subsection first provides a brief overview of the key features of the SMBHBpy code, followed by a detailed description of the main steps integrated for calculating the SGWB.

The acronym SMBHBpy refers both to the astrophysical objects the code is specialized for and to the programming language in which it is written, namely Python. The code was developed by me and works in geometrized units with $G = c = 1$, converting every unit of the physical quantities involved into parsecs before numerical processing. The underlying code structure has been adapted from the IMRIpy code by Niklas Becker [5]. Furthermore, the SMBHBpy code was also used in the context of my Bachelor thesis and the associated publication (see list of publications). However, since then, I have extended the code with several new files, such as "sgwb.py" and "mcmc_GW+3B.py", and adjusted it to handle SMBHBs as well as the orders of magnitude of their specific parameters in conjunction with their SGWB in the nanohertz frequency range.

Using the SMBHBpy code, the differential equations for the semi-major axis a and the eccentricity e can be solved numerically. In this context, Chandrasekhar's dynamical friction with dark matter spikes, the gravitational slingshot ejection of stars through 3-body interactions, and the emission of GWs can be considered as effects that remove energy and angular momentum from a SMBHB. However, for the purposes of this work, only the last two mechanisms play a role, as discussed earlier. Furthermore, both the GW spectrum of individual binary systems and the astrophysical SGWB of a *discrete* cosmic population of *identical* as well as *arbitrary* SMBHBs can be calculated. Moreover, a Markov Chain Monte Carlo sampling algorithm is available for investigating the degeneracy between the two model parameters e_0 and $\log_{10}(\rho/\sigma)$ in the case of identical SMBHBs, which is the aim of this Master thesis.

Once the temporal evolution of the orbital parameters a and e is known (for each SMBHB) and the functions $g(n, e)$, $\tau(f)$, $P_{\mathrm{GW,circ}}(f)$, and $n_{\mathrm{max}}(e_{\mathrm{max}})$ introduced in Chap. 2 have been defined in the code, the SGWB produced by N identical or arbitrary SMBHBs, which exhibit a discrete distribution function, can be calculated using the following five main steps:

Step 1 - Frequency binning: According to the discussion about the order of the last non-neglected harmonic in Appendix A, there are n_{max} different sub-spectra (one per harmonic)

contributing to the stochastic background for each SMBHB. This results in $\sum_{i=1}^{N} n_{\max}(e_{\max}(i))$ different GW frequency arrays $\mathcal{A}^{(i_n)}_{f_{\text{unbinned}}}$, with $n = 1, \ldots, n_{\max}(e_{\max}(i))$ for a fixed $i = 1, \ldots, N$, each associated with an array containing the corresponding values for the (squared) characteristic strain. However, to enable the summation of all sub-spectra with a computer, it is essential that they are defined at the same discrete frequencies $\mathcal{F}_{\text{bins}} = \{f_1, \ldots, f_{N_{\text{bins}}}\}$, where N_{bins} is the number of considered bins[40]. To achieve this, certain values from each unbinned frequency array $\mathcal{A}^{(i_n)}_{f_{\text{unbinned}}}$ are grouped together to be represented by one of N_{bins} values of $\mathcal{F}_{\text{bins}}$ that is added to a new frequency array $\mathcal{A}^{(i_n)}_{f_{\text{binned}}}$. After that, possible duplicate values are removed from $\mathcal{A}^{(i_n)}_{f_{\text{binned}}}$. Consequently, every $\mathcal{A}^{(i_n)}_{f_{\text{binned}}}$ contains a maximum[41] of N_{bins} different entries corresponding to discrete GW frequencies in the PTA band. The minimum/maximum frequency $f_1/f_{N_{\text{bins}}}$ in $\mathcal{F}_{\text{bins}}$ is chosen to match the smallest/largest bin position of the experimental data under consideration. Of course, the number of bins N_{bins} used in the code for calculating the SGWB does not necessarily need to correspond to the number of bins available from the data. In addition, it should be noted that in the case of identical SMBHBs, distinguishing between different i is not required.

Step 2 - Interpolation: Using the mathematical technique of interpolation, the characteristic strain arrays belonging to the binned frequency arrays are calculated based on the "old" ones.

Step 3 - Add zeros: As previously noted, the number of entries in all $\mathcal{A}^{(i_n)}_{f_{\text{binned}}}$ is generally not the same. This is because, for a fixed initial and final condition for the evolution of a SMBHB, each harmonic exists within a different limited frequency range in which it contributes to the SGWB. However, this range does not necessarily overlap completely with $\mathcal{F}_{\text{bins}}$. Therefore, there are values in $\mathcal{F}_{\text{bins}}$ for which no corresponding partner lives in some $\mathcal{A}^{(i_n)}_{f_{\text{binned}}}$. To ensure that all characteristic strain arrays nevertheless have the same dimension, zeros are added at positions where no value exists.

Step 4 - Summation of all sub-spectra: Due to the preliminary work, all sub-spectra can now be easily summed up. The result is the characteristic strain of the SGWB generated by the entire SMBHB population[42].

[40] In the SMBHBpy code, N_{bins} is also referred to as "fineness" in some instances.

[41] The number of values in each $\mathcal{A}^{(i_n)}_{f_{\text{binned}}}$ does not necessarily have to match the number of bins N_{bins}. This is, for example, the case when $\mathcal{A}^{(i_n)}_{f_{\text{unbinned}}}$ was not defined over the entire frequency range covered by $\mathcal{F}_{\text{bins}}$.

[42] To be more precise, according to Eq. 2.43, the squares of the sub-spectra are summed up. After that, the square root of the result is taken to obtain $h_{c,\text{SGWB}}(f)$.

Step 5 - Delete remaining zeros: The array containing the values for the characteristic strain of the SGWB could still include a few zeros, which are remnants from step 3. However, since the characteristic strain is typically plotted logarithmically, in this last step, the remaining zeros are removed from the final SGWB array, along with the corresponding GW frequencies from $\mathcal{F}_{\text{bins}}$.

Furthermore, it should be noted that this method for calculating the SGWB has been verified in several ways. For example, in Appendix B the results from Fig. 4 of Ref. [46] are reproduced almost exactly.

The `SMBHBpy` code as well as the Jupyter Notebooks used to create the plots presented in this work are available on GitHub[43].

3.2 Markov Chain Monte Carlo Sampling

Markov Chain Monte Carlo (MCMC) is a class of algorithms used to numerically approximate the multidimensional probability distribution for a complex theoretical model, starting from a given initial distribution. By combining the properties of Markov Chains with Monte Carlo sampling, these methods facilitate the efficient exploration of the underlying parameter space. In the context of astrophysical analyses, this provides an understanding of how well individual theoretical predictions fit experimental data across a broad range of the model parameters.

In the following, the mathematical foundation of MCMCs, as described in Refs. [111] and [112], is outlined, followed by a detailed explanation of their concrete application in this work.

A Markov Chain is defined as a sequence, generated step by step during the sampling process, of random samples $\{X_0, X_1, \ldots, X_{n_{\text{steps}}}\}$ with $X_i = \{\Theta_1^{(i)}, \Theta_2^{(i)}, \ldots, \Theta_{n_{\text{dim}}}^{(i)}\}$, drawn from the set of possible combinations of continuous model parameters Θ_k, with $k = 1, \ldots, n_{\text{dim}}$. Here, n_{steps} denotes the number of steps/iterations the algorithm will go through per complete run, and n_{dim} represents the dimension of X_i, corresponding to the number of considered model/fit parameters. Consequently, X_i can be interpreted as the state of the chain after the i-th step of the Monte Carlo process.

The key property of a Markov Chain is that the probability of transitioning to the next state X_{i+1} depends only on the current state X_i of the chain and not on previous states. The most commonly used MCMC algorithm to generate a Markov Chain according to this "memoryless"

[43] See https://github.com/MatthiasD25/Master_thesis-Matthias_Daniel.

principle is the Metropolis-Hastings method (see Fig. 3.1) [113], [114]. To initialize the sampling process, "good" *initial guesses* X_0 for the model parameters must be established as the starting sample of the chain. At each iteration, the algorithm proposes a candidate Y for the next sample based on a *proposal function* $Q(X_i, Y)$ which depends on X_i. This candidate is accepted as the next state of the chain, such that $X_{i+1} = Y$, if it satisfies the acceptance criterion $u < \alpha_Y$, where u is a random number from the uniform distribution $[0, 1)$ and α_Y is defined by

$$\alpha_Y = \min\left(1, \frac{P(Y|d)}{P(X_i|d)} \frac{Q(Y, X_i)}{Q(X_i, Y)}\right) . \tag{3.1}$$

Otherwise Y is discarded and the current sample is reused for the next iteration, i.e., $X_{i+1} = X_i$. In the equation above, $P(X_i|d)$ represents the chosen initial *posterior distribution* (or simply *posterior*), which serves as the basis for approximating the true posterior over the course of the MCMC algorithm. This distribution describes the probability that the specific parameter combination X_i can explain the experimental data d, given that the data are already known. Moreover, a common choice for $Q(X_i, Y)$ is a Gaussian distribution centered around X_i. In this case, $Q(X_i, Y)$ is symmetric, meaning $Q(X_i, Y) = Q(Y, X_i)$, and thus the expression for α_Y simplifies to

$$\alpha_Y^{\text{sym}} = \min\left(1, \frac{P(Y|d)}{P(X_i|d)}\right) . \tag{3.2}$$

From this equation, it is evident that Y is always accepted if $P(Y|d) \geq P(X_i|d)$. Consequently, those X_i that maximize[44] $P(X_i|d)$ are most favored by d. Finally, after a sufficient number of iterations, the Markov Chain converges to its stationary distribution (samples do not change with i anymore) that approximates the true posterior. Fig. 3.1 shows a flowchart of the complete algorithm presented above.

Next, the expression used for the initial posterior $P(X_i|d)$ is specified. To simplify notation, the index i will be omitted by defining $\Theta \equiv X_i$.

Using Bayes' theorem for conditional probabilities, $P(X_i|d) = P(\Theta|d)$ can be rewritten as

$$P(\Theta|d) = \frac{P(d|\Theta)P(\Theta)}{P(d)} \propto P(d|\Theta)P(\Theta) , \tag{3.3}$$

[44] Typically, the logarithmic posterior function $\ln(P(X_i|d))$ is maximized, which can ensure numerical stability, among other benefits. Therefore, this approach is also used in the MCMC algorithm employed in this work.

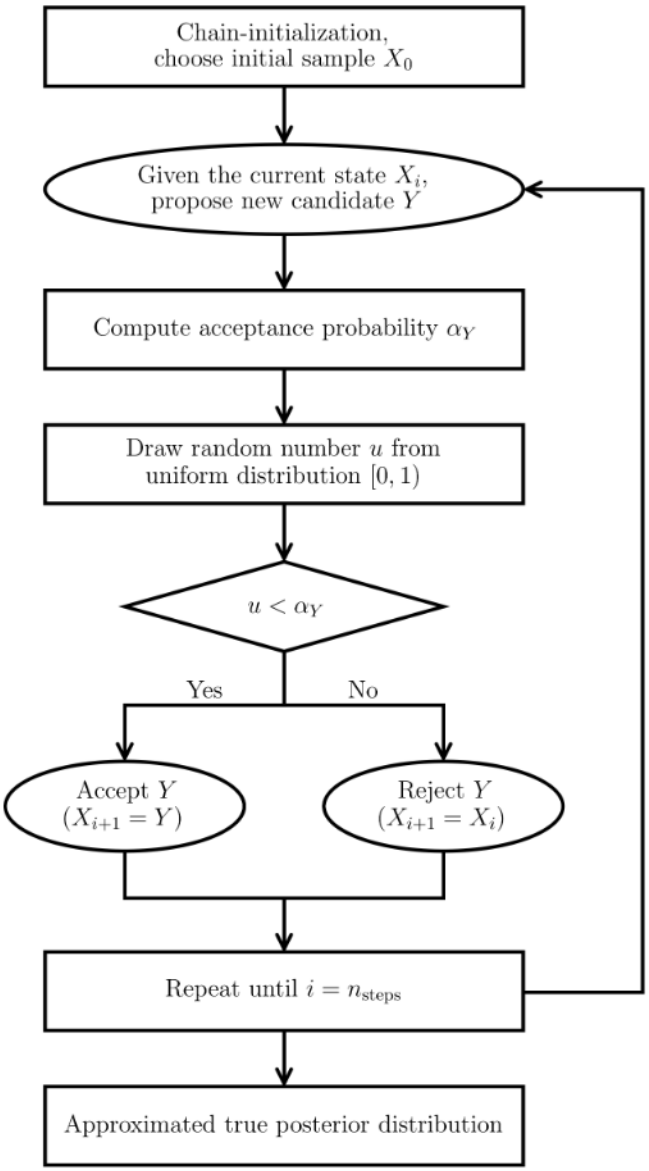

Fig. 3.1: Schematic representation of the Metropolis-Hastings MCMC algorithm (inspired by Fig. 4 of Ref. [115]). A detailed description of each step can be found in the text.

where $P(d|\Theta)$ is the *likelihood function*, $P(\Theta)$ is the *prior* distribution and $P(d)$ a normalizing constant that is called *evidence*.

The experimental data d used in this study include the measured/derived values $h_{c,\text{exp},j} = h_{c,\text{exp}}(f_j)$ of the characteristic strain of the nanohertz SGWB, along with the corresponding discrete values f_j within the underlying PTA frequency range and the uncertainties $\sigma_{h_{c,\text{exp}},j}$ in the characteristic strain. The frequencies f_j have no uncertainties as they are binned.

A neutral way to define the likelihood function when important information about how the data were obtained is missing, as it is the case in this work, is to assume that the uncertainties

are *Gaussian-distributed* and independent. In this case, $P(d|\Theta)$ can be expressed as

$$P(d|\Theta) = \prod_{j=1}^{n_{\text{data}}} \frac{1}{\sqrt{2\pi\sigma^2_{h_{c,\text{exp},j}}}} \exp\left[-\frac{1}{2}\frac{\left(h_{c,\text{exp},j} - h_{c,\text{model},j}(\Theta)\right)^2}{\sigma^2_{h_{c,\text{exp},j}}}\right] , \tag{3.4}$$

where $h_{c,\text{model},j}(\Theta)$ are the corresponding values for the characteristic strain predicted by the theoretical model depending on the fit parameters. They are obtained from Eq. 2.48 as described in the previous subsection. Furthermore, n_{data} is the number of considered/available experimental data points. In this study, the first five bins of the 15-year data set from NANOGrav and the lowest ten bins of the 18-year data set from PPTA are used[45]. Accordingly, $n_{\text{data}} = 15$. Additionally, since symmetric errors in the characteristic strain of the experimental data are required for the calculation of the posterior distribution according to Eq. 3.6, the mean values from the negative and positive uncertainties shown in Fig. 1.2 are used.

The second important component for calculating the posterior is the prior distribution $P(\Theta)$, which covers any prior knowledge about the model parameters. This includes physical constraints on the parameter ranges or limitations known from previously conducted experiments. By default, a *uniform prior* for Θ_k is chosen, defined by

$$P(\Theta_k) = \begin{cases} \frac{1}{(\Theta_{k,\text{max}} - \Theta_{k,\text{min}})} & \text{if } \Theta_k \in [\Theta_{k,\text{min}}, \Theta_{k,\text{max}}] \\ 0 & \text{otherwise} \end{cases} . \tag{3.5}$$

Here, $\Theta_{k,\text{min}}$ represents the lower bound and $\Theta_{k,\text{max}}$ the upper bound for the fit parameter Θ_k, which are fixed before starting the MCMC algorithm. The term "uniform" means that, during the MCMC sampling, each value for Θ_k is drawn from the interval $[\Theta_{k,\text{min}}, \Theta_{k,\text{max}}]$ with the constant probability $P(\Theta_k)$. Mathematically, this is expressed as $\Theta_k \in \mathcal{U}(\Theta_{k,\text{min}}, \Theta_{k,\text{max}})$.

It should also be noted that factors independent of Θ are irrelevant for the MCMC process, as only the *ratio* of the posterior distribution for two different samples is required to determine the acceptance probability according to Eq. 3.1. Therefore, such constant terms are omitted when implementing the aforementioned statistical functions into the `SMBHBpy` code. These constants include the evidence $P(d)$ from Eq. 3.3, the factor $\prod_{j=1}^{n_{\text{data}}} \left(2\pi\sigma^2_{h_{c,\text{exp},j}}\right)^{-1/2}$ of $P(d|\Theta)$ in Eq. 3.4, and the denominator $(\Theta_{k,\text{max}} - \Theta_{k,\text{min}})$ of $P(\Theta_k)$ for each k (Eq. 3.5). The resulting logarithmic

[45] As mentioned at the beginning of this thesis, the interesting feature in the observed SGWB spectrum, namely the turnover in the arrangement of the data points, is located at the low-frequency end of the PTA band (see Fig. 1.2). Therefore, considering higher frequency bins is not necessary for the purpose of this work.

expression for the posterior, used in the `SMBHBpy` code, is therefore given by

$$\log_{10}(P(\Theta|d))\Big|_{\text{w/o const}} = -\frac{1}{2}\chi^2 = \begin{cases} -\frac{1}{2}\sum_{j=1}^{n_{\text{data}}}\left(\frac{h_{c,\text{exp},j}-h_{c,\text{model},j}(\Theta)}{\sigma_{h_{c,\text{exp},j}}}\right)^2 & \text{if } \Theta \in \mathcal{C}_\Theta \\ -\infty & \text{otherwise} \end{cases}, \tag{3.6}$$

where $\mathcal{C}_\Theta$ denotes the Cartesian product $\mathcal{C}_\Theta = \prod_{k=1}^{n_{\text{dim}}}[\Theta_{k,\text{min}}, \Theta_{k,\text{max}}]$, which corresponds to the set of the physically constrained/considered fit parameter combinations. The abbreviation "w/o const" means that the above mentioned constant terms are not taken into account. Additionally, the quantity χ^2 is used in Subsec. 4.2 to quantify how well the theoretical model for calculating the SGWB fits the experimental data for certain parameter combinations. The smaller the value for χ^2, the better the agreement between the model and the data.

This work uses the Python package `emcee` [116] for the MCMC sampling. By employing an affine-invariant ensemble sampler [117], multiple Markov Chains can be constructed in parallel. This approach makes `emcee` very efficient for performing random walks through high-dimensional parameter spaces and eliminates the need for manual tuning of the proposal function Q. In addition, the algorithm behind `emcee` has several advantages over a traditional Metropolis-Hastings method, allowing a more reliable approximation of the true posterior distribution (for more details, see Ref. [116]). Nevertheless, `emcee` is based on its fundamental principles. The different Markov Chains are referred to as *walkers*. Using a large number of walkers can speed up the exploration of the parameter space and help to reach different regions of it, especially when there is a high degeneracy between the model parameters[46]. In this study, 30 walkers with $n_{\text{steps}} = 3{,}000$ steps each are used. Additionally, `emcee` can be easily combined with the Python module `multiprocessing` for parallel processing [118]. Using several processor cores[47], the sampling speed can be significantly increased.

By taking a look at the parameter values for each walker at each step, the convergence behavior of the Markov Chains can be visually assessed. After the true posterior has been approximated, the *binned* one- and two-dimensional posterior distributions can be easily extracted from it. Specifically, the one-dimensional posterior for the fit parameter Θ_k is obtained by counting the number of samples falling within each bin[48], ignoring the specific values of the other parameters. A two-dimensional posterior for parameter combinations of Θ_k and $\Theta_{k'}$, with $k \neq k'$, is defined

[46] For this purpose, the number of walkers used should be at least 2 to $3 \times n_{\text{dim}}$ [116].
[47] The computer on which the different MCMCs run has a total of 4 CPU-cores.
[48] In this work, 30 bins are used to create the corner plots.

in an analogous manner. Both types of posterior distribution are typically visualized in the form of *corner plots* [119]. The diagrams on the diagonals of such plots correspond to marginalized distributions (one-dimensional posteriors) for each model parameter independently. The higher a bar, the more frequently values within the associated bin were tested during the sampling process. Moreover, for quantifying the uncertainties of the median values of the fit parameters in the titles of the diagonal plots, the 16th and 84th percentiles are utilized. The off-diagonal plots represent the pairwise distributions (two-dimensional posteriors) of different parameters, highlighting the physical correlations between the individual model parameters. Additionally, blurry squares indicate areas where many parameter combinations are located. This means that these combinations are particularly favored by the underlying experimental data. Furthermore, three different contours represent the 68 %, 95 %, and 99 % confidence level. These lines specify the probability that the parameters fall within the corresponding enclosed region.

Finally, this subsection provides a more detailed discussion of the model parameters considered in this work, including the choice of their priors. As discussed in Subsec. 2.6, these encompass the initial eccentricity e_0 of the identical SMBHBs, the logarithmic ratio $\log_{10}(\rho/\sigma)$ characterizing the environmental conditions in their host galaxies, and A_0 as the quantity directly related to the level of the stochastic background. That means Θ is given by $\Theta = \{e_0, \log_{10}(\rho/\sigma), A_0\}$ and $n_{\mathrm{dim}} = 3$.

The initial eccentricity e_0 is physically constrained to $0 \leq e_0 < 1$, and A_0 has to be positive, i.e., $A_0 > 0$. However, for the sampling process, the upper limit of e_0 is set to values ≤ 0.99 depending on the considered initial semi-major axis a_0 (for more details, see Tab. 4.3). This ensures that the computing time remains moderate for a variety of parameter combinations, even for those with high ρ/σ. Otherwise, the number of GW harmonics that need to be considered would quickly become too large for certain combinations (see Eq. 2.47 and Fig. 2.3), since the gravitational slingshot mechanism leads to an eccentrification of the orbits (see Subsec. 2.2). Besides, eccentricities of $e_0 \gtrsim 0.9$ at the formation of a SMBHB are expected to be untypical/unphysical [110].

At last, $\log_{10}(\rho/\sigma)$ is limited to $-10 < \log_{10}(\rho/\sigma\,[\mathrm{M_\odot/pc^3\,(km/s)^{-1}}]) < 10$ for the sampling process. This is a sufficient and conservative choice for the range of this fit parameter as can be seen from the results in Subsec. 4.2. The cases where the SMBHBs evolve in vacuum ($\rho/\sigma = 0$) or have circular orbits ($e_0 = e(t_r) = 0$) are analyzed separately using the MCMC algorithm with the remaining two model parameters.

4 Results

This chapter first discusses the orbital evolution of SMBHBs losing energy due to gravitational 3-body scatterings with surrounding stars as well as through the radiation of GWs. Next, it is shown how both different eccentricities and the stellar environment influence the shape of the SGWB produced by a population of *identical* SMBHBs. The corresponding results will motivate the second subsection, where the findings from the MCMC sampling algorithm are presented for various initial semi-major axes a_0. Based on these outcomes, the parameter space consisting of $e_0, \rho/\sigma$, and A_0 is constrained, the degeneracy between the eccentricity and the gravitational slingshot mechanism is partially broken and best fits for the theoretical SGWB model to the considered experimental data from NANOGrav and PPTA are generated.
To avoid the explicit use of units in several places, the following reference values will be used from this chapter onward: $\rho_{\text{ref}} = 1\,\text{M}_\odot/\text{pc}^3$, $\sigma_{\text{ref}} = 1\,\text{km/s}$, and $A_{0,\text{ref}} = 1\,\text{Mpc}^{-3}$.

4.1 SMBHBs: Orbital Evolution and Environmental Influences on their SGWB

At the beginning of this subsection, it should be pointed out again that the SMBHBs are described within the Newtonian approximation. This requires the termination of the numerical solution of the differential equations for a and e at $a = a_{\text{fin}} = r_{\text{ISCOs}}$ (see Subsec. 2.1). Furthermore, a_0 is defined at the time of SMBHB formation and equated with r_{infl}.
The figures in this subsection are created using the values listed in Tab. 4.1 for the mass m_1 of the first SMBH, the mass ratio q, the redshift z, the hardening rate H (see discussions in Subsecs. 2.2 and 2.6), and the number density normalization A_0.

Parameter	Value
m_1	$3 \times 10^9\,\text{M}_\odot$
q	0.65
z	0.3
H	18
$A_0/A_{0,\text{ref}}$	10^{-4}

Tab. 4.1: Table with the values for different SMBHB and SGWB parameters used for Figs. 4.1 to 4.5.

As shown in Subsecs. 2.2 and 2.3, the interaction of a SMBHB with its stellar environment leads to an eccentrification of the orbits, while the GW emission tends to circularize them. This interplay can be visualized by plotting the eccentricity e as a function of the semi-major axis a as done in Fig. 4.1 for an individual SMBHB exhibiting an intermediate initial eccentricity of $e_0 = 0.5$ (left panel) and a high initial eccentricity of $e_0 = 0.9$ (right panel), respectively. In both cases $\frac{\rho/\sigma}{\rho_{\mathrm{ref}}/\sigma_{\mathrm{ref}}} = 10^0, 10^4$ (blue, orange) as well as $a_0 = 40, 100\,\mathrm{pc}$ (solid, dashed lines) are considered. For comparison, the orbital evolution is also plotted for the case where the binary system is surrounded by vacuum and thus only loses energy through the radiation of GWs (GW-only case, green lines).

As discussed in Subsec. 2.4, the value of a up to which the gravitational slingshot mechanism drives the evolution of a SMBHB decreases as ρ/σ increases (see Eq. 2.30). This implies that the maximum eccentricity e_{max} achieved also increases with ρ/σ, as the eccentrification effect persists over a longer period. However, such an extension of the 3B-dominated phase can also be realized by increasing a_0 while keeping $\frac{\rho/\sigma}{\rho_{\mathrm{ref}}/\sigma_{\mathrm{ref}}}$ fixed. Each of these three characteristics is evident from Fig. 4.1. Additionally, it can be observed that stellar hardening causes a significant (non-negligible) change in the eccentricity, especially for moderate values of e_0 such as $e_0 = 0.5$ and high ratios between ρ and σ. The former is due to the parametrization of the eccentricity growth rate K used in this work (see Eq. 2.5) and has also been confirmed by Ref. [92].

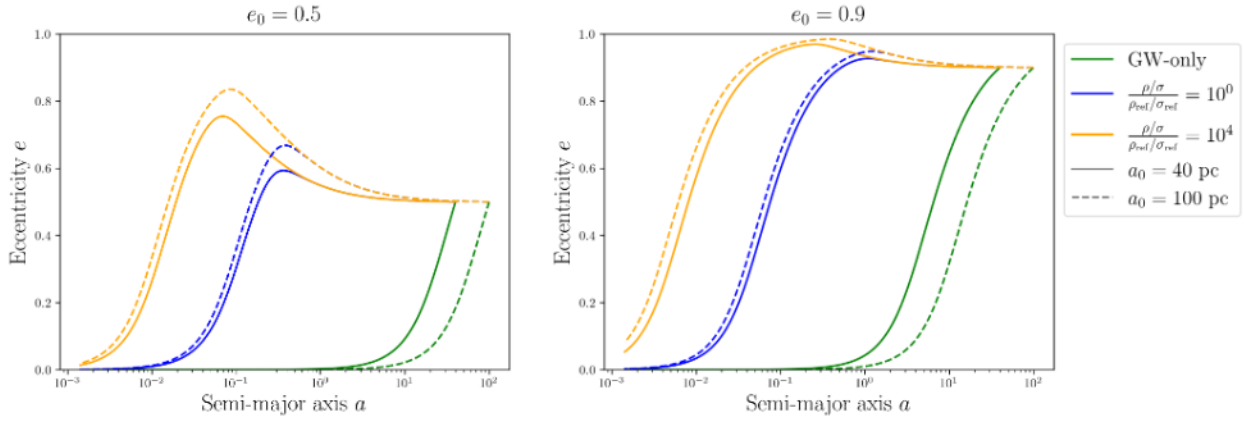

Fig. 4.1: Orbital evolution of SMBHBs: Eccentricity e depending on the semi-major axis a for $\frac{\rho/\sigma}{\rho_{\mathrm{ref}}/\sigma_{\mathrm{ref}}} = 10^0, 10^4$ (blue, orange) and $a_0 = 40, 100\,\mathrm{pc}$ (solid, dashed lines). For comparison, the GW-only case is depicted in green. *Left panel:* For $e_0 = 0.5$. *Right panel:* For $e_0 = 0.9$.

The remainder of this subsection focuses on the precise impact of varying e_0 and a_0 as well as the interaction of SMBHBs with their stellar environment on the shape of their SGWB.

However, before going into these details, a discussion of why this shape looks the way it does and how the stochastic background is generally composed for both circular and eccentric orbits is provided considering four exemplary cases (see Fig. 4.2).

For circular binary systems, explicit relations between the characteristic strain $h_{c,\mathrm{SGWB}}$ of the SGWB and the observed GW frequency f can be derived analytically. By combining Eqs. 2.11, 2.19, 2.24, 2.39, and 2.48, one finds that within the frequency range where GW emission dominates the evolution of the SMBHBs, i.e., where $\dot{f}_{\mathrm{orb}}\big|_{\mathrm{GW}} \gg \dot{f}_{\mathrm{orb}}\big|_{\mathrm{3B}}$, it follows that $h_{c,\mathrm{SGWB}}(f) \propto f^{-2/3}$. In contrast, during the 3B-driven phase, where $\dot{f}_{\mathrm{orb}}\big|_{\mathrm{GW}} \ll \dot{f}_{\mathrm{orb}}\big|_{\mathrm{3B}}$, $h_{c,\mathrm{SGWB}}(f) \propto f$ applies. This implies that the slope of $h_{c,\mathrm{SGWB}}$ changes its sign[49] at a specific frequency, the *turnover* frequency f_t, causing the 3B-dominated part of the SGWB spectrum to lie below the spectrum for the GW-only case (see blue line in Fig. 4.2). This *attenuation* can be explained by the fact that the presence of (stellar) matter in a SMBHB, according to Eq. 2.10, increases the total energy loss of the binary system, meaning it evolves faster and thus spends less time emitting GWs at each frequency. When eccentricity comes into play, however, the situation quickly becomes more complex.

Firstly, the GW emission is enhanced for eccentric orbits compared to circular orbits (see Eq. 2.19), which accelerates the SMBHB evolution and, as explained above, diminishes $h_{c,\mathrm{SGWB}}$. Secondly, eccentricity distributes the radiation of energy preferentially toward higher harmonics [120]. Both effects cause not only a turnover in the SGWB spectrum but also a *bump*, i.e., an amplification of $h_{c,\mathrm{SGWB}}$ compared to the circular case within a small frequency range. Furthermore, the turnover is shifted to a higher frequency with increasing eccentricity. An additional energy loss due to the gravitational slingshot mechanism further reduces $h_{c,\mathrm{SGWB}}$ across a broader frequency range. All the above mentioned features can be seen in Fig. 4.2.

As described at the beginning of Subsec. 2.3, in the case of circular orbits, only the second harmonic contributes to the GW signal of SMBHBs, while for eccentric binary systems, all harmonics must be taken into account. Fig. 4.2 also shows the contribution of the first three terms (dashed, dashed-dotted, and dotted lines) to the characteristic strain of the total SGWB (solid lines) produced by identical SMBHBs with $e_0 = 0.9$, according to Eq. 2.48. It can be observed that the stochastic background is dominated by the $n = 1$ mode for frequencies to the left of the turnover and by the $n = 2$ mode for frequencies to the right of it. In contrast, all considered terms play an important role in shaping the transition between these two regions.

[49] Provided that $h_{c,\mathrm{SGWB}}(f)$ is plotted against f on a double-logarithmic scale, as usually done.

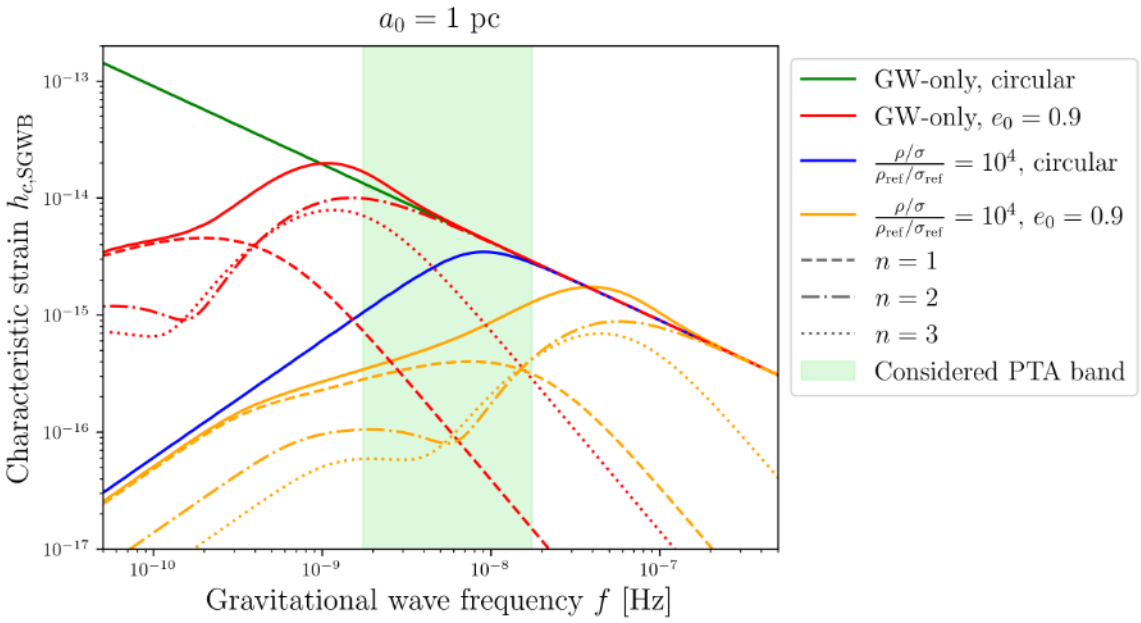

Fig. 4.2: SGWB (solid lines) from SMBHBs with circular/eccentric orbits surrounded by vacuum (green/red) and evolving in a stellar background with the parameter $\frac{\rho/\sigma}{\rho_{\mathrm{ref}}/\sigma_{\mathrm{ref}}} = 10^4$ (blue/orange), respectively. For the cases with $e = 0.9$, the first three contributions $n = 1, 2, 3$ (dashed, dashed-dotted, and dotted lines) to the total SGWB are also depicted. Additionally, the PTA band considered in this work is highlighted in light green. For the initial semi-major axis, $a_0 = 1\,\mathrm{pc}$ is selected.

In Fig. 4.3, the SGWB for the GW-only case with $e_0 = 0.99$ is shown for four different initial semi-major axes. The specific choices of $a_0 = 1, 7, 40\,\mathrm{pc}$, and $100\,\mathrm{pc}$ will be justified in Subsec. 4.2. It is clearly evident that the frequency at which the turnover occurs decreases with increasing a_0. This was first demonstrated by Ref. [34]. However, for circular orbits, the turnover would remain at the same frequency, as $f_t\big|_{e=0}$ depends neither explicitly nor implicitly on a_0 but only on ρ/σ (see Eq. 2.49).

As will become more plausible in the next subsection, the turnover of the SGWB spectrum must lie near the low-frequency end of the PTA band in order to provide good fits to the NANOGrav and PPTA data (see also Fig. 1.2). Since a decrease in e_0 causes a shift of the turnover to lower frequencies, it becomes impossible for $a_0 \gtrsim 7\,\mathrm{pc}$ that the turnover appears within the PTA band under consideration in the GW-only case (for $e_0 \leq 0.99$, see Fig. 4.3). Thus, it can already be concluded at this point that theoretical SGWB models with $a_0 \gtrsim 7\,\mathrm{pc}$ and $e_0 \leq 0.99$, which assume that SMBHBs evolve in vacuum, will not produce good fits to the experimental data. For these scenarios, the corresponding SGWB for frequencies within the PTA range is similar to that for the GW-only case with circular orbits ($h_{c,\mathrm{SGWB}}(f) \propto f^{-2/3}$) and could additionally

exhibit a small part of a bump depending on a_0 as can be seen in Fig. 4.3. Consequently, it can also be predicted for these models that the quality of the fits, i.e., χ^2, will hardly depend on $e_0 \leq 0.99$. On the other hand, (extremely) high initial eccentricities will be required for $1\,\mathrm{pc} \lesssim a_0 \lesssim 7\,\mathrm{pc}$ to minimize χ^2. However, when environmental effects are included, e_0 can be significantly lowered as will be discussed next.

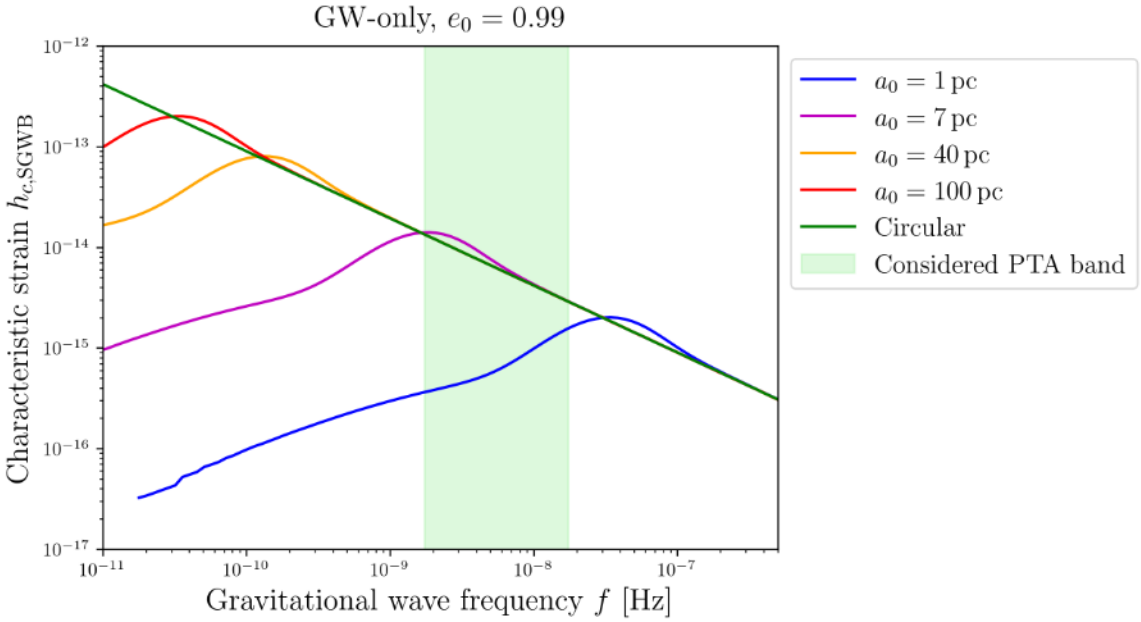

Fig. 4.3: SGWB for $a_0 = 1, 7, 40\,\mathrm{pc}$, and $100\,\mathrm{pc}$ (blue, violet, orange, and red) considering the GW-only case with $e_0 = 0.99$. The case in which the SMBHBs have circular orbits is depicted in green.
Note: For $a_0 = 1\,\mathrm{pc}$, the frequency at which GWs are emitted by the SMBHBs for the first time is higher than the minimum frequency taken into account in this plot.

In Fig. 4.4, the same as in Fig. 4.3 is illustrated, except that the gravitational slingshot effect with $\frac{\rho/\sigma}{\rho_{\mathrm{ref}}/\sigma_{\mathrm{ref}}} = 10^2$ is additionally taken into account and a smaller initial eccentricity of $e_0 = 0.5$ is considered. In comparison to the GW-only case, the turnover lies within the PTA band even for large a_0 and smaller e_0. Furthermore, the variances between the results for different a_0 are much less pronounced than in Fig. 4.3. Moreover, it can be observed that f_t does not decrease with increasing a_0 when the interaction with the stellar environment is included, but instead increases. Based on the previous results, it can be stated that the shape of the SGWB strongly depends on the specific combination of a_0, e_0, and ρ/σ. This will be further demonstrated in another example, where the value for $\frac{\rho/\sigma}{\rho_{\mathrm{ref}}/\sigma_{\mathrm{ref}}}$ is varied over several orders of magnitude.
Fig. 4.5 shows $h_{c,\mathrm{SGWB}}$ for $\frac{\rho/\sigma}{\rho_{\mathrm{ref}}/\sigma_{\mathrm{ref}}} = 0, 10^0, 10^2$, and 10^4, considering a fixed initial semi-major axis of $a_0 = 7\,\mathrm{pc}$ and two different values for the initial eccentricity $e_0 = 0, 0.9$ (solid, dahed

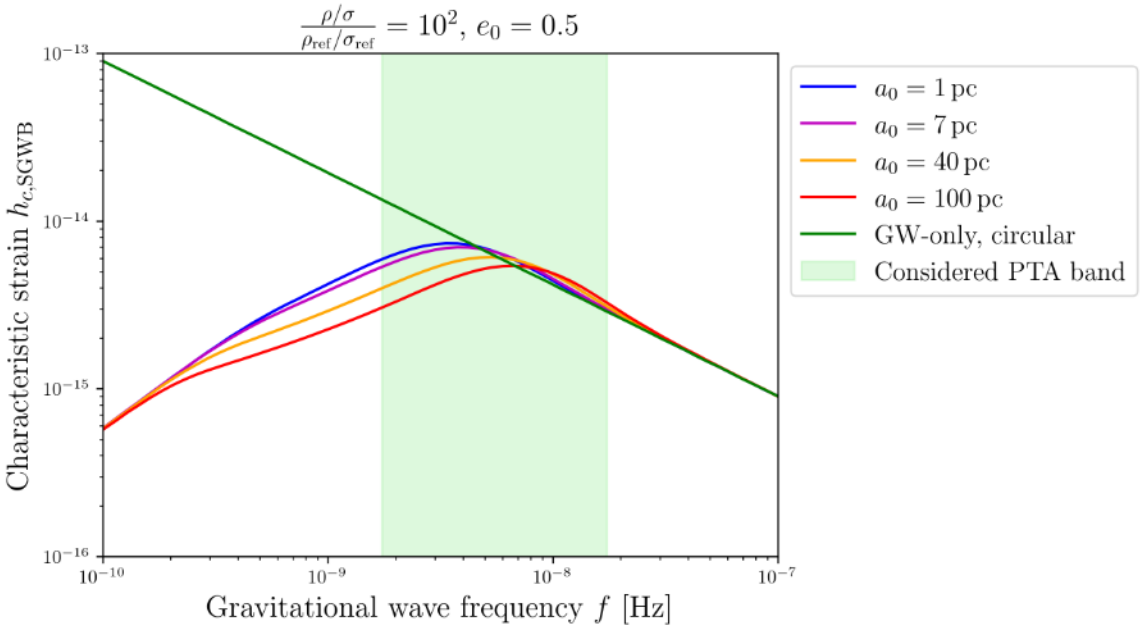

Fig. 4.4: Spectrum for the SGWB of SMBHBs with $e_0 = 0.5$ evolving in a dense stellar environment with $\frac{\rho/\sigma}{\rho_{\mathrm{ref}}/\sigma_{\mathrm{ref}}} = 10^2$. Similar to Fig. 4.3, the characteristic strain is presented for $a_0 = 1, 7, 40\,\mathrm{pc}$, and $100\,\mathrm{pc}$ (blue, violet, orange, and red). For comparison, the vacuum case with circular orbits is plotted in green.

lines). According to Eq. 2.10, the larger ρ/σ is, the greater the energy loss of the SMBHBs due to the ejection of stars, and consequently, the more distinct the attenuation of the SGWB

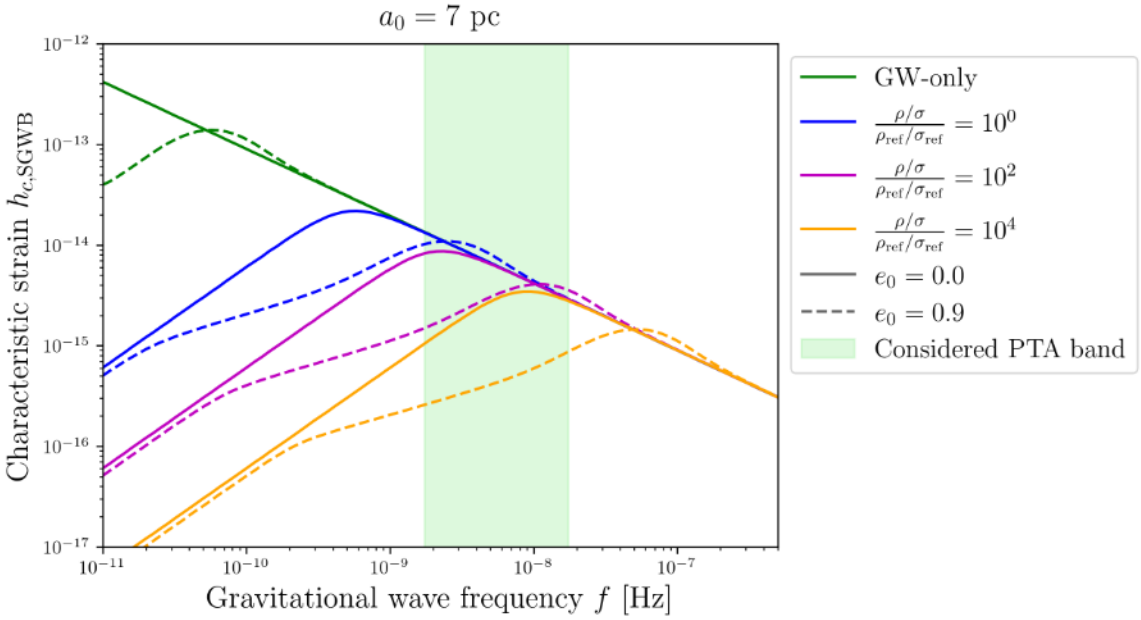

Fig. 4.5: Characteristic strain of the SGWB produced by SMBHBs with $a_0 = 7\,\mathrm{pc}$ for various $\frac{\rho/\sigma}{\rho_{\mathrm{ref}}/\sigma_{\mathrm{ref}}} = 0, 10^0, 10^2$, and 10^4 (green, blue, violet, and orange) and two different $e_0 = 0, 0.9$ (solid, dashed lines).

becomes. As a result, f_t increases with increasing ρ/σ for both eccentric and circular orbits. Finally, the general impacts observed in this subsection on the turnover frequency f_t due to changes in a_0, e_0, or ρ/σ are summarized in the following table:

a_0	e_0	ρ/σ	f_t
increases	fixed, $= 0$	fixed, ≥ 0	constant
increases	fixed, > 0	fixed, $= 0$	decreases
increases	fixed, > 0	fixed, > 0	increases
fixed	increases	fixed, ≥ 0	increases
fixed	fixed, ≥ 0	increases	increases

Tab. 4.2: Effects of different variations of a_0, e_0, or ρ/σ on f_t.

4.2 MCMC Results: Degeneracy between Eccentricity and Stellar Environment

Before presenting the MCMC results and the corresponding best fits to the NANOGrav and PPTA data for different a_0, it remains to explain why $a_0 = 1, 7, 40\,\mathrm{pc}$, and $100\,\mathrm{pc}$ are chosen as values for the initial semi-major axis as well as to outline important assumptions incorporated into the MCMC algorithm.

In our joint publication with the NANOGrav collaboration [1], we consider the stellar density at parsec-scale $\rho_{1\mathrm{pc}} = \rho(r = 1\,\mathrm{pc})$ as a model parameter instead of the ratio between ρ and σ at the influence radius $r_{\mathrm{infl}} = a_0$. To compare the results from both works, $a_0 = 1\,\mathrm{pc}$ is selected. The value $a_0 = 7\,\mathrm{pc}$ represents the threshold in the GW-only case, beyond which the turnover of the SGWB spectrum lies outside the PTA band (for $e_0 \leq 0.99$, see Fig. 4.3). However, both $1\,\mathrm{pc}$ and $7\,\mathrm{pc}$ are not expected as typical values for a_0 of SMBHBs in accordance with galactic-scale N-body simulations [110]. Rather, values like $40\,\mathrm{pc}$ or $100\,\mathrm{pc}$ seem more realistic in this regard. The corresponding priors used for e_0 are given in Tab. 4.3. Since the calculation of the SGWB for $e_0 > 0.9$ considering $40\,\mathrm{pc}$ or $100\,\mathrm{pc}$ in conjunction with large ρ/σ would take too long, e_0 is limited to 0.9 for these two cases (see related explanation in Subsec. 3.2). Nevertheless, for $1\,\mathrm{pc}$ and $7\,\mathrm{pc}$, combinations with $e_0 > 0.9$ should also be taken into account (see discussion regarding Fig. 4.3). For this reason, and to allow comparisons of MCMC results for different a_0, two runs with different priors are performed for each of these two a_0.

a_0	1 pc	7 pc	40 pc	100 pc
Uniform distributions for e_0	$\mathcal{U}(0, 0.9)$ & $\mathcal{U}(0, 0.99)$	$\mathcal{U}(0, 0.9)$ & $\mathcal{U}(0, 0.99)$	$\mathcal{U}(0, 0.9)$	$\mathcal{U}(0, 0.9)$

Tab. 4.3: Table with the uniform distributions (priors) for e_0 for all considered a_0.

As mentioned earlier, eccentric SMBHBs emit GWs at several harmonics, causing a binary system to contribute to more than one frequency bin, and thus making different frequency bins correlated [45]. This feature cannot be mimicked by environmental effects. However, this type of correlation is neglected in this thesis, due to the fact that it is at a low level even for large eccentricities, as demonstrated by Ref. [35]. In addition, the data from NANOGrav and PPTA

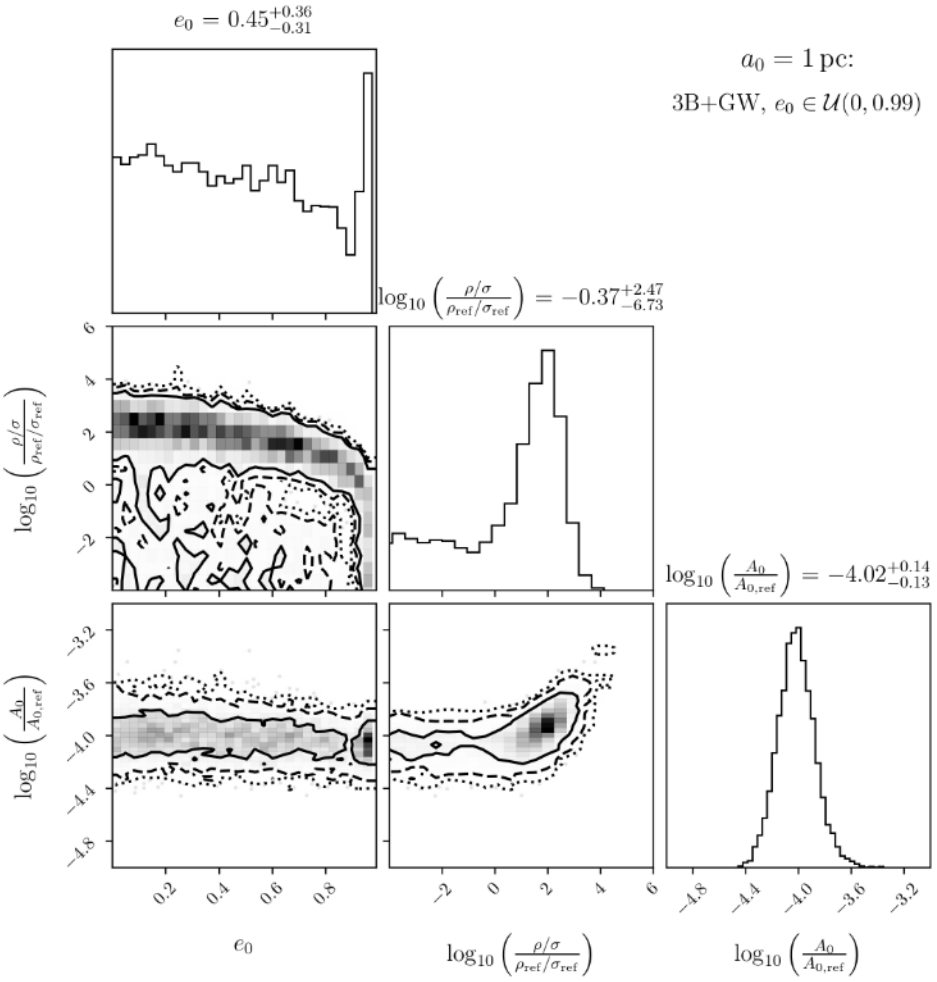

Fig. 4.6: $a_0 = 1\,\mathrm{pc}$: Approximated one- and two-dimensional posterior distributions for the model parameters $e_0, \log_{10}(\rho/\sigma)$ and A_0. The solid, dashed and dotted contours enclose the 68 %, 95 % and 99 % confidence regions, respectively. The corresponding corner plot for $e_0 \in \mathcal{U}(0, 0.9)$ can be found in Appendix C (see Fig. C.14).

are assumed to be independent of each other.

As discussed in the previous subsection, eccentric orbits as well as the interaction with surrounding stars lead to a turnover in the SGWB spectrum produced by SMBHBs. Looking at the current data from NANOGrav and PPTA in Fig. 1.2, such a turnover can be clearly seen at around 3 to 4 nHz. This is an indication that SMBHBs do not move on circular orbits through vacuum, but are instead located in dense stellar environments and could also have certain eccentricities. Indeed, the outcomes of the MCMC runs, presented in Figs. 4.6 to 4.9, show a pronounced degeneracy between the two model parameters e_0 and $\log_{10}(\rho/\sigma)$ for all considered a_0; very eccentric SMBHBs in stellar environments with lower ρ/σ produce a turnover at approximately the same position f_t favored by the data as more circular binary systems in

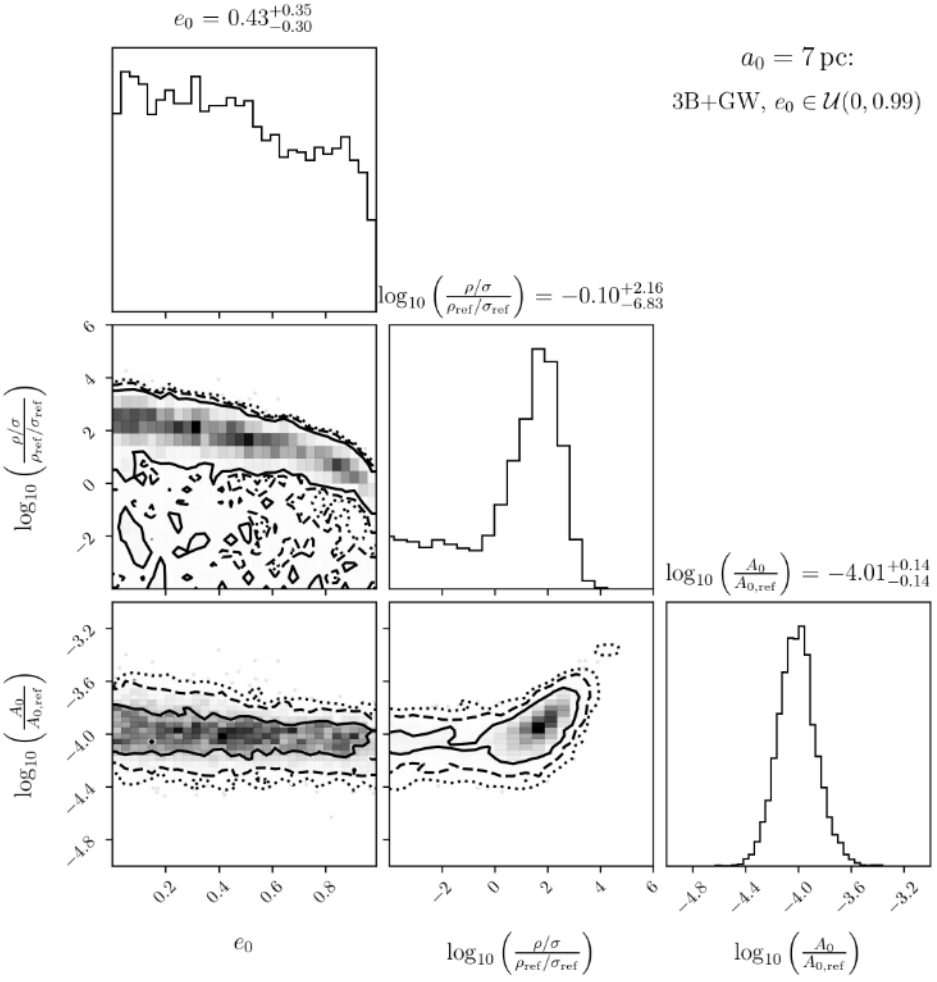

Fig. 4.7: $a_0 = 7\,\mathrm{pc}$: Approximated one- and two-dimensional posterior distributions for the model parameters $e_0, \log_{10}(\rho/\sigma)$ and A_0. The solid, dashed and dotted contours enclose the 68 %, 95 % and 99 % confidence regions, respectively. The corresponding corner plot for $e_0 \in \mathcal{U}(0, 0.9)$ can be found in Appendix C (see Fig. C.15).

stellar environments exhibiting higher ρ/σ. Consequently, countless combinations of e_0 and ρ/σ provide similarly good fits to the experimental data. Nevertheless, a strict upper limit for the data-preferred value of $\log_{10}(\rho/\sigma)$ depending on the initial eccentricity is revealed for the first time in this study, as will be discussed in more detail later.

Next, the similarities and differences between the four cases are highlighted, with a particular focus on the physical correlations between the three model parameters (see also Subsec. 4.1). Afterward, the results for $a_0 = 1\,\mathrm{pc}$ are compared with those from Ref. [1].

The first notable observation, aside from the previously mentioned degeneracy, is that the favored values of A_0 decrease as ρ/σ decreases until $\frac{\rho/\sigma}{\rho_{\mathrm{ref}}/\sigma_{\mathrm{ref}}}$ reaches $\approx 10^0$. This behavior can be explained by the fact that higher ρ/σ lead to a stronger attenuation of the SGWB, and, consequently, smaller values of A_0 are required to maintain the data-preferred level of the stochastic

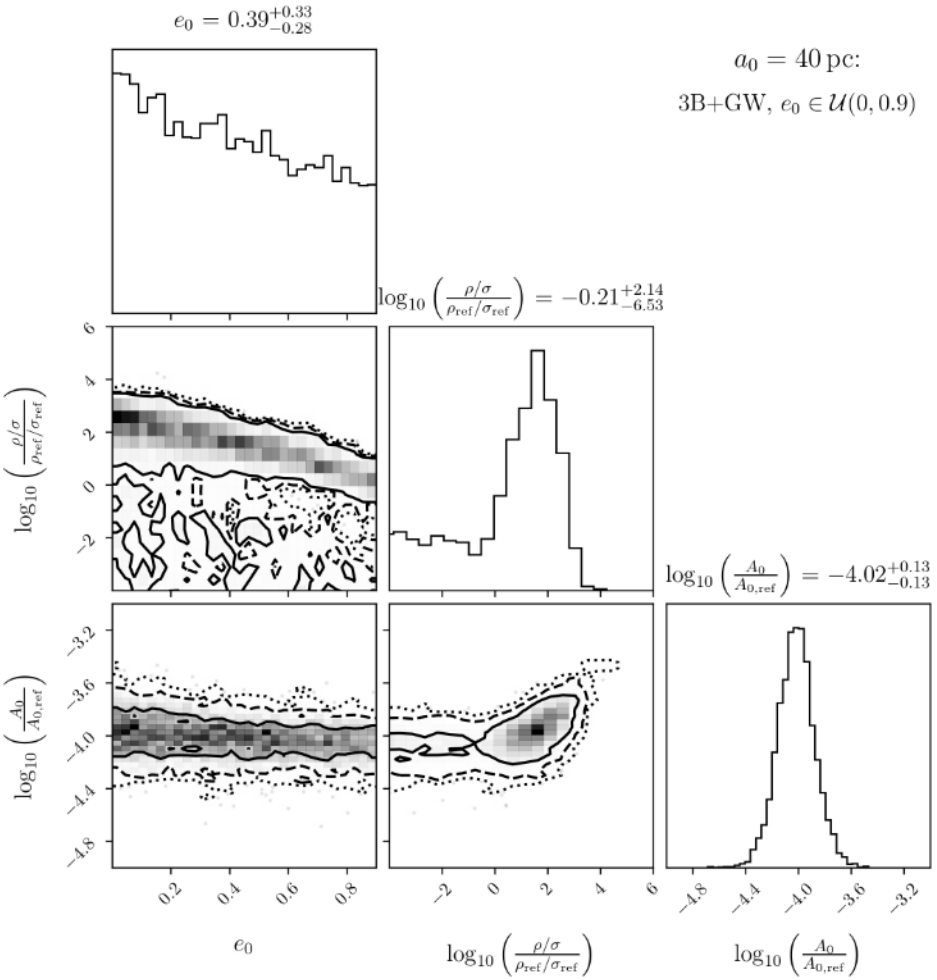

Fig. 4.8: $a_0 = 40\,\mathrm{pc}$: Approximated one- and two-dimensional posterior distributions for the model parameters $e_0, \log_{10}(\rho/\sigma)$ and A_0. The solid, dashed and dotted contours enclose the 68 %, 95 % and 99 % confidence regions, respectively.

background. However, in the case where $\frac{\rho/\sigma}{\rho_{\mathrm{ref}}/\sigma_{\mathrm{ref}}}$ is smaller than $\approx 10^0$, the region exhibiting significant diminution of $h_{c,\mathrm{SGWB}}$ lies at lower GW frequencies outside the range accessible to NANOGrav and PPTA for all considered a_0 (see Fig. 4.5 in conjunction with Fig. 4.4). Thus, it is no longer necessary to counterbalance by reducing A_0, resulting in A_0 remaining more or less constant. Nevertheless, a clear value for the number density normalization can be identified, which is most preferred by the data across a wide region of the parameter space in every examined case, namely $A_0/A_{0,\mathrm{ref}} \approx 10^{-4}$. This is due to the fact that the aforementioned variation in A_0 over ρ/σ is relatively small.

Furthermore, it can be seen that the value of ρ/σ providing a good agreement between the theoretical SGWB model and the data decreases with increasing initial eccentricity e_0 (see also Fig. 4.10). This is also consistent with what we found in Ref. [1] and is related to the fact

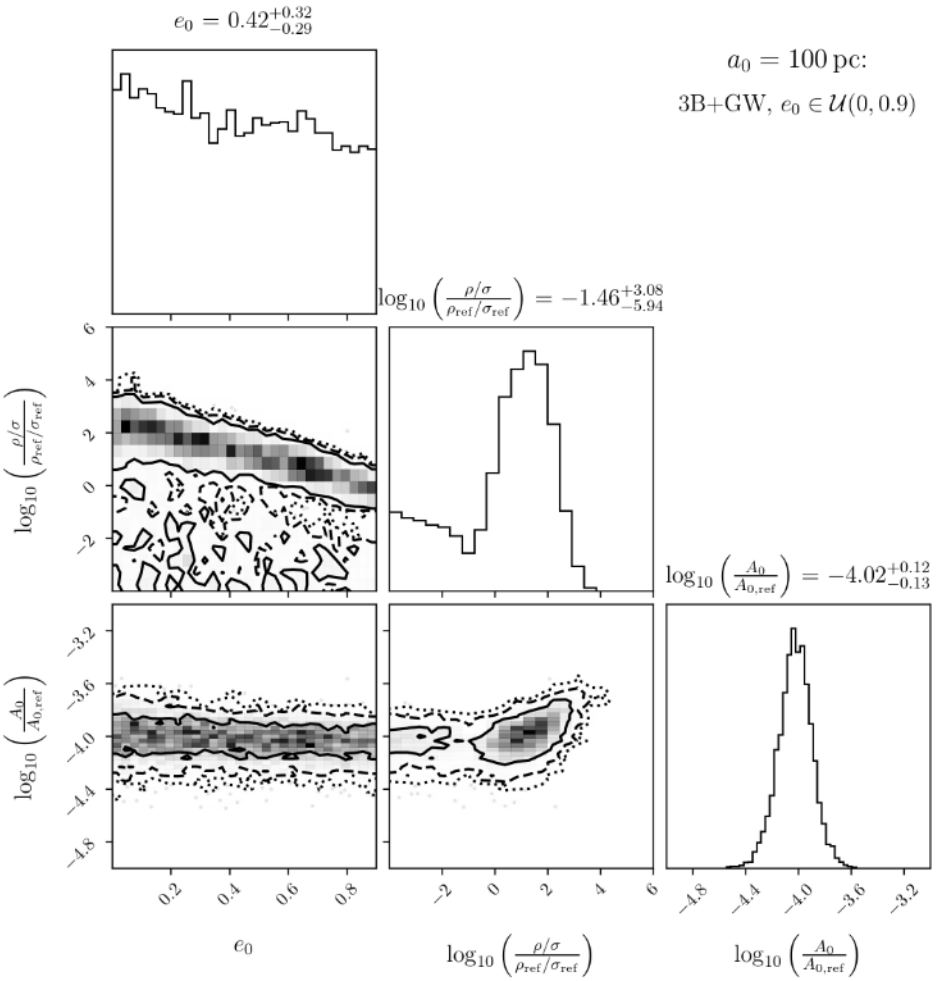

Fig. 4.9: $a_0 = 100\,\mathrm{pc}$: Approximated one- and two-dimensional posterior distributions for the model parameters $e_0, \log_{10}(\rho/\sigma)$ and A_0. The solid, dashed and dotted contours enclose the 68 %, 95 % and 99 % confidence regions, respectively.

that the experimental data demand the turnover to appear in a specific, narrow GW frequency range (see Fig. 1.2). A positive shift in the turnover of the SGWB spectrum induced by an increase in e_0 can be counteracted by choosing a smaller ρ/σ, and vice versa (see Tab. 4.2). Moreover, the comparison of the maximum value for $\log_{10}(\rho/\sigma)$ depending on e_0 at 99 % confidence level (CL) across all a_0 reveals that also an increase in a_0 leads to a reduction of the favored values for ρ/σ (see Fig. 4.10). However, this is not surprising for the same reason as before, in combination with the findings presented in Fig. 4.4. Of course, this behavior is also reflected in the best-fit values for ρ/σ (see Figs. 4.11 to 4.14), which are marked in Fig. 4.10 by colored crosses as well[50]. Consequently, for setting a stringent upper limit on ρ/σ, it is sufficient to focus on the case of $a_0 = 1\,\mathrm{pc}$.

Finally, since the position of the turnover in the case of circular orbits does not depend on the choice of a_0, both the different maxima of the 99 % CL and the best-fit values are approximately at the same level for $e_0 \approx 0$.

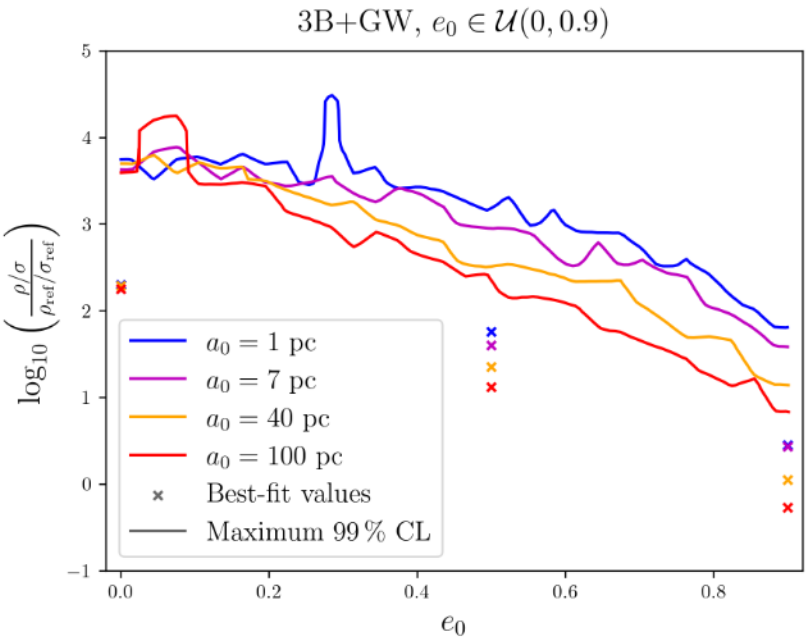

Fig. 4.10: Maximum of the 99 % CL for $\log_{10}\left(\frac{\rho/\sigma}{\rho_{\mathrm{ref}}/\sigma_{\mathrm{ref}}}\right)$ depending on e_0 for $a_0 = 1, 7, 40\,\mathrm{pc}$, and $100\,\mathrm{pc}$ (blue, violet, orange, and red), taken from Figs. C.14, C.15, 4.8, and 4.9, respectively. Additionally, the corresponding values from the best fits in Figs. 4.11 to 4.14 are also marked for $e_0 = 0, 0.5$, and 0.9 using colored crosses.

Thus, this work shows that the values of $\frac{\rho/\sigma}{\rho_{\mathrm{ref}}/\sigma_{\mathrm{ref}}}$ for $a_0 \geq 1\,\mathrm{pc}$, preferred by the latest NANOGrav and PPTA data at the 99 % CL, are below approximately 10^4 for circular orbits, below a

[50]Note: All best-fit values lie within the respective 68 % confidence region.

threshold between 10^3 and 10^4 for small to moderate e_0, and below around 10^2 for high initial eccentricities $e_0 \gtrsim 0.85$. For a given velocity dispersion σ, the corresponding upper limits for the stellar density at r_{infl} in the considered SMBHBs can also be determined.

Assuming that σ can be calculated via the virial theorem, i.e., $\sigma = \sqrt{GM/r_{\mathrm{infl}}}$, as we have done in Ref. [1], it follows that $\sigma \approx 5 \times 10^3\,\mathrm{km/s}$ for $r_{\mathrm{infl}} = 1\,\mathrm{pc}$ and $M = 4.95 \times 10^9\,\mathrm{M}_\odot$. Therefore, the value of ρ at which the marginalized distribution for $\log_{10}(\rho/\sigma)$ in Fig. 4.6 reaches its maximum is $\rho_{1\mathrm{pc}}^{\mathrm{max}} \approx 5 \times 10^5\,\mathrm{M}_\odot/\mathrm{pc}^3$. This value corresponds to the stellar density at 1 pc preferred by the experimental data across most of the parameter space and agrees very well with the corresponding value of $10^{5.8}\,\mathrm{M}_\odot/\mathrm{pc}^3 \approx 6 \times 10^5\,\mathrm{M}_\odot/\mathrm{pc}^3$ from our publication with NANOGrav. This underscores once again that the diverging theoretical SGWB models employed in the two studies are consistent with each other and therefore lead to the same overall findings.

The remaining MCMC results, including those considering only circular orbits or purely vacuum scenarios as well as selected plots showing the parameter distributions throughout the sampling process can be found in Appendix C. It can be observed that the posterior distributions of e_0 and $\log_{10}(\rho/\sigma)$ for the GW-only case exhibit the features expected from Fig. 4.3 for each a_0. In particular, a specific high initial eccentricity $e_0 \leq 0.99$ is preferred for $a_0 = 1\,\mathrm{pc}$

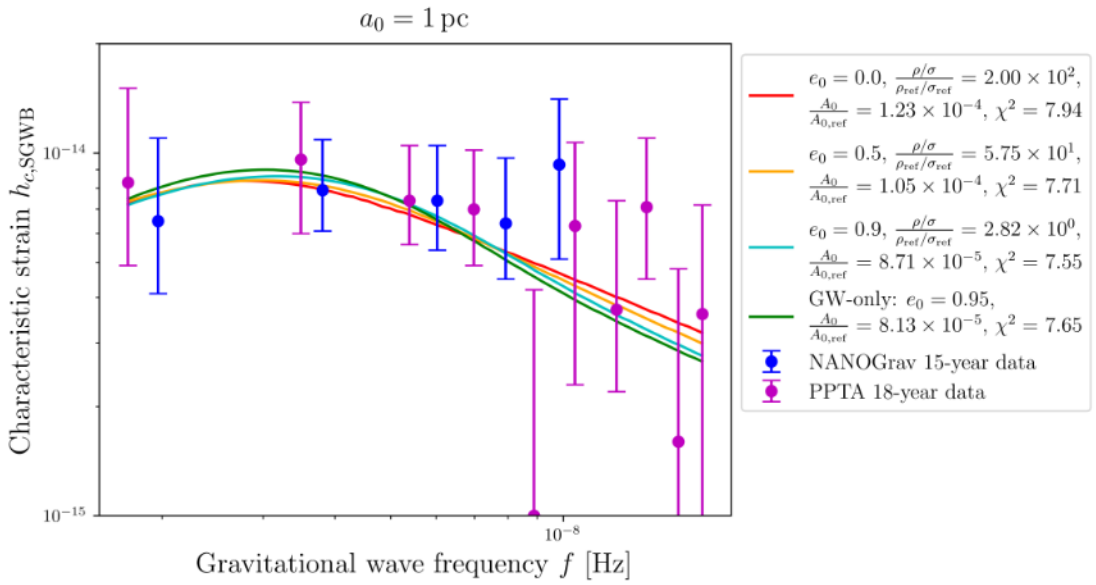

Fig. 4.11: $a_0 = 1\,\mathrm{pc}$: Best-fit SGWB spectrum for circular orbits ($e_0 = 0$, red), eccentric orbits with $e_0 = 0.5$ (orange) and 0.9 (cyan), respectively, as well as for the GW-only case (green), considering the lowest five frequency bins from the NANOGrav 15-year data set (blue) and the lowest ten frequency bins from the PPTA 18-year data set (violet). In addition to the best-fit values for $\frac{\rho/\sigma}{\rho_{\mathrm{ref}}/\sigma_{\mathrm{ref}}}$ and $A_0/A_{0,\mathrm{ref}}$, the corresponding values for χ^2 are also provided in the legend.

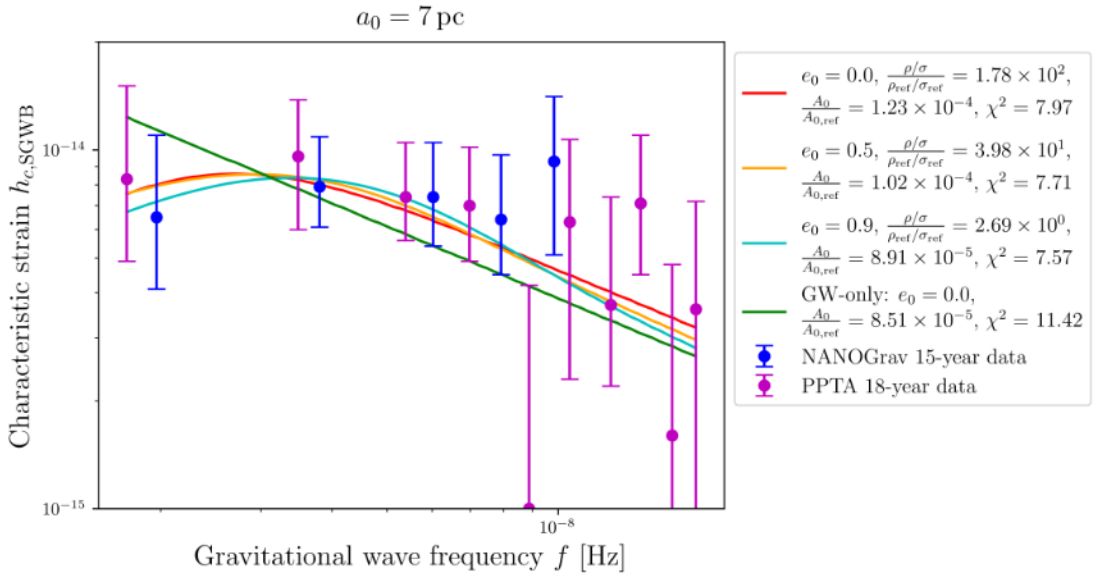

Fig. 4.12: $a_0 = 7\,\mathrm{pc}$: Best-fit SGWB spectrum for circular orbits ($e_0 = 0$, red), eccentric orbits with $e_0 = 0.5$ (orange) and 0.9 (cyan), respectively, as well as for the GW-only case (green), considering the lowest five frequency bins from the NANOGrav 15-year data set (blue) and the lowest ten frequency bins from the PPTA 18-year data set (violet). In addition to the best-fit values for $\frac{\rho/\sigma}{\rho_{\mathrm{ref}}/\sigma_{\mathrm{ref}}}$ and $A_0/A_{0,\mathrm{ref}}$, the corresponding values for χ^2 are also provided in the legend.

(see Figs. C.9 and 4.11), whereas for $a_0 \geq 7\,\mathrm{pc}$, this is no longer the case. Rather, each considered initial eccentricity is equally favored (see Figs. C.11, C.12 and C.13). For this reason, to create the best fits for the GW-only case in Figs. 4.12 to 4.14, $e_0 = 0$ is chosen arbitrarily for $a_0 = 7, 40\,\mathrm{pc}$, and $100\,\mathrm{pc}$. Some of the aforementioned characteristics are also visible in the corner plots presented in this subsection (see Figs. 4.6 and 4.7). Furthermore, as expected, the results for circular orbits are almost identical for all examined a_0 (see Figs. C.4 to C.7).

To conclude this subsection, the best fits of the theoretical SGWB model to the experimental data from NANOGrav and PPTA are presented for $a_0 = 1, 7, 40\,\mathrm{pc}$, and $100\,\mathrm{pc}$ (see Figs. 4.11 to 4.14). A comparison of the χ^2-values (see Eq. 3.6) shows that the SGWB generated by SMBHBs, which lose energy through both GW emission and the gravitational slingshot mechanism, aligns slightly better with the data for $a_0 = 7, 40\,\mathrm{pc}$, and $100\,\mathrm{pc}$ compared to the stochastic background for the GW-only case. This is because the latter does not exhibit a turnover at the low-frequency end of the considered PTA range. However, for $a_0 = 1\,\mathrm{pc}$, or more generally for $a_0 \lesssim 7\,\mathrm{pc}$ (and $e_0 \leq 0.99$), both scenarios are equally preferred. Finally, the similarity of the χ^2-values despite strongly contrasting e_0 again emphasizes the degeneracy between the eccentricity and the stellar environment of the SMBHBs.

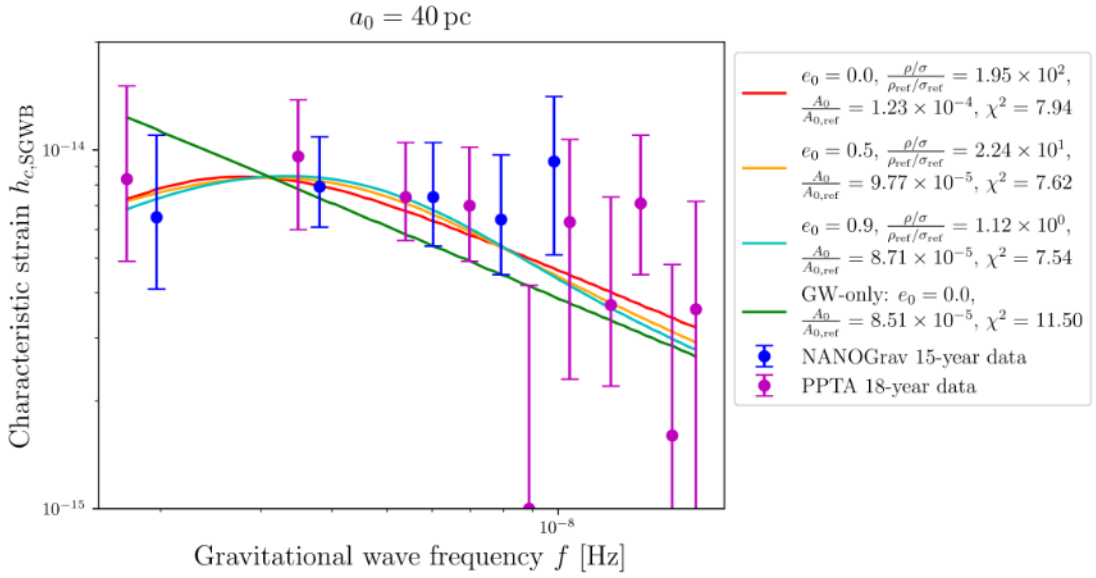

Fig. 4.13: $a_0 = 40\,\mathrm{pc}$: Best-fit SGWB spectrum for circular orbits ($e_0 = 0$, red), eccentric orbits with $e_0 = 0.5$ (orange) and 0.9 (cyan), respectively, as well as for the GW-only case (green), considering the lowest five frequency bins from the NANOGrav 15-year data set (blue) and the lowest ten frequency bins from the PPTA 18-year data set (violet). In addition to the best-fit values for $\frac{\rho/\sigma}{\rho_{\mathrm{ref}}/\sigma_{\mathrm{ref}}}$ and $A_0/A_{0,\mathrm{ref}}$, the corresponding values for χ^2 are also provided in the legend.

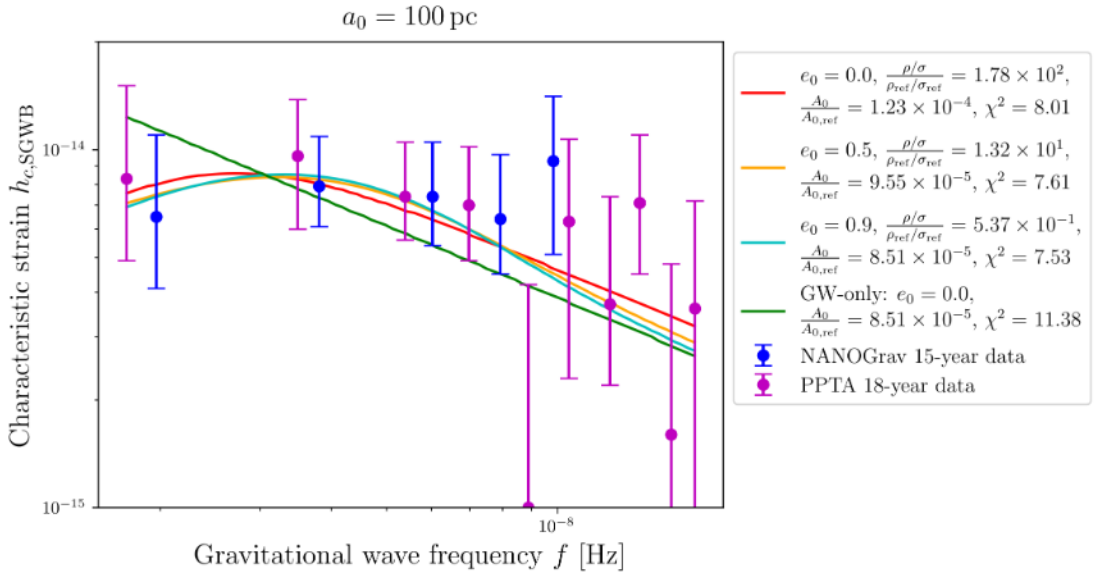

Fig. 4.14: $a_0 = 100\,\mathrm{pc}$: Best-fit SGWB spectrum for circular orbits ($e_0 = 0$, red), eccentric orbits with $e_0 = 0.5$ (orange) and 0.9 (cyan), respectively, as well as for the GW-only case (green), considering the lowest five frequency bins from the NANOGrav 15-year data set (blue) and the lowest ten frequency bins from the PPTA 18-year data set (violet). In addition to the best-fit values for $\frac{\rho/\sigma}{\rho_{\mathrm{ref}}/\sigma_{\mathrm{ref}}}$ and $A_0/A_{0,\mathrm{ref}}$, the corresponding values for χ^2 are also provided in the legend.

5 Conclusions

This study first investigates in detail the impact of the initial binary parameters e_0 and a_0 as well as the stellar environment on the shape of the nanohertz SGWB generated by a population of SMBHBs. It is demonstrated that both eccentric orbits and the interaction of the binary systems with surrounding stars via the gravitational slingshot mechanism lead to a turnover in the observed SGWB spectrum. For a fixed initial eccentricity e_0 and a fixed ratio of the stellar density ρ to the velocity dispersion σ at the influence radius, the exact position of this turnover further depends on the semi-major axis a_0 at the formation of the SMBHBs.

By analyzing the NANOGrav 15-year data and the PPTA 18-year data using a MCMC sampling algorithm, the corresponding model parameter space can be constrained. Despite a pronounced degeneracy between e_0 and ρ/σ, a stringent upper limit at the 99 % confidence level on ρ/σ can be identified. For values above a threshold of approximately 10^2 to $10^4\,\mathrm{M}_\odot/\mathrm{pc}^3\,(\mathrm{km/s})^{-1}$, depending on e_0, the attenuation of the SGWB due to the gravitational slingshot effect becomes too strong, and the resulting characteristic strain is inconsistent with the experimental data. Additionally, the parsec-scale ρ/σ value most favored by the data over a broad parameter space is approximately $10^2\,\mathrm{M}_\odot/\mathrm{pc}^3\,(\mathrm{km/s})^{-1}$. These findings provide insights into the dynamics and distribution of stars as well as the star formation rate near SMBHs in galactic centers[51] [122].

It is also important to note that the mechanism considered to describe the interaction with the environment is based purely on gravitational 3-body scatterings and is therefore not restricted to the nature of the matter. Consequently, this effect applies not only to stars but also to clumps of cold, collisionless dark matter. Determining the exact contributions of baryonic and dark matter in galactic cores will require further investigations. Observations of visible matter in the electromagnetic spectrum, for instance through the Square Kilometre Array [123], in conjunction with the results of this study and future releases of more precise PTA data (i.e., multi-messenger observations [124]), could help address fundamental questions about the composition of matter in SMBHBs and consequently the evolution of these systems.

Another important result of this work is that the turnover observed in current PTA data cannot be reproduced by a cosmic population of identical, purely GW-driven SMBHBs, provided these systems have a reasonable initial semi-major axis of $\mathcal{O}(10-100\,\mathrm{pc})$ and do not exhibit unphysically high initial eccentricities like $e_0 > 0.99$. Considering the interaction of SMBHBs with

[51] For comparison, the value for ρ/σ at a distance of 1 pc from Sagittarius A* is about $10^3\,\mathrm{M}_\odot/\mathrm{pc}^3\,(\mathrm{km/s})^{-1}$. This result is obtained by modeling a parsec-scale stellar core at the center of the Milky Way (see Ref. [121]).

their matter environment is essential to produce good fits especially to the lowest frequency bins. Future PTA data sets will show whether this finding proves robust.

Additionally, this study finds that the data-preferred value for the number density normalization A_0 of identical SMBHBs contributing to the SGWB is approximately $10^{-4}\,\mathrm{Mpc}^{-3}$. Since these SMBHBs are expected to dominate the stochastic background, this result can be used to get information about the minimum number of such binary systems in the local universe. This, in turn, could help impose further constraints on the galaxy merger rate and binary formation rate. Exploring this in more detail will be left for future work.

Nevertheless, it must be mentioned that the recent PTA data can also be explained by SMBHBs that lose energy not mainly through the gravitational slingshot effect but via the dynamical friction mechanism with DM of different types. In particular, theoretical SGWB models in which SMBHs are surrounded by spikes of self-interacting DM particles [41] or interact gravitationally with compact cores of wave-like, ultralight DM ("solitons") [125], [126] also provide good fits to the experimental data. Furthermore, a cosmological origin of the stochastic background cannot be excluded, as discussed at the beginning of this study.

The continued monitoring of the current pulsars as well as the inclusion of new ones is necessary to collect more data that will allow distinguishing between these different effects in future. For example, a more detailed examination of the anisotropy in the SGWB could offer insights into the degree of homogeneity in the distribution of the GW sources. For a discrete population of SMBHBs in the universe, deviations from isotropy are expected to be at a significantly higher level than for cosmological sources [22]. In combination with the detection of correlations among the data at different frequency bins, this would serve as a strong indication that the SGWB originates from eccentric SMBHBs [35]. Moreover, incorporating additional GW frequency bands through future detectors such as LISA or next-generation astrometry missions[52] [129] could be crucial in ruling out certain theoretical models [130]. For instance, SMBHs in binary systems merge at certain frequencies, ceasing to emit strong GWs afterward, which could lead to an additional diminution of the SGWB in the micro- to millihertz range.

In summary, it is very important not to overlook other theories that could also explain the observed SGWB in the nanohertz frequency regime. However, the results of this work affirms the existence of the gravitational slingshot effect as an efficient mechanism for extracting orbital

[52]Astrometry missions such as Gaia [127] or Roman [128] enable precise measurements of stellar positions. They contribute to the indirect detection of GWs by observing their effects on the apparent motion of stars.

energy from SMBHBs before they enter the GW-dominated phase of their evolution.

Acknowledgements

Over the past 18 months, I have had the privilege of experiencing so much and meeting many amazing new people. I wrote and published my first paper, became part of another international collaboration, and lived in Los Angeles for nine weeks. I owe a significant part of this to you, Laura. Thank you for giving me the opportunity to work with Yifan, Xiao, and Lei on a fascinating project that led to our first joint publication and laid the foundation for this thesis. Thank you for introducing me to Kris Pardo. He is not only an intelligent physicist but also a unique person. I very enjoyed my time in his research group at the University of Southern California. I will never forget this time. Living in the USA for nine weeks, getting to know the culture and the incredible scales of this country, enjoying the daily summer weather with over 30 °C, and working with Kris was an exceptional opportunity. I am very much looking forward to our upcoming years of research together, Laura.

At this point, I also want to thank you, Kris, for everything. Thank you for this indescribably wonderful experience. I greatly enjoyed the meetings with you and your research group as well as the visit to your home and our lunches. I would be delighted to invite you to my family's restaurant the next time you visit Frankfurt and to help you with learning German.

I also want to extend my gratitude to Prof. Dr. Jürgen Schaffner-Bielich for his work as second reviewer of this thesis. Additionally, I thank all the proofreaders for their helpful feedback.

Moreover, I would like to thank the Deutschlandstipendium at Goethe University for the financial support during my master studies, and the International Lab Visit Scholarship Program for funding my stay in the USA.

With this thesis I close another chapter of my life and will soon begin the next within my academic career, which will certainly present me with new and exciting challenges.

Throughout not only my physics studies but also the various stages of my life my entire family has stood by me. Without your endless support, Mama and Papa, many doors to this world would have remained closed to me. You gave me the opportunity and, most importantly, the courage to open those doors and achieve something unique beyond them. Both of you, and especially you, Pascal, are always by my side and I know I can always count on you.

Let's get the PhD together!

A Discussion on the Factor ξ_{peak}

In order to calculate the SGWB generated by SMBHBs with *eccentric* orbits, all harmonics must theoretically be taken into account. Since this number is infinite, an accurate estimate for the order of the last non-neglected harmonic $n_{\mathrm{max}}(e, \xi_{\mathrm{peak}})$, which depends on the eccentricity e and $\xi_{\mathrm{peak}} \in \mathbb{N}$ (see Subsec. 2.6), is required so that the difference between the associated approximation for the SGWB and the exact result can be considered negligible. At the same time, it must be ensured that n_{max} does not become too large for high eccentricities, so that the computing time remains moderate to test fit parameter combinations over a wide range within the MCMC sampling algorithm. This chapter provides a detailed discussion on why $\xi_{\mathrm{peak}} = 3$ guarantees both of the above mentioned conditions in a sufficient manner. But first, it needs to be clarified why it is even possible to truncate the infinite sum for calculating $h^2_{c,\mathrm{SGWB}}$ according to Eq. 2.48 after a certain order, denoted as n_{max}.

Each summand S_n contributing to $h^2_{c,\mathrm{SGWB}}$ exhibits the following n-dependence:

$$S_n = \frac{C_{\mathrm{A}}\,(1/n)^{10/3}}{n\,[C_{\mathrm{3B}}\,(1/n)^{1/3} + C_{\mathrm{GW}}\,(1/n)^{11/3}]}\,g(n,e) = \frac{C_{\mathrm{A}}\,(1/n)^{2/3}}{C_{\mathrm{3B}}\,n^{10/3} + C_{\mathrm{GW}}}\,g(n,e)\,, \tag{A.1}$$

with $C_{\mathrm{A}}, C_{\mathrm{GW}} > 0$ and $C_{\mathrm{3B}} \geq 0$ as constants independent of n. It can be easily shown that the first term in Eq. A.1 approaches zero as $n \to \infty$ ($\propto n^{-4}$ for large n). That this is also the case for $g(n,e)$ is evident from Fig. A.1, where $g(n,e)$ is plotted as a function of n for three different eccentricities $e = 0.1, 0.5$ and 0.9 (see Eq. 2.22). Consequently, S_n converges sufficiently quickly to zero as $n \to \infty$, implying that summing over a finite number of harmonics is acceptable for calculating the SGWB.

Using the `SMBHBpy` code, it can be found that the SGWB spectra for, for example, $\xi_{\mathrm{peak}} = 10$ and $\xi_{\mathrm{peak}} = 100$ are (practically) indistinguishable[53]. This is even the case for very high eccentricities and not surprising due to the previously discussed convergence behavior of S_n. Consequently, beyond a certain value of ξ_{peak}, it makes (almost) no difference whether all harmonics are considered for the SGWB calculation or only those up to the corresponding $n_{\mathrm{max}}(e, \xi_{\mathrm{peak}})$. For this reason, the case for $\xi_{\mathrm{peak}} = 100$ will be referred to as the "truth" in the following.

However, n_{max} should not become too large, especially for huge e, in order to keep the computing time within a reasonable limit. For instance, the computing time for a single calculation of the

[53] To be more precise, the ratio of the results for $h_{c,\mathrm{SGWB}}$ for these two ξ_{peak} values is (nearly) one.

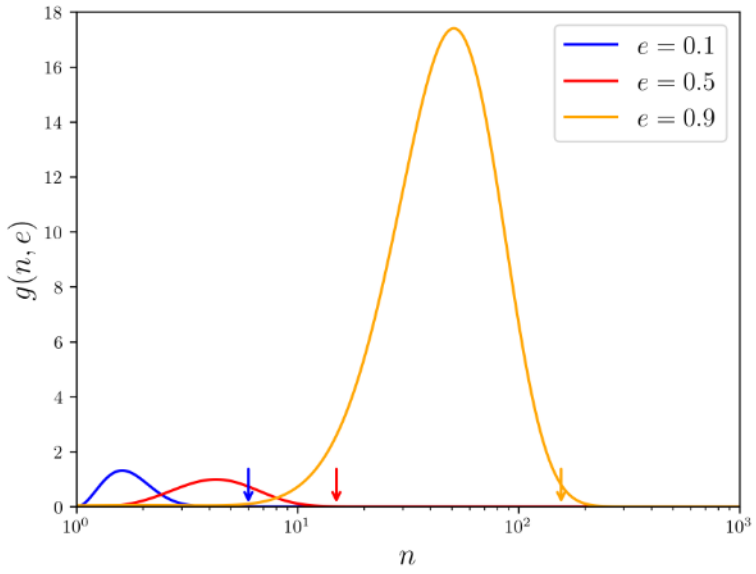

Fig. A.1: GW distribution function $g(n, e)$ for (continuous) n and three different eccentricities $e = 0.1, 0.5$ and 0.9 (blue, red, and orange). The colored arrows indicate the corresponding values for $n_{\text{max}}(e, \xi_{\text{peak}} = 3)$, according to Eq. 2.47.

SGWB for identical SMBHBs with $e_{\text{max}} = 0.99$ using $\xi_{\text{peak}} = 3$ already exceeds two minutes[54] (utilizing an Intel i5-7300HQ CPU). Therefore, one must consider the question of what deviation can be tolerated between the "truth" and the result obtained for small ξ_{peak}.

In Fig. A.2, the percentage deviation from the "truth" is presented for $\xi_{\text{peak}} = 1, 2, 3$, and 4 (blue, red, orange, and green) across a wide GW frequency range. As expected, the relative difference increases with increasing eccentricity for each case. While the deviation for $\xi_{\text{peak}} = 1$ is a few percent over a wide frequency range, this quantity remains below a maximum of $\sim 10^{-4}$ for $\xi_{\text{peak}} = 3$, even for high eccentricities. This value is certainly acceptable for determining the SGWB across a broad parameter space[55]. Besides, the numerical calculation of the stochastic background would take too long for $\xi_{\text{peak}} > 3$. Additionally, it is noticeable that the frequency range in which the deviation differs from almost zero shrinks and becomes more concentrated around the turnover, marked by the vertical dashed black line, with increasing eccentricity.

For completeness, it is important to mention that the findings presented in this chapter are independent of a specific value for a_0 and ρ/σ. The values used for these two quantities in Fig. A.2 were chosen solely to place the turnover of the SGWB spectrum within the PTA band.

[54]The combination of e_{max} and ξ_{peak} corresponds to $n_{\text{max}} = 4{,}905$ (see Fig. 2.3).

[55]This choice was also motivated by Refs. [45] and [32], which adopt $\xi_{\text{peak}} = 3$ and $\xi_{\text{peak}} = 4$ in their analyses, respectively.

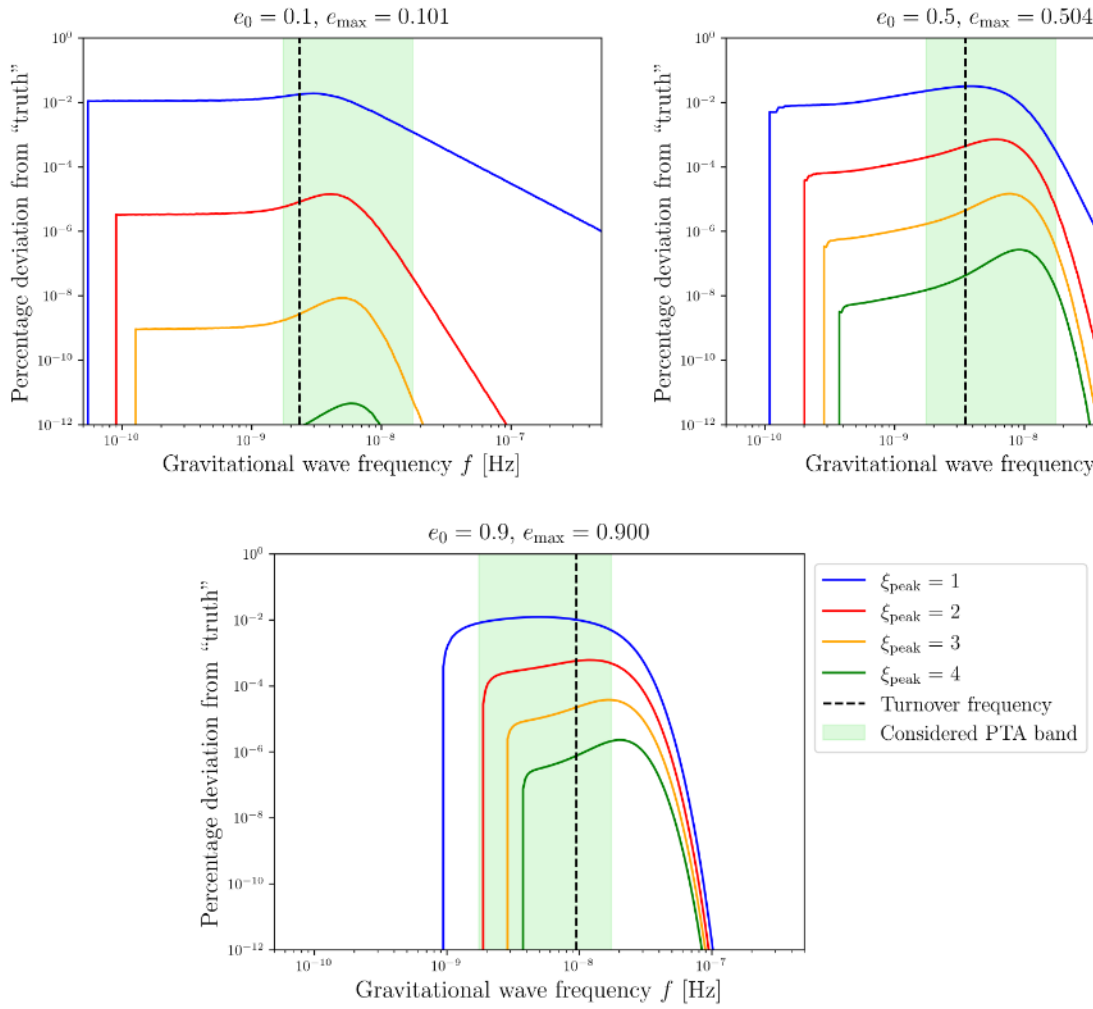

Fig. A.2: Relative difference between the result for the SGWB for $\xi_{\text{peak}} = 100$, referred to as "truth", and $\xi_{\text{peak}} = 1, 2, 3, 4$ (blue, red, orange, green) across a wide GW frequency range, considering three different initial eccentricities $e_0 = 0.1, 0.5$ and 0.9. The associated maximum eccentricity $e_{\max}$ reached by the identical SMBHBs with parameters $\{m_1, q, z, a_0, H, \frac{\rho/\sigma}{\rho_{\text{ref}}/\sigma_{\text{ref}}}\} = \{3 \times 10^9\,\text{M}_\odot, 0.65, 0.3, 1\,\text{pc}, 18, 10^2\}$ is also given in the title of each subplot. It should be recalled that $e_{\max}$ is used to calculate $n_{\max}$. As a reference, the frequency at which the turnover occurs in the SGWB spectrum is represented by a vertical dashed black line. Additionally, the PTA frequency band considered in this work is highlighted in light green.

B Testing the SMBHBpy Code: Reproduction of the Results from Ref. [46]

The reproduction of results from other studies provides a solid foundation for verifying the accuracy of one's own approaches, especially when developing new concepts based on the findings of these works. Therefore, this chapter demonstrates that the method for calculating the SGWB from SMBHBs, presented in Subsec. 3.1, produces results in excellent agreement with those from Ref. [46].

In Fig. B.1, the results from Fig. 4 of Ref. [46] (black dashed lines), under the condition that no harmonic contributes to the SGWB for $f < f_{\mathrm{min}} = 10^{-10}\,\mathrm{Hz}$, are compared with the outcomes obtained from the method used in this study for four different initial eccentricities $e_0 = 0.3, 0.6, 0.9$, and 0.99 (orange, red, green, and violet). The comparisons are based on the SGWB generated by a population of identical SMBHBs, which have a chirp mass of $\mathcal{M}_c = 4.16 \times 10^8\,\mathrm{M}_\odot$ as well as a redshift of $z = 0.02$, and are surrounded by vacuum, meaning

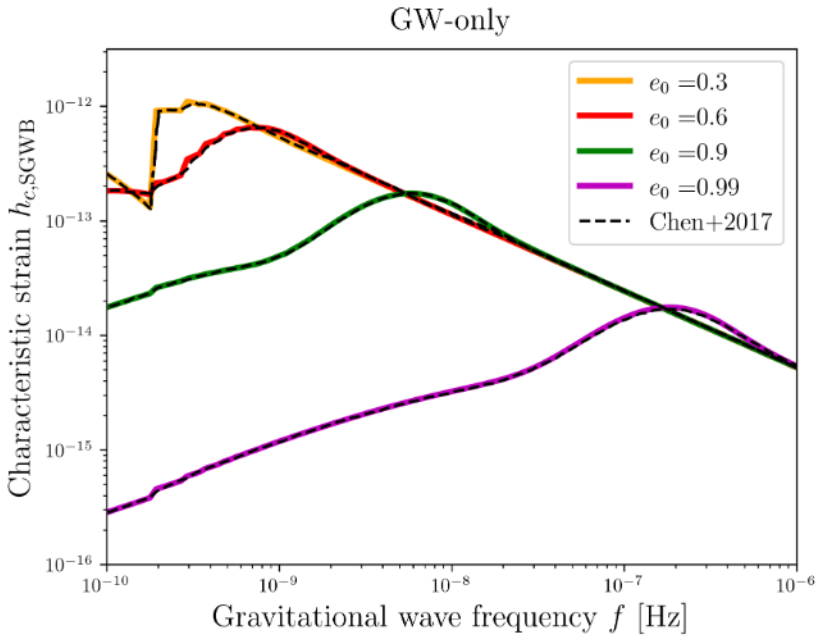

Fig. B.1: Comparison of the results from Fig. 4 of Ref. [46] (black dashed lines, referred to as "Chen+2017") with those obtained utilizing the method for calculating the SGWB described in Subsec. 3.1, under consideration of different initial eccentricities $e_0 = 0.3, 0.6, 0.9$, and 0.99 (orange, red, green, and violet). $\{\mathcal{M}_c, z, A_0\} = \{4.16 \times 10^8\,\mathrm{M}_\odot, 0.02, 1\,\mathrm{Mpc}^{-3}\}$.
Note: The positions of the steps in the spectrum correspond to frequencies at which important low-order harmonics begin to contribute to the SGWB.

they lose energy only through the emission of GWs during their evolution (GW-only). Furthermore, a number density normalization of $A_0 = 1\,\mathrm{Mpc}^{-3}$ is used.

While the authors of Ref. [46] chose $n_{\mathrm{max}} = 12{,}500$ for all initial eccentricities, this study considers $\xi_{\mathrm{peak}} = 3$, as discussed in Chap. A, to reproduce their findings. This leads to $n_{\mathrm{max}} = 9, 21, 156$, and 4,905 depending on the respective value for e_0. Since the results from both methods are nearly identical, it can be concluded again that $\xi_{\mathrm{peak}} = 3$ is an appropriate choice and thus that a significantly lower number of harmonics than 12,500 is sufficient to calculate the SGWB, even for highly eccentric SMBHBs.

Finally, to satisfy the above mentioned condition about the contribution of the harmonics, the initial semi-major axis is set to $a_0 = \left[\frac{n_{\mathrm{min}}^2 G\, m_1 (1+q)}{(2\pi(1+z) f_{\mathrm{min}})^2}\right]^{1/3} \approx 0.22\,\mathrm{pc}$ with $n_{\mathrm{min}} = 1$, $m_1 \approx 4.78 \times 10^8\,\mathrm{M}_\odot$ and $q = 1$. The choice of m_1 and q gives $\mathcal{M}_c = 4.16 \times 10^8\,\mathrm{M}_\odot$, according to Eq. 2.35.

C Supplementary MCMC Results

In this chapter, the corner plots are presented, which could not be included in the main body of this work but still play an important role in analyzing the results. First, however, the parameter evolution during the MCMC sampling will be provided, using the example of $a_0 = 1\,\mathrm{pc}$ for the cases "3B+GW, circular", "GW-only", and "3B+GW". The associated figures show that the values for $A_0/A_{0,\mathrm{ref}}$ settle around 10^{-4} throughout the sampling process, while a pronounced degeneracy exists between e_0 and ρ/σ.

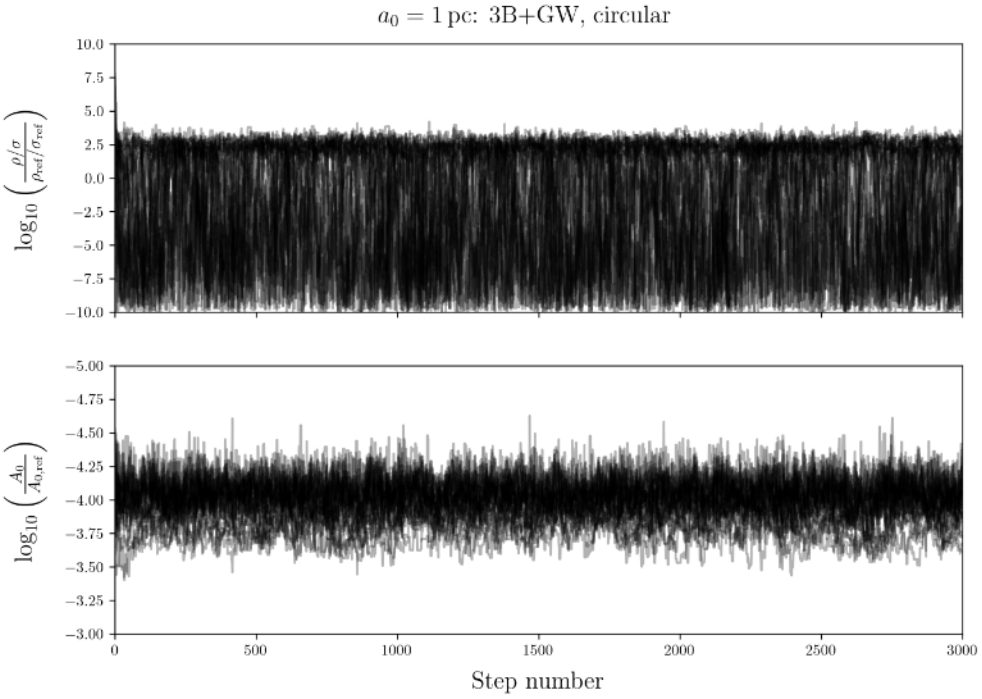

Fig. C.1: 3B+GW, circular: Evolution of the model parameters $\log_{10}(\rho/\sigma)$ and A_0 during the MCMC sampling process for $a_0 = 1\,\mathrm{pc}$.

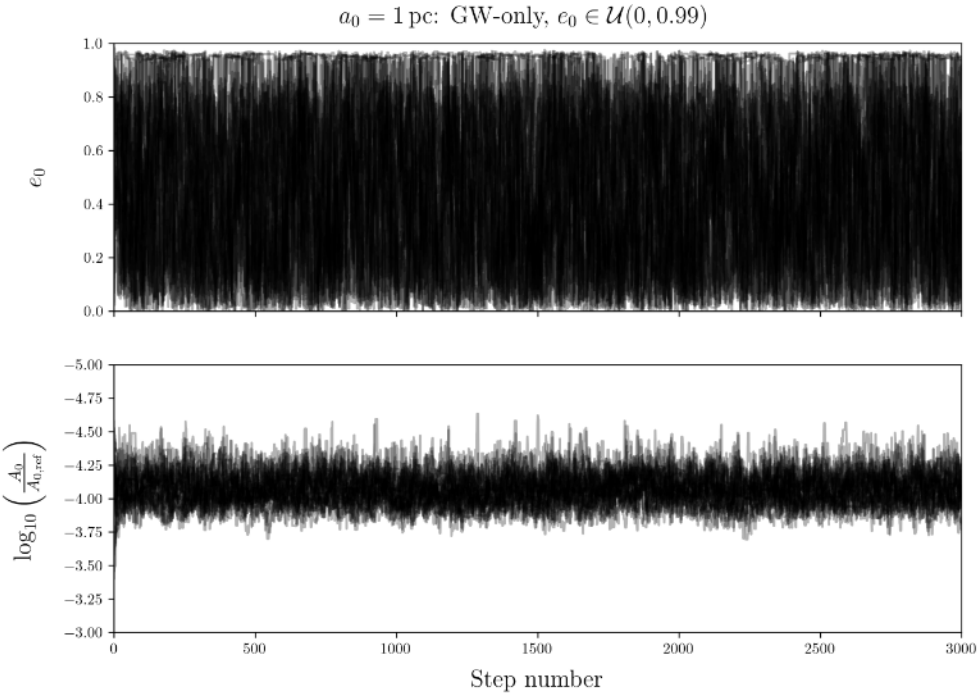

Fig. C.2: GW-only: Evolution of the model parameters e_0 and A_0 during the MCMC sampling process for $a_0 = 1\,\mathrm{pc}$ and $e_0 \in \mathcal{U}(0, 0.99)$.

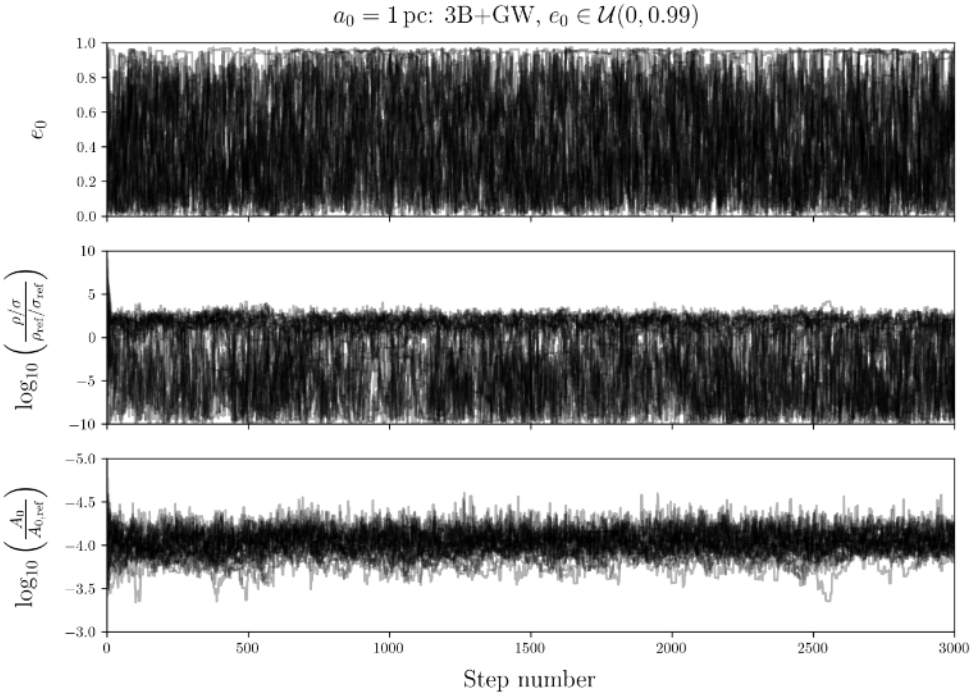

Fig. C.3: 3B+GW: Evolution of the model parameters e_0, $\log_{10}(\rho/\sigma)$ and A_0 during the MCMC sampling process for $a_0 = 1\,\mathrm{pc}$ and $e_0 \in \mathcal{U}(0, 0.99)$.

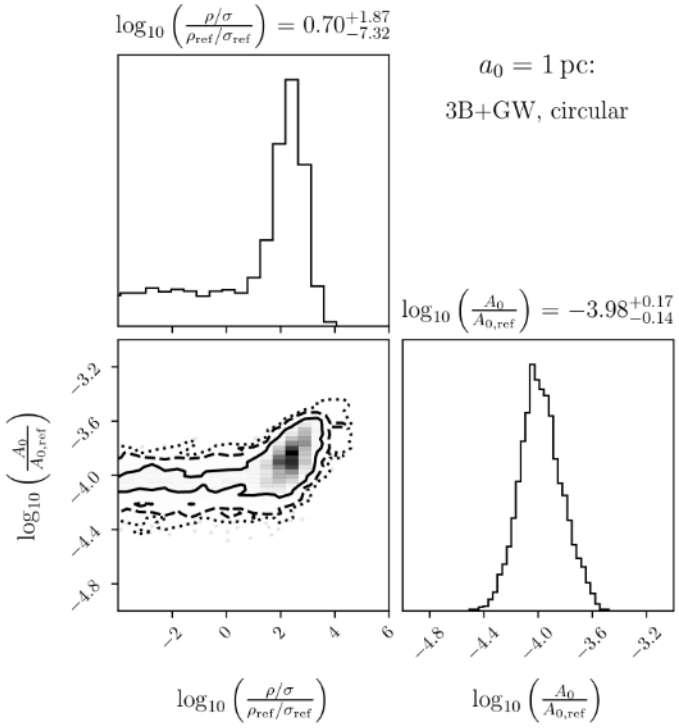

Fig. C.4: $a_0 = 1\,\mathrm{pc}$ (3B+GW, circular): Approximated one- and two-dimensional posterior distributions for the fit parameters $\log_{10}(\rho/\sigma)$ and A_0.

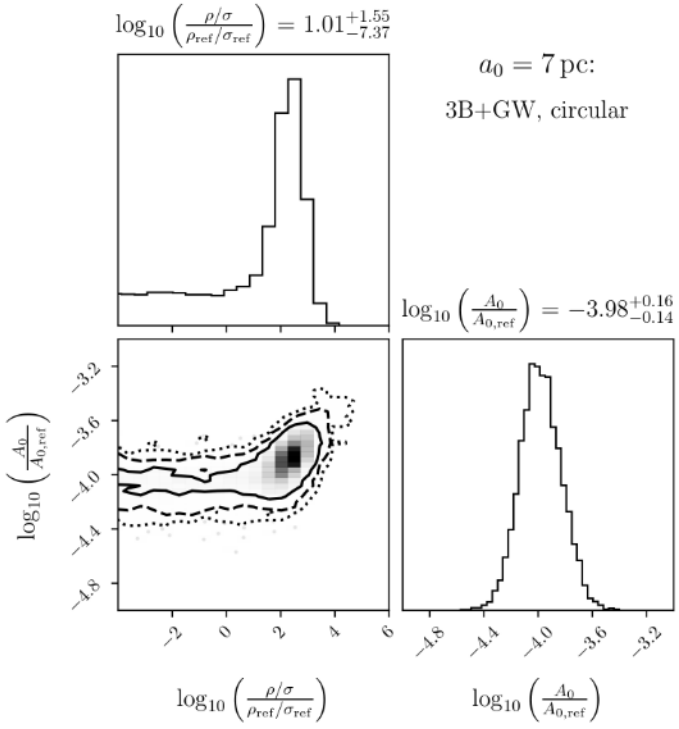

Fig. C.5: $a_0 = 7\,\mathrm{pc}$ (3B+GW, circular): Approximated one- and two-dimensional posterior distributions for the fit parameters $\log_{10}(\rho/\sigma)$ and A_0.

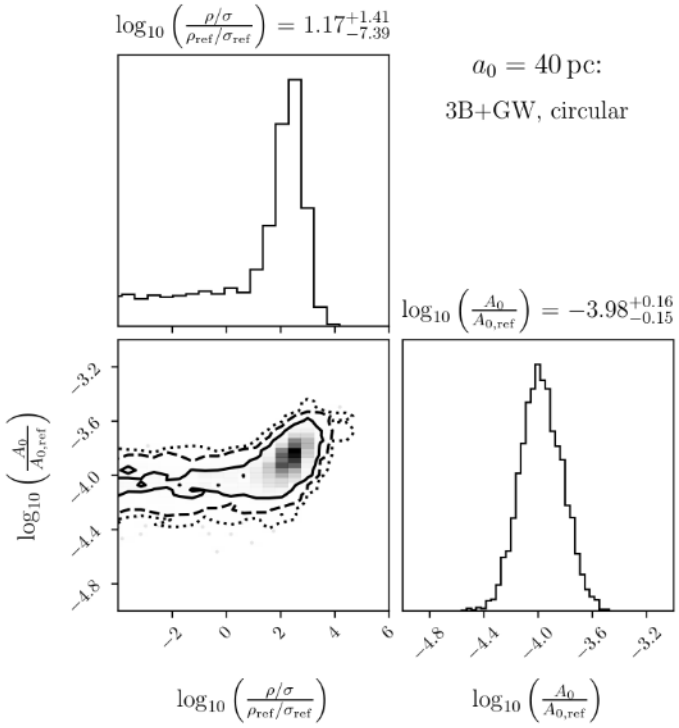

Fig. C.6: $a_0 = 40\,\mathrm{pc}$ (3B+GW, circular): Approximated one- and two-dimensional posterior distributions for the fit parameters $\log_{10}(\rho/\sigma)$ and A_0.

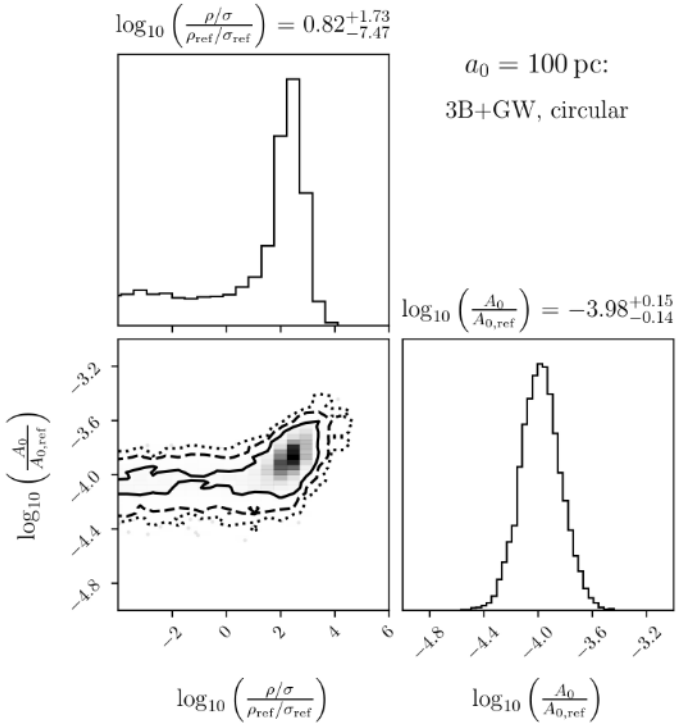

Fig. C.7: $a_0 = 100\,\mathrm{pc}$ (3B+GW, circular): Approximated one- and two-dimensional posterior distributions for the fit parameters $\log_{10}(\rho/\sigma)$ and A_0.

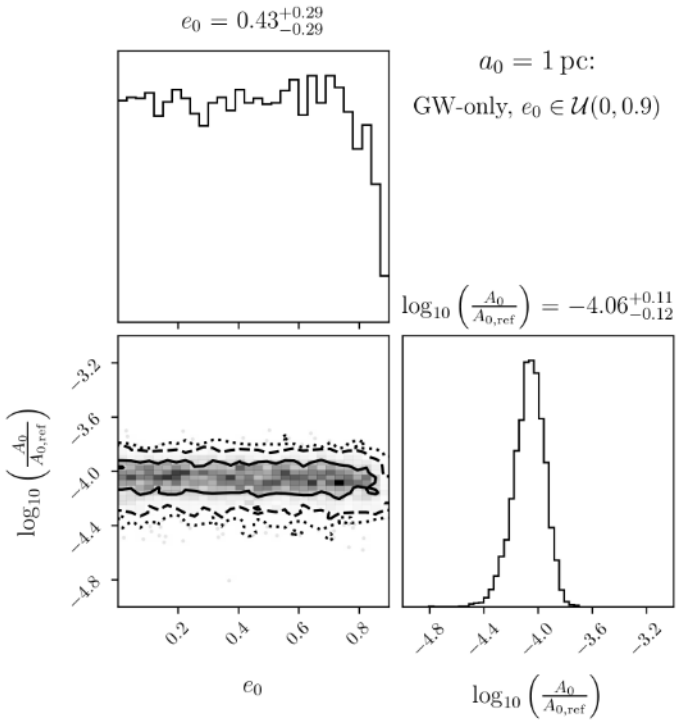

Fig. C.8: $a_0 = 1\,\mathrm{pc}$ (GW-only, $e_0 \in \mathcal{U}(0, 0.9)$): Approximated one- and two-dimensional posterior distributions for the fit parameters e_0 and A_0.

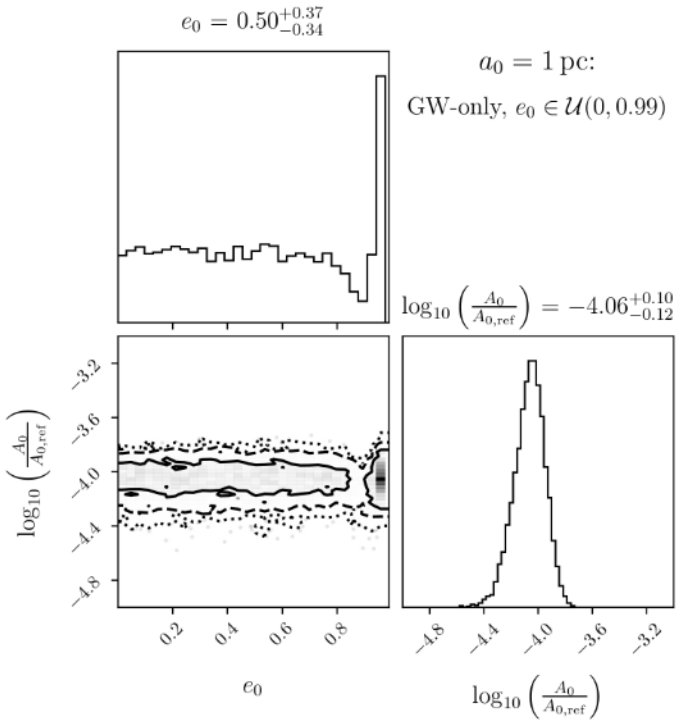

Fig. C.9: $a_0 = 1\,\mathrm{pc}$ (GW-only, $e_0 \in \mathcal{U}(0, 0.99)$): Approximated one- and two-dimensional posterior distributions for the fit parameters e_0 and A_0.

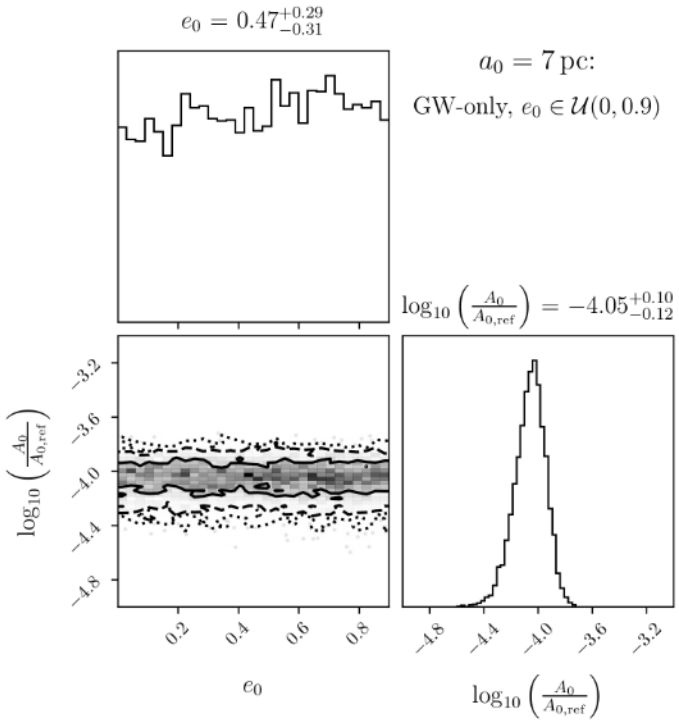

Fig. C.10: $a_0 = 7\,\mathrm{pc}$ (GW-only, $e_0 \in \mathcal{U}(0, 0.9)$): Approximated one- and two-dimensional posterior distributions for the fit parameters e_0 and A_0.

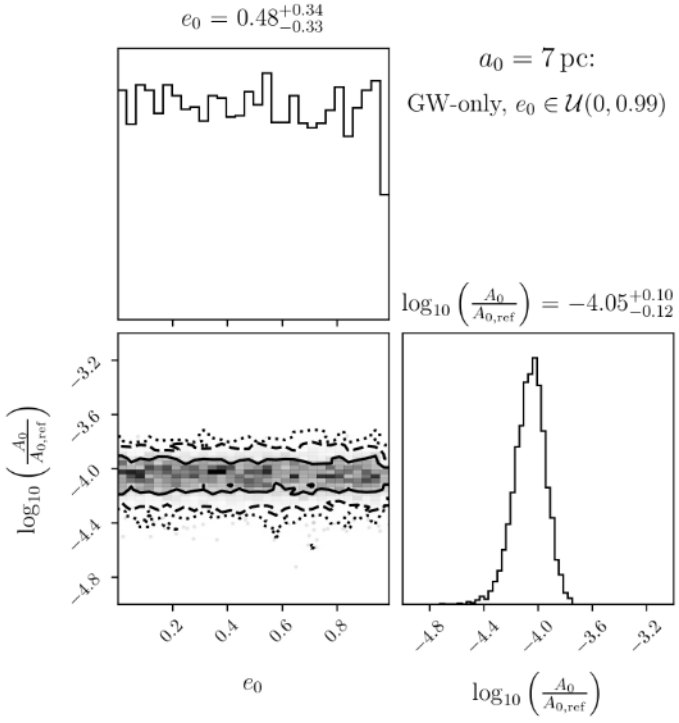

Fig. C.11: $a_0 = 7\,\mathrm{pc}$ (GW-only, $e_0 \in \mathcal{U}(0, 0.99)$): Approximated one- and two-dimensional posterior distributions for the fit parameters e_0 and A_0.

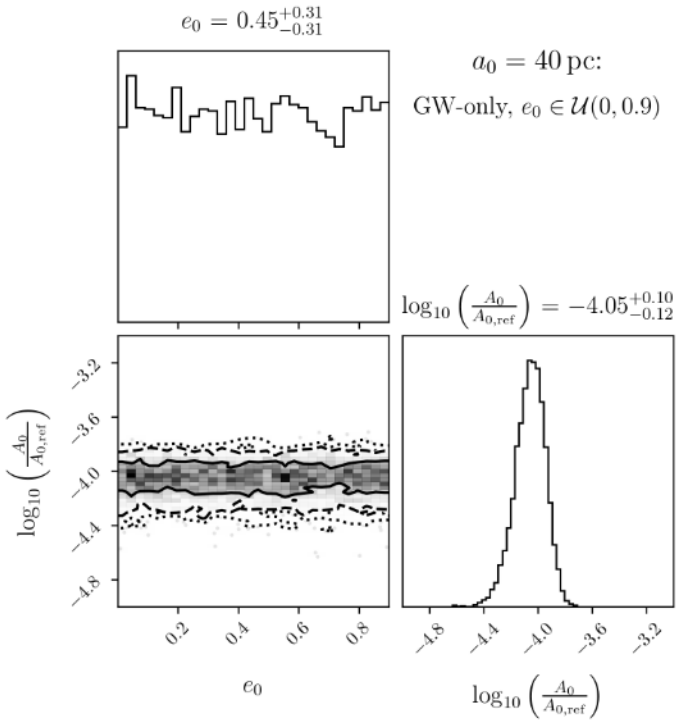

Fig. C.12: $a_0 = 40\,\mathrm{pc}$ (GW-only, $e_0 \in \mathcal{U}(0, 0.9)$): Approximated one- and two-dimensional posterior distributions for the fit parameters e_0 and A_0.

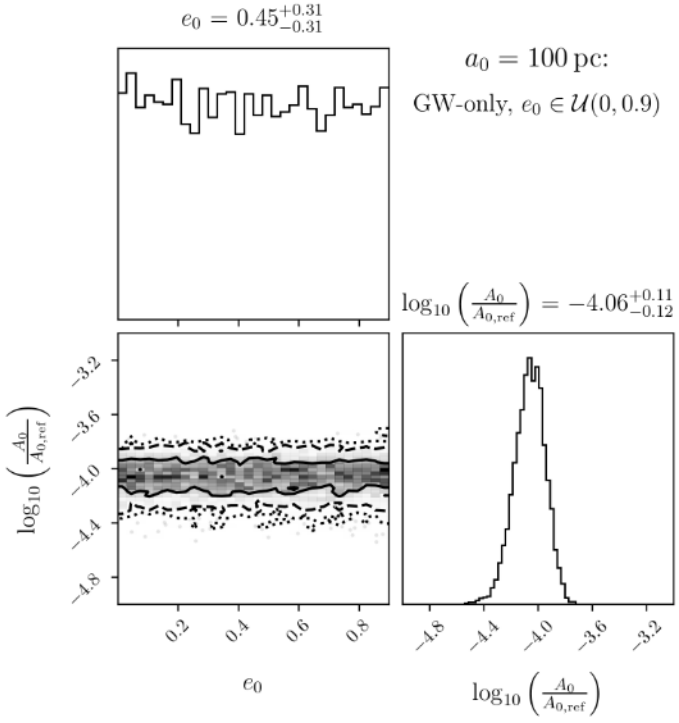

Fig. C.13: $a_0 = 100\,\mathrm{pc}$ (GW-only, $e_0 \in \mathcal{U}(0, 0.9)$): Approximated one- and two-dimensional posterior distributions for the fit parameters e_0 and A_0.

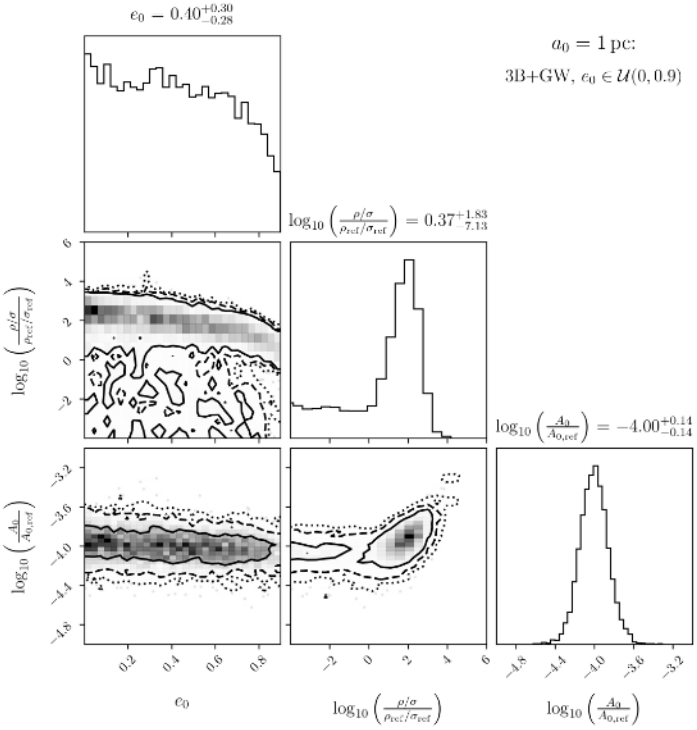

Fig. C.14: $a_0 = 1\,\mathrm{pc}$ (3B+GW, $e_0 \in \mathcal{U}(0, 0.9)$): Approximated one- and two-dimensional posterior distributions for the fit parameters $e_0, \log_{10}(\rho/\sigma)$ and A_0.

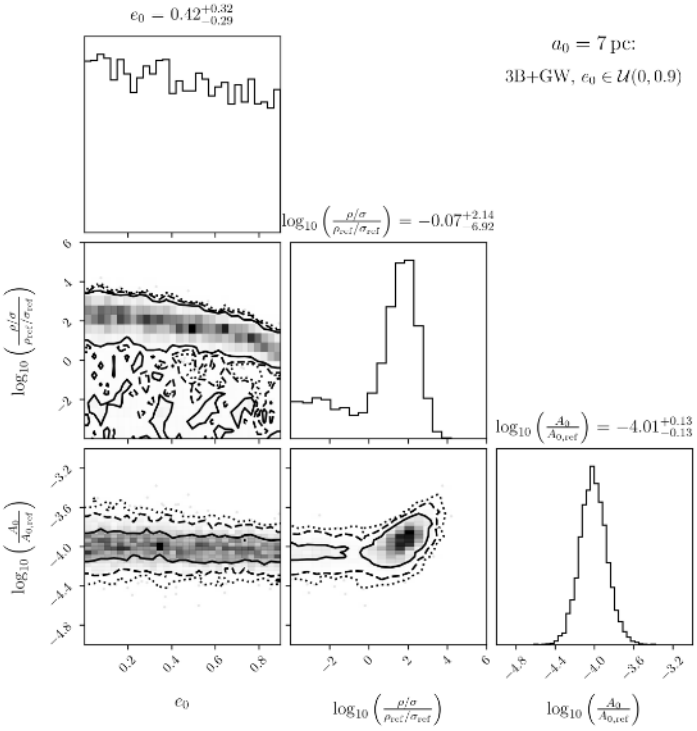

Fig. C.15: $a_0 = 7\,\mathrm{pc}$ (3B+GW, $e_0 \in \mathcal{U}(0, 0.9)$): Approximated one- and two-dimensional posterior distributions for the fit parameters $e_0, \log_{10}(\rho/\sigma)$ and A_0.

References

[1] Y. Chen, M. Daniel, L. Sagunski, X. Xue, and *The NANOGrav Collaboration*, "Galaxy Tomography with the Gravitational Wave Background from Supermassive Black Hole Binaries," Nov. 2024. arXiv: 2411.05906.

[2] M. Daniel, K. Pardo, and L. Sagunski, "Forecasted Detection Limits on the (Dark) Matter Density in Supermassive Black Hole Binaries for LISA," Jan. 2025. arXiv: 2501.13601.

[3] M. Daniel, "Constraining Dark Matter with Gravitational Waves from Supermassive Black Hole Binaries using Cassini Data," Aug. 2023. DOI: 10.21248/gups.79949.

[4] A. Mitridate, D. Wright, R. von Eckardstein, *et al.*, "`PTArcade`," Jun. 2023. arXiv: 2306.16377.

[5] N. Becker, "`IMRIpy`: Intermediate Mass Ratio Inspirals Simulator," Aug. 2021. [Online]. Available: https://github.com/DMGW-Goethe/imripy.

[6] M. H. Gregory, "Advanced LIGO: The Next Generation of Gravitational Wave Detectors," *Classical and Quantum Gravity*, vol. 27, no. 8, p. 084 006, Apr. 2010. DOI: 10.1088/0264-9381/27/8/084006.

[7] B. P. Abbott *et al.*, "Observation of Gravitational Waves from a Binary Black Hole Merger," *Physical Review Letters*, vol. 116, no. 6, Feb. 2016, ISSN: 1079-7114. DOI: 10.1103/physrevlett.116.061102.

[8] F. Acernese *et al.*, "Advanced Virgo Baseline Design - Technical Report VIR-0027A-09," May 2009. [Online]. Available: https://tds.virgo-gw.eu/?call_file=VIR-0027A-09.pdf.

[9] T. Akutsu, M. Ando, K. Arai, *et al.*, "Overview of KAGRA: Detector Design and Construction History," May 2020. arXiv: 2005.05574.

[10] C. J. Moore, R. H. Cole, and C. P. L. Berry, "Gravitational Wave Sensitivity Curves," *Classical and Quantum Gravity*, vol. 32, no. 1, p. 015 014, Dec. 2014, ISSN: 1361-6382. DOI: 10.1088/0264-9381/32/1/015014.

[11] ET Steering Committee Editorial Team, "Einstein Telescope - Design Report Update ET-0007C-20," Sep. 2020. [Online]. Available: https://apps.et-gw.eu/tds/ql/?c=15418.

[12] N. van Remortel, K. Janssens, and K. Turbang, "Stochastic Gravitational Wave Background: Methods and Implications," *Progress in Particle and Nuclear Physics*, vol. 128, p. 104 003, Jan. 2023, ISSN: 0146-6410. DOI: 10.1016/j.ppnp.2022.104003.

[13] B. P. Abbott *et al.*, "GW150914: Implications for the Stochastic Gravitational Wave Background from Binary Black Holes," *Physical Review Letters*, vol. 116, no. 13, Mar. 2016, ISSN: 1079-7114. DOI: 10.1103/physrevlett.116.131102.

[14] G. Agazie, A. Anumarlapudi, A. M. Archibald, *et al.*, "The NANOGrav 15-Year Data Set: Evidence for a Gravitational Wave Background," *The Astrophysical Journal Letters*, vol. 951, no. 1, p. L8, Jun. 2023, ISSN: 2041-8213. DOI: 10.3847/2041-8213/acdac6.

[15] M. Rajagopal and R. W. Romani, "Ultra-Low-Frequency Gravitational Radiation from Massive Black Hole Binaries," *The Astrophysical Journal*, vol. 446, p. 543, Jun. 1995, ISSN: 1538-4357. DOI: 10.1086/175813.

[16] G. Agazie, A. Anumarlapudi, A. M. Archibald, *et al.*, "The NANOGrav 15-Year Data Set: Constraints on Supermassive Black Hole Binaries from the Gravitational Wave Background," *The Astrophysical Journal Letters*, vol. 952, no. 2, p. L37, Aug. 2023, ISSN: 2041-8213. DOI: 10.3847/2041-8213/ace18b.

[17] C. Caprini and D. G. Figueroa, "Cosmological Backgrounds of Gravitational Waves," *Classical and Quantum Gravity*, vol. 35, no. 16, p. 163 001, Jul. 2018, ISSN: 1361-6382. DOI: 10.1088/1361-6382/aac608.

[18] M. Guzzetti, N. Bartolo, M. Liguori, and S. Matarrese, "Gravitational Waves from Inflation," *La Rivista del Nuovo Cimento*, vol. 39, pp. 399–495, May 2016. DOI: 10.1393/ncr/i2016-10127-1.

[19] A. Vilenkin, "Gravitational Radiation from Cosmic Strings," *Physics Letters B*, vol. 107, no. 1, pp. 47–50, Dec. 1981, ISSN: 0370-2693. DOI: 10.1016/0370-2693(81)91144-8.

[20] C. Caprini, M. Hindmarsh, S. Huber, *et al.*, "Science with the Space-Based Interferometer eLISA. II: Gravitational Waves from Cosmological Phase Transitions," *Journal of Cosmology and Astroparticle Physics*, vol. 2016, no. 04, pp. 001–001, Apr. 2016, ISSN: 1475-7516. DOI: 10.1088/1475-7516/2016/04/001.

[21] G. Domenech, "Scalar Induced Gravitational Waves Review," *Universe*, vol. 7, no. 11, p. 398, Oct. 2021, ISSN: 2218-1997. DOI: 10.3390/universe7110398.

[22] A. Afzal, G. Agazie, A. Anumarlapudi, *et al.*, "The NANOGrav 15-Year Data Set: Search for Signals from New Physics," *The Astrophysical Journal Letters*, vol. 951, no. 1, p. L11, Jun. 2023, ISSN: 2041-8213. DOI: 10.3847/2041-8213/acdc91.

[23] N. Christensen, "Stochastic Gravitational Wave Backgrounds," *Reports on Progress in Physics*, vol. 82, no. 1, p. 016 903, Nov. 2018, ISSN: 1361-6633. DOI: 10.1088/1361-6633/aae6b5.

[24] A. Penzias and R. Wilson, "A Measurement of Excess Antenna Temperature at 4080 Mc/s," vol. 142, pp. 419–421, Jul. 1965. DOI: 10.1086/148307.

[25] R. Durrer, "The Cosmic Microwave Background: The History of its Experimental Investigation and its Significance for Cosmology," *Classical and Quantum Gravity*, vol. 32, no. 12, p. 124 007, Jun. 2015. DOI: 10.1088/0264-9381/32/12/124007.

[26] R. Ding and C. Tian, "On the Anisotropies of the Cosmological Gravitational Wave Background from Pulsar Timing Array Observations," *Journal of Cosmology and Astroparticle Physics*, vol. 2024, no. 02, p. 016, Feb. 2024, ISSN: 1475-7516. DOI: 10.1088/1475-7516/2024/02/016.

[27] M. R. Sah, S. Mukherjee, V. Saeedzadeh, A. Babul, M. Tremmel, and T. R. Quinn, "Imprints of Supermassive Black Hole Evolution on the Spectral and Spatial Anisotropy of Nanohertz Stochastic Gravitational Wave Background," *Monthly Notices of the Royal Astronomical Society*, vol. 533, no. 2, pp. 1568–1582, Aug. 2024, ISSN: 1365-2966. DOI: 10.1093/mnras/stae1930.

[28] G. Agazie, A. Anumarlapudi, A. M. Archibald, *et al.*, "The NANOGrav 15-Year Data Set: Search for Anisotropy in the Gravitational Wave Background," Jun. 2023. arXiv: 2306.16221.

[29] S. R. Taylor and J. R. Gair, "Searching for Anisotropic Gravitational Wave Backgrounds using Pulsar Timing Arrays," *Physical Review D*, vol. 88, no. 8, Oct. 2013, ISSN: 1550-2368. DOI: 10.1103/physrevd.88.084001.

[30] C. M. F. Mingarelli, T. J. W. Lazio, A. Sesana, *et al.*, "The Local Nanohertz Gravitational Wave Landscape from Supermassive Black Hole Binaries," *Nature Astronomy*, vol. 1, no. 12, pp. 886–892, Nov. 2017, ISSN: 2397-3366. DOI: 10.1038/s41550-017-0299-6.

[31] N. Grimm, M. Pijnenburg, G. Cusin, and C. Bonvin, "The Impact of Large-Scale Galaxy Clustering on the Variance of the Hellings-Downs Correlation: Numerical Results," Nov. 2024. arXiv: 2411.08744.

[32] R. J. Truant, D. Izquierdo-Villalba, A. Sesana, G. M. Shaifullah, and M. Bonetti, "Resolving the Nanohertz Gravitational Wave Sky: The Detectability of Eccentric Binaries with PTA Experiments," Jul. 2024. arXiv: 2407.12078.

[33] P. Amaro-Seoane, J. Andrews, M. Arca Sedda, *et al.*, "Astrophysics with the Laser Interferometer Space Antenna," *Living Reviews in Relativity*, vol. 26, no. 1, Mar. 2023, ISSN: 1433-8351. DOI: 10.1007/s41114-022-00041-y.

[34] M. Enoki and M. Nagashima, "The Effect of Orbital Eccentricity on Gravitational Wave Background Radiation from Supermassive Black Hole Binaries," *Progress of Theoretical Physics*, vol. 117, no. 2, pp. 241–256, Feb. 2007, ISSN: 1347-4081. DOI: 10.1143/ptp.117.241.

[35] J. Raidal, J. Urrutia, V. Vaskonen, and H. Veermäe, "Eccentricity Effects on the Supermassive Black Hole Gravitational Wave Background," Jun. 2024. arXiv: 2406.05125.

[36] J. Ellis, M. Fairbairn, G. Hütsi, *et al.*, "Gravitational Waves from Supermassive Black Hole Binaries in Light of the NANOGrav 15-Year Data," *Physical Review D*, vol. 109, no. 2, Jan. 2024, ISSN: 2470-0029. DOI: 10.1103/physrevd.109.l021302.

[37] L. Z. Kelley, L. Blecha, and L. Hernquist, "Massive Black Hole Binary Mergers in Dynamical Galactic Environments," *Monthly Notices of the Royal Astronomical Society*, vol. 464, no. 3, pp. 3131–3157, Oct. 2016, ISSN: 1365-2966. DOI: 10.1093/mnras/stw2452.

[38] S. Chandrasekhar, "Dynamical Friction. I. General Considerations: The Coefficient of Dynamical Friction," *Astrophys. J.*, vol. 97, p. 255, May 1943. DOI: 10.1086/144517.

[39] J. Binney and S. Tremaine, *Galactic Dynamics: Second Edition*. Princeton University Press, Dec. 2008, ISBN: 9781400828722. DOI: doi:10.1515/9781400828722.

[40] P. Gondolo and J. Silk, "Dark Matter Annihilation at the Galactic Center," *Phys. Rev. Lett.*, vol. 83, pp. 1719–1722, Aug. 1999. DOI: 10.1103/PhysRevLett.83.1719.

[41] G. Alonso-Álvarez, J. M. Cline, and C. Dewar, "Self-Interacting Dark Matter Solves the Final Parsec Problem of Supermassive Black Hole Mergers," Jan. 2024. arXiv: 2401.14450.

[42] Z.-Q. Shen, G.-W. Yuan, Y.-Y. Wang, and Y.-Z. Wang, "Dark Matter Spike Surrounding Supermassive Black Holes Binary and the Nanohertz Stochastic Gravitational Wave Background," Jun. 2023. arXiv: 2306.17143.

[43] A. Sesana, "Insights into the Astrophysics of Supermassive Black Hole Binaries from Pulsar Timing Observations," *Classical and Quantum Gravity*, vol. 30, no. 22, p. 224 014, Nov. 2013, ISSN: 1361-6382. DOI: 10.1088/0264-9381/30/22/224014.

[44] S. R. Taylor, J. Simon, and L. Sampson, "Constraints on the Dynamical Environments of Supermassive Black Hole Binaries using Pulsar Timing Arrays," *Physical Review Letters*, vol. 118, no. 18, May 2017, ISSN: 1079-7114. DOI: 10.1103/physrevlett.118.181102.

[45] M. Bonetti, A. Franchini, B. G. Galuzzi, and A. Sesana, "Neural Networks Unveiling the Properties of Gravitational Wave Background from Supermassive Black Hole Binaries," *Astronomy and Astrophysics*, vol. 687, A42, Jun. 2024, ISSN: 1432-0746. DOI: 10.1051/0004-6361/202348433.

[46] S. Chen, A. Sesana, and W. Del Pozzo, "Efficient Computation of the Gravitational Wave Spectrum Emitted by Eccentric Massive Black Hole Binaries in Stellar Environments," *Monthly Notices of the Royal Astronomical Society*, vol. 470, no. 2, pp. 1738–1749, May 2017, ISSN: 1365-2966. DOI: 10.1093/mnras/stx1093.

[47] Y.-C. Bi, Y.-M. Wu, Z.-C. Chen, and Q.-G. Huang, "Implications for the Supermassive Black Hole Binaries from the NANOGrav 15-Year Data Set," *Science China Physics, Mechanics & Astronomy*, vol. 66, no. 12, Nov. 2023, ISSN: 1869-1927. DOI: 10.1007/s11433-023-2252-4.

[48] B. Kocsis and A. Sesana, "Gas-Driven Massive Black Hole Binaries: Signatures in the Nanohertz Gravitational Wave Background: Massive Black Holes and Pulsar Timing," *Monthly Notices of the Royal Astronomical Society*, vol. 411, no. 3, pp. 1467–1479, Jan. 2011, ISSN: 0035-8711. DOI: 10.1111/j.1365-2966.2010.17782.x.

[49] A. Escala, R. B. Larson, P. S. Coppi, and D. Mardones, "The Role of Gas in the Merging of Massive Black Holes in Galactic Nuclei. I. Black Hole Merging in a Spherical Gas Cloud," *The Astrophysical Journal*, vol. 607, no. 2, pp. 765–777, Jun. 2004, ISSN: 1538-4357. DOI: 10.1086/386278.

[50] J. P. W. Verbiest, M. Bailes, W. A. Coles, *et al.*, "Timing Stability of Millisecond Pulsars and Prospects for Gravitational Wave Detection," *Monthly Notices of the Royal Astronomical Society*, vol. 400, no. 2, pp. 951–968, Dec. 2009, ISSN: 1365-2966. DOI: 10.1111/j.1365-2966.2009.15508.x.

[51] D. Matsakis, J. Taylor, and M. Eubanks, "A Statistic for Describing Pulsar and Clock Stabilities," *Astronomy and Astrophysics*, vol. 326, pp. 924–928, Sep. 1997.

[52] R. S. Foster and D. C. Backer, "Constructing a Pulsar Timing Array," *Astrophysical Journal*, vol. 361, Sep. 1990, ISSN: 0004-637X. DOI: 10.1086/169195.

[53] S. Detweiler, "Pulsar Timing Measurements and the Search for Gravitational Waves," *Astrophysical Journal*, vol. 234, Dec. 1979. DOI: 10.1086/157593.

[54] M. Sazhin, "Opportunities for Detecting Ultralong Gravitational Waves," *Soviet Astronomy*, vol. 22, pp. 36–38, Jan. 1978.

[55] D. J. Reardon, A. Zic, R. M. Shannon, *et al.*, "Search for an Isotropic Gravitational Wave Background with the Parkes Pulsar Timing Array," *The Astrophysical Journal Letters*, vol. 951, no. 1, p. L6, Jun. 2023, ISSN: 2041-8213. DOI: 10.3847/2041-8213/acdd02.

[56] J. Antoniadis, P. Arumugam, S. Arumugam, *et al.*, "The Second Data Release from the European Pulsar Timing Array: IV. Implications for Massive Black Holes, Dark Matter and the Early Universe," May 2024. arXiv: 2306.16227.

[57] H. Xu, S. Chen, Y. Guo, *et al.*, "Searching for the Nanohertz Stochastic Gravitational Wave Background with the Chinese Pulsar Timing Array Data Release I," *Research in Astronomy and Astrophysics*, vol. 23, no. 7, p. 075 024, Jun. 2023, ISSN: 1674-4527. DOI: 10.1088/1674-4527/acdfa5.

[58] R. W. Hellings and G. S. Downs, "Upper Limits on the Isotropic Gravitational Radiation Background from Pulsar Timing Analysis," *Astrophysical Journal, Lett. Ed.*, vol. 265, Feb. 1983. DOI: 10.1086/183954.

[59] R. C. Bernardo and K.-W. Ng, "Charting the Nanohertz Gravitational Wave Sky with Pulsar Timing Arrays," Sep. 2024. arXiv: 2409.07955.

[60] J. D. Romano and B. Allen, "Answers to Frequently Asked Questions about the Pulsar Timing Array Hellings and Downs Curve," Aug. 2024. DOI: https://doi.org/10.1088/1361-6382/ad4c4c. arXiv: 2308.05847.

[61] S. Chen, A. Sesana, and C. J. Conselice, "Constraining Astrophysical Observables of Galaxy and Supermassive Black Hole Binary Mergers using Pulsar Timing Arrays," *Monthly Notices of the Royal Astronomical Society*, vol. 488, no. 1, pp. 401–418, Jun. 2019, ISSN: 0035-8711. DOI: 10.1093/mnras/stz1722.

[62] G. Kauffmann, S. D. M. White, and B. Guiderdoni, "The Formation and Evolution of Galaxies within Merging Dark Matter Halos," *Monthly Notices of the Royal Astronomical Society*, vol. 264, no. 1, pp. 201–218, Sep. 1993, ISSN: 0035-8711. DOI: 10.1093/mnras/264.1.201.

[63] M. C. Begelman, R. D. Blandford, and M. J. Rees, "Massive Black Hole Binaries in Active Galactic Nuclei," *Nature*, vol. 287, no. 5780, pp. 307–309, Sep. 1980. DOI: 10.1038/287307a0.

[64] B. Sundelius, M. Wahde, H. J. Lehto, and M. J. Valtonen, "A Numerical Simulation of the Brightness Variations of OJ 287," *The Astrophysical Journal*, vol. 484, no. 1, p. 180, Jul. 1997. DOI: 10.1086/304331.

[65] C. Rodriguez, G. B. Taylor, R. T. Zavala, A. B. Peck, L. K. Pollack, and R. W. Romani, "A Compact Supermassive Binary Black Hole System," *The Astrophysical Journal*, vol. 646, no. 1, pp. 49–60, Jul. 2006, ISSN: 1538-4357. DOI: 10.1086/504825.

[66] S. Iguchi, T. Okuda, and H. Sudou, "A Very Close Binary Black Hole in a Giant Elliptical Galaxy 3C 66B and its Black Hole Merger," *The Astrophysical Journal*, vol. 724, no. 2, pp. L166–L170, Nov. 2010, ISSN: 2041-8213. DOI: 10.1088/2041-8205/724/2/l166.

[67] J. Frank and M. J. Rees, "Effects of Massive Central Black Holes on Dense Stellar Systems," *Monthly Notices of the Royal Astronomical Society*, vol. 176, no. 3, pp. 633–647, Sep. 1976, ISSN: 0035-8711. DOI: 10.1093/mnras/176.3.633.

[68] D. Merritt, "Dynamics of Galaxy Cores and Supermassive Black Holes," *Reports on Progress in Physics*, vol. 69, no. 9, R01, Sep. 2006, ISSN: 1361-6633. DOI: 10.1088/0034-4885/69/9/r01.

[69] G. D. Quinlan, "The Dynamical Evolution of Massive Black Hole Binaries I. Hardening in a Fixed Stellar Background," *New Astronomy*, vol. 1, no. 1, pp. 35–56, Jul. 1996, ISSN: 1384-1076. DOI: 10.1016/s1384-1076(96)00003-6.

[70] N. Aghanim, Y. Akrami, M. Ashdown, *et al.*, "Planck 2018 Results: VI. Cosmological Parameters," *Astronomy and Astrophysics*, vol. 641, A6, Sep. 2020, ISSN: 1432-0746. DOI: 10.1051/0004-6361/201833910.

[71] S. Burke-Spolaor, "A Radio Census of Binary Supermassive Black Holes: VLBI Search for Double Black Holes," *Monthly Notices of the Royal Astronomical Society*, vol. 410, no. 4, pp. 2113–2122, Oct. 2010, ISSN: 0035-8711. DOI: 10.1111/j.1365-2966.2010.17586.x.

[72] L. Wang, J. E. Greene, W. Ju, R. R. Rafikov, J. J. Ruan, and D. P. Schneider, "Searching for Binary Supermassive Black Holes via Variable Broad Emission Line Shifts: Low Binary Fraction," *The Astrophysical Journal*, vol. 834, no. 2, p. 129, Jan. 2017, ISSN: 1538-4357. DOI: 10.3847/1538-4357/834/2/129.

[73] M. Milosavljević, *The Final Parsec Problem*. AIP, Oct. 2003, vol. 686, pp. 201–210. DOI: 10.1063/1.1629432.

[74] F. M. Khan, A. Just, and D. Merritt, "Efficient Merger of Binary Supermassive Black Holes in Merging Galaxies," *The Astrophysical Journal*, vol. 732, no. 2, p. 89, Apr. 2011, ISSN: 1538-4357. DOI: 10.1088/0004-637x/732/2/89.

[75] F. M. Khan, M. Preto, P. Berczik, I. Berentzen, A. Just, and R. Spurzem, "Mergers of Unequal-Mass Galaxies: Supermassive Black Hole Binary Evolution and Structure of Merger Remnants," *The Astrophysical Journal*, vol. 749, no. 2, p. 147, Apr. 2012, ISSN: 1538-4357. DOI: 10.1088/0004-637x/749/2/147.

[76] D. Merritt, "Loss-Cone Dynamics," *Classical and Quantum Gravity*, vol. 30, no. 24, p. 244 005, Nov. 2013, ISSN: 1361-6382. DOI: 10.1088/0264-9381/30/24/244005.

[77] F. M. Khan, D. Fiacconi, L. Mayer, P. Berczik, and A. Just, "Swift Coalescence of Supermassive Black Holes in Cosmological Mergers of Massive Galaxies," *The Astrophysical Journal*, vol. 828, no. 2, p. 73, Sep. 2016. DOI: 10.3847/0004-637X/828/2/73.

[78] E. Bortolas, A. Gualandris, M. Dotti, and J. I. Read, "The Influence of Massive Black Hole Binaries on the Morphology of Merger Remnants," *Monthly Notices of the Royal Astronomical Society*, vol. 477, no. 2, pp. 2310–2325, Mar. 2018, ISSN: 1365-2966. DOI: 10.1093/mnras/sty775.

[79] M. Dotti, M. Colpi, F. Haardt, and L. Mayer, "Supermassive Black Hole Binaries in Gaseous and Stellar Circumnuclear Discs: Orbital Dynamics and Gas Accretion," *Monthly Notices of the Royal Astronomical Society*, vol. 379, no. 3, pp. 956–962, Aug. 2007, ISSN: 1365-2966. DOI: 10.1111/j.1365-2966.2007.12010.x.

[80] F. G. Goicovic, C. Maureira-Fredes, A. Sesana, P. Amaro-Seoane, and J. Cuadra, "Accretion of Clumpy Cold Gas onto Massive Black Hole Binaries: A Possible Fast Route to Binary Coalescence," *Monthly Notices of the Royal Astronomical Society*, vol. 479, no. 3, pp. 3438–3455, Jun. 2018, ISSN: 1365-2966. DOI: 10.1093/mnras/sty1709.

[81] B. J. Kavanagh, D. A. Nichols, G. Bertone, and D. Gaggero, "Detecting Dark Matter around Black Holes with Gravitational Waves: Effects of Dark Matter Dynamics on the Gravitational Waveform," *Physical Review D*, vol. 102, no. 8, Oct. 2020, ISSN: 2470-0029. DOI: 10.1103/physrevd.102.083006.

[82] D. N. Spergel and P. J. Steinhardt, "Observational Evidence for Self-Interacting Cold Dark Matter," *Physical Review Letters*, vol. 84, no. 17, pp. 3760–3763, Apr. 2000, ISSN: 1079-7114. DOI: 10.1103/physrevlett.84.3760.

[83] T. Nakano and J. Makino, "On the Cusp around Central Black Holes in Luminous Elliptical Galaxies," *The Astrophysical Journal*, vol. 525, no. 2, p. L77, Oct. 1999. DOI: 10.1086/312338.

[84] D. Merritt, M. Milosavljević, L. Verde, and R. Jimenez, "Dark Matter Spikes and Annihilation Radiation from the Galactic Center," *Physical Review Letters*, vol. 88, no. 19, Apr. 2002, ISSN: 1079-7114. DOI: 10.1103/physrevlett.88.191301.

[85] A. Sesana, F. Haardt, and P. Madau, "Interaction of Massive Black Hole Binaries with their Stellar Environment. I. Ejection of Hypervelocity Stars," *The Astrophysical Journal*, vol. 651, no. 1, pp. 392–400, Nov. 2006, ISSN: 1538-4357. DOI: 10.1086/507596.

[86] S. Mikkola and M. J. Valtonen, "Evolution of Binaries in the Field of Light Particles and the Problem of Two Black Holes," *Monthly Notices of the Royal Astronomical Society*, vol. 259, no. 1, pp. 115–120, Nov. 1992, ISSN: 0035-8711. DOI: 10.1093/mnras/259.1.115.

[87] P. Hut and J. N. Bahcall, "Binary-Single Star Scattering. I - Numerical Experiments for Equal Masses," *The Astrophysical Journal*, vol. 268, pp. 319–341, May 1983. DOI: 10.1086/160956.

[88] E. Vasiliev, F. Antonini, and D. Merritt, "The Final Parsec Problem in the Collisionless Limit," *The Astrophysical Journal*, vol. 810, no. 1, p. 49, Aug. 2015, ISSN: 1538-4357. DOI: 10.1088/0004-637x/810/1/49.

[89] D. A. Forbes and T. J. Ponman, "On the Relationship between Age and Dynamics in Elliptical Galaxies," *Monthly Notices of the Royal Astronomical Society*, vol. 309, no. 3, pp. 623–628, Nov. 1999, ISSN: 1365-2966. DOI: 10.1046/j.1365-8711.1999.02868.x.

[90] H. Middleton, S. Chen, W. Del Pozzo, A. Sesana, and A. Vecchio, "No Tension between Assembly Models of Supermassive Black Hole Binaries and Pulsar Observations," *Nature Communications*, vol. 9, no. 1, Feb. 2018, ISSN: 2041-1723. DOI: 10.1038/s41467-018-02916-7.

[91] A. Sesana and F. M. Khan, "Scattering Experiments meet N-Body – I. A Practical Recipe for the Evolution of Massive Black Hole Binaries in Stellar Environments," *Monthly Notices of the Royal Astronomical Society: Letters*, vol. 454, no. 1, pp. L66–L70, Sep. 2015, ISSN: 1745-3933. DOI: 10.1093/mnrasl/slv131.

[92] A. Sesana, "Self Consistent Model for the Evolution of Eccentric Massive Black Hole Binaries in Stellar Environments: Implications for Gravitational Wave Observations," *The Astrophysical Journal*, vol. 719, no. 1, pp. 851–864, Jul. 2010, ISSN: 1538-4357. DOI: 10.1088/0004-637x/719/1/851.

[93] D. Merritt, "Black Holes and Galaxy Evolution," Oct. 1999. arXiv: astro-ph/9910546.

[94] M. Celoria, R. Oliveri, A. Sesana, and M. Mapelli, "Lecture Notes on Black Hole Binary Astrophysics," Jul. 2018. arXiv: 1807.11489.

[95] M. Maggiore, *Gravitational Waves: Volume 1: Theory and Experiments*. Oxford University Press, Oct. 2007, ISBN: 9780198570745. DOI: 10.1093/acprof:oso/9780198570745.001.0001.

[96] E. Hubble, "A Relation between Distance and Radial Velocity among Extra-Galactic Nebulae," *Proceedings of the National Academy of Science*, vol. 15, no. 3, pp. 168–173, Mar. 1929. DOI: 10.1073/pnas.15.3.168.

[97] P. C. Peters and J. Mathews, "Gravitational Radiation from Point Masses in a Keplerian Orbit," *Physical Review*, vol. 131, no. 1, pp. 435–440, Jul. 1963. DOI: 10.1103/PhysRev.131.435.

[98] P. C. Peters, "Gravitational Radiation and the Motion of Two Point Masses," *Phys. Rev.*, vol. 136, B1224–B1232, Nov. 1964. DOI: 10.1103/PhysRev.136.B1224.

[99] P. Amaro-Seoane, A. Sesana, L. Hoffman, *et al.*, "Triplets of Supermassive Black Holes: Astrophysics, Gravitational Waves and Detection," *Monthly Notices of the Royal Astronomical Society*, vol. 402, no. 4, pp. 2308–2320, Mar. 2010, ISSN: 1365-2966. DOI: 10.1111/j.1365-2966.2009.16104.x.

[100] L. S. Finn and K. S. Thorne, "Gravitational Waves from a Compact Star in a Circular, Inspiral Orbit, in the Equatorial Plane of a Massive, Spinning Black Hole, as Observed by LISA," *Physical Review D*, vol. 62, no. 12, Nov. 2000, ISSN: 1089-4918. DOI: 10.1103/physrevd.62.124021.

[101] K. S. Thorne, *Gravitational Radiation*. S. W. Hawking and W. Israel, Eds. Mar. 1987, pp. 330–458.

[102] D. W. Hogg, "Distance Measures in Cosmology," Dec. 2000. arXiv: astro-ph/9905116.

[103] S. Weinberg, *Gravitation and Cosmology: Principles and Applications of the General Theory of Relativity*. New York: John Wiley and Sons, Jan. 1972, ISBN: 978-0-471-92567-5.

[104] E. S. Phinney, "A Practical Theorem on Gravitational Wave Backgrounds," Aug. 2001. arXiv: astro-ph/0108028.

[105] A. Sesana, A. Vecchio, and C. N. Colacino, "The Stochastic Gravitational Wave Background from Massive Black Hole Binary Systems: Implications for Observations with Pulsar Timing Arrays," *Monthly Notices of the Royal Astronomical Society*, vol. 390, no. 1, pp. 192–209, Oct. 2008, ISSN: 1365-2966. DOI: 10.1111/j.1365-2966.2008.13682.x.

[106] A. Sesana, "Systematic Investigation of the Expected Gravitational Wave Signal from Supermassive Black Hole Binaries in the Pulsar Timing Band," *Monthly Notices of the Royal Astronomical Society: Letters*, vol. 433, no. 1, pp. L1–L5, May 2013, ISSN: 1745-3925. DOI: 10.1093/mnrasl/slt034.

[107] H. Middleton, W. Del Pozzo, W. M. Farr, A. Sesana, and A. Vecchio, "Astrophysical Constraints on Massive Black Hole Binary Evolution from Pulsar Timing Arrays," *Monthly Notices of the Royal Astronomical Society: Letters*, vol. 455, no. 1, pp. L72–L76, Nov. 2015, ISSN: 1745-3933. DOI: 10.1093/mnrasl/slv150.

[108] A. S. Hamers, "An Improved Numerical Fit to the Peak Harmonic Gravitational Wave Frequency Emitted by an Eccentric Binary," *Research Notes of the AAS*, vol. 5, no. 11, p. 275, Nov. 2021, ISSN: 2515-5172. DOI: 10.3847/2515-5172/ac3d98.

[109] A. Gualandris, F. M. Khan, E. Bortolas, *et al.*, "Eccentricity Evolution of Massive Black Hole Binaries from Formation to Coalescence," *Monthly Notices of the Royal Astronomical Society*, vol. 511, no. 4, pp. 4753–4765, Jan. 2022, ISSN: 1365-2966. DOI: 10.1093/mnras/stac241.

[110] F. Fastidio, A. Gualandris, A. Sesana, E. Bortolas, and W. Dehnen, "Eccentricity Evolution of PTA Sources from Cosmological Initial Conditions," Jun. 2024. arXiv: 2406.02710.

[111] R. Trotta, "Bayesian Methods in Cosmology," Jan. 2017. arXiv: 1701.01467.

[112] D. W. Hogg, J. Bovy, and D. Lang, "Data Analysis Recipes: Fitting a Model to Data," Aug. 2010. arXiv: 1008.4686.

[113] N. Metropolis, A. W. Rosenbluth, M. N. Rosenbluth, A. H. Teller, and E. Teller, "Equation of State Calculations by Fast Computing Machines," *The Journal of Chemical Physics*, vol. 21, no. 6, pp. 1087–1092, Jun. 1953, ISSN: 0021-9606. DOI: 10.1063/1.1699114.

[114] W. K. Hastings, "Monte Carlo Sampling Methods using Markov Chains and their Applications," *Biometrika*, vol. 57, no. 1, pp. 97–109, Apr. 1970. DOI: 10.1093/biomet/57.1.97.

[115] M. Omoya, H. Burton, and H. Baroud, "Bayesian Parameter Estimation of Duration-Based Variables used in Post-Earthquake Building Recovery Modeling," *Earthquake Spectra*, p. 875 529 302 110 737, May 2022. DOI: 10.1177/87552930211073717.

[116] D. Foreman-Mackey, D. W. Hogg, D. Lang, and J. Goodman, "`emcee`: The MCMC Hammer," *Publications of the Astronomical Society of the Pacific*, vol. 125, no. 925, pp. 306–312, Mar. 2013, ISSN: 1538-3873. DOI: 10.1086/670067.

[117] J. Goodman and J. Weare, "Ensemble Samplers with Affine Invariance," *Communications in Applied Mathematics and Computational Science*, vol. 5, no. 1, pp. 65–80, Jan. 2010. DOI: 10.2140/camcos.2010.5.65.

[118] Z. Aziz, D. Abdulqader, A. Sallow, and H. Omer, "Python Parallel Processing and Multiprocessing," *Academic Journal of Nawroz University*, vol. 10, Aug. 2021. DOI: 10.25007/ajnu.v10n3a1145.

[119] D. Foreman-Mackey, "corner.py: Scatterplot Matrices in Python," *The Journal of Open Source Software*, vol. 1, p. 24, Jun. 2016. DOI: 10.21105/joss.00024.

[120] S. Burke-Spolaor, S. R. Taylor, M. Charisi, *et al.*, "The Astrophysics of Nanohertz Gravitational Waves," *The Astronomy and Astrophysics Review*, vol. 27, no. 1, Jun. 2019, ISSN: 1432-0754. DOI: 10.1007/s00159-019-0115-7.

[121] D. Merritt, "The Distribution of Stars and Stellar Remnants at the Galactic Center," *The Astrophysical Journal*, vol. 718, no. 2, pp. 739–761, Jul. 2010, ISSN: 1538-4357. DOI: 10.1088/0004-637x/718/2/739.

[122] R. Schödel, D. Merritt, and A. Eckart, "The Nuclear Star Cluster of the Milky Way: Proper Motions and Mass," *Astronomy & Astrophysics*, vol. 502, no. 1, pp. 91–111, Mar. 2009, ISSN: 1432-0746. DOI: 10.1051/0004-6361/200810922.

[123] A. Weltman, P. Bull, S. Camera, *et al.*, "Fundamental Physics with the Square Kilometre Array," *Publications of the Astronomical Society of Australia*, vol. 37, Jan. 2020, ISSN: 1448-6083. DOI: 10.1017/pasa.2019.42.

[124] S. Burke-Spolaor, "Multi-Messenger Approaches to Binary Supermassive Black Holes in the 'Continuous-Wave' Regime," *Classical and Quantum Gravity*, vol. 30, no. 22, p. 224 013, Nov. 2013, ISSN: 1361-6382. DOI: 10.1088/0264-9381/30/22/224013.

[125] T. Broadhurst, C. Chen, T. Liu, and K.-F. Zheng, "Binary Supermassive Black Holes orbiting Dark Matter Solitons: From the Dual AGN in UGC4211 to Nanohertz Gravitational Waves," May 2024. arXiv: 2306.17821.

[126] M. Aghaie, G. Armando, A. Dondarini, and P. Panci, "Bounds on Ultralight Dark Matter from NANOGrav," *Physical Review D*, vol. 109, no. 10, May 2024, ISSN: 2470-0029. DOI: 10.1103/physrevd.109.103030.

[127] S. A. Klioner, "Gaia-Like Astrometry and Gravitational Waves," *Classical and Quantum Gravity*, vol. 35, no. 4, p. 045 005, Jan. 2018, ISSN: 1361-6382. DOI: 10.1088/1361-6382/aa9f57.

[128] K. Pardo, T.-C. Chang, O. Doré, and Y. Wang, "Gravitational Wave Detection with Relative Astrometry using Roman's Galactic Bulge Time Domain Survey," Jun. 2023. arXiv: 2306.14968.

[129] M. Çalışkan, Y. Chen, L. Dai, N. A. Kumar, I. Stomberg, and X. Xue, "Dissecting the Stochastic Gravitational Wave Background with Astrometry," *Journal of Cosmology and Astroparticle Physics*, vol. 2024, no. 05, p. 030, May 2024, ISSN: 1475-7516. DOI: 10.1088/1475-7516/2024/05/030.

[130] S. D. Odintsov and V. K. Oikonomou, "The Necessity of Multi-Band Observations of the Stochastic Gravitational Wave Background," Jun. 2024. arXiv: 2407.00491.